Multi-Frequency MEMS Sensing Platforms for Advanced Photoacoustic Imaging and Cross-Domain Diagnostic Applications

by

Alberto PRUD HOMME BUELNA

THESIS PRESENTED TO ÉCOLE DE TECHNOLOGIE SUPÉRIEURE
IN PARTIAL FULFILLEMENT FOR THE DEGREE OF
DOCTOR OF PHILOSOPHY
Ph.D.

MONTREAL, MARCH 16, 2026

ÉCOLE DE TECHNOLOGIE SUPÉRIEURE
UNIVERSITÉ DU QUÉBEC

BOARD OF EXAMINERS (THESIS PH.D.)

THIS THESIS HAS BEEN EVALUATED

BY THE FOLLOWING BOARD OF EXAMINERS

Mr. Frederic Nabki, Thesis Supervisor
Department of Electrical Engineering, École de technologie supérieure

Mr. Ricardo J. Zednik, President of the Board of Examiners
Department of Mechanical Engineering, École de technologie supérieure

Mr. Ricardo Izquierdo, Member of the jury
Department of Electrical Engineering, École de technologie supérieure

Mr. Yves Audet, Member of the jury
Department of Electrical Engineering, Polytechnique Montréal

THIS THESIS WAS PRENSENTED AND DEFENDED

IN THE PRESENCE OF A BOARD OF EXAMINERS AND PUBLIC

FEBRUARY 25, 2026

AT ÉCOLE DE TECHNOLOGIE SUPÉRIEURE

PLATEFORMES DE DÉTECTION MEMS MULTIFRÉQUENCES POUR L'IMAGERIE PHOTOACOUSTIQUE AVANCÉE ET LES APPLICATIONS DIAGNOSTIQUES INTER-DOMAINES

Alberto PRUD HOMME BUELNA

RÉSUMÉ

Cette thèse fait progresser l'imagerie photoacoustique (PAI) et les diagnostics multidomaines au moyen d'une plateforme compacte et entièrement à semi-conducteurs, combinant une excitation LED haute puissance via transistor à avalanche, des transducteurs ultrasonores MEMS multifréquences, et des capteurs MEMS passifs de contrainte et de déplacement à très faible consommation.

Sur le plan optique, un pilote à avalanche sur mesure délivre des impulsions de courant de forte intensité, inférieures à 100 ns, vers des LED proche infrarouge. Cette illumination temporellement confinée génère des signaux photoacoustiques robustes dans l'air comme dans l'eau, tout en réduisant les coûts et l'encombrement par rapport aux lasers Q-switched.

Sur le plan acoustique, les transducteurs MEMS sont conçus pour fonctionner à plusieurs fréquences résonantes couvrant une plage d'environ 0,3 à 8 MHz. Cette réponse large bande permet de capter, dans un seul dispositif, des détails superficiels à haute résolution ainsi que des structures plus profondes.

Les capteurs mécaniques compacts facilitent la mesure des déformations et des mouvements à puissance microwatt, permettant la compensation du mouvement et l'optimisation du couplage acoustique. Un capteur à anneaux concentriques atteint une résolution de déplacement de ~2 µm sur une plage de 20 µm, avec une consommation totale de seulement 2,8 µW.

Des prototypes intégrés pourraient permettre une acquisition tenant compte de la mécanique, ouvrant la voie à des systèmes PAI portables, basse consommation, ainsi qu'à des composants réutilisables pour les essais non destructifs, la surveillance environnementale et le diagnostic portable.

Ces résultats établissent les bases d'un système photoacoustique évolutif, abordable et fiable, reposant sur l'excitation LED par avalanche et une détection MEMS multifréquence et mécanique.

Mots-clés: Imagerie photoacoustique, pilote à transistor à avalanche, excitation LED haute puissance, transducteurs ultrasonores MEMS multifréquences, capteurs MEMS passifs de contrainte/déplacement, compensation de mouvement, systèmes d'imagerie.

MULTI-FREQUENCY MEMS SENSING PLATFORMS FOR ADVANCED PHOTOACOUSTIC IMAGING AND CROSS-DOMAIN DIAGNOSTIC APPLICATIONS

Alberto PRUD HOMME BUELNA

ABSTRACT

This thesis advances photoacoustic imaging (PAI) and cross-domain diagnostics through a compact platform that combines high-power LED excitation via avalanche transistor, multi-frequency MEMS ultrasonic transducers, and ultra-low-power passive MEMS strain and displacement sensors.

On the optical side, a custom avalanche driver delivers high-intensity current pulses under 100 ns to near-infrared LEDs. This temporally confined illumination enables robust photoacoustic signal generation in both air and water, while significantly reducing cost and footprint compared to Q-switched lasers.

On the acoustic side, the MEMS transducers are designed to operate across multiple resonant frequencies ranging from approximately 0.3 to 8 MHz. This broadband response allows a single device to capture both high-resolution superficial details and deeper structural features.

Compact mechanical sensors enable deformation and motion measurements at microwatt-level power, facilitating motion compensation and optimization of acoustic coupling. A concentric-ring sensor achieves displacement resolution of ~2 μm over a 20 μm range, with total power consumption of only 2.8 μW.

Future integrated prototypes could enable mechanically aware acquisition, paving the way for portable, low-power PAI systems, as well as reusable components for non-destructive testing, environmental monitoring, and wearable diagnostics.

These results lay the groundwork for a scalable, affordable, and reliable photoacoustic system, based on avalanche-driven LED excitation and multi-frequency mechanical MEMS detection.

Keywords: Photoacoustic imaging, avalanche transistor pulse driver, high-power LED excitation, multi-frequency MEMS ultrasonic transducers, passive MEMS strain/displacement sensors, motion compensation, low-power imaging systems.

TABLE OF CONTENTS

Page

LIST OF TABLES

Page

LIST OF FIGURES

LIST OF ABREVIATIONS

AI	Artificial Intelligence
AO	Acousto-Optic
ATT	Attenuation
BJT	Bipolar Junction Transistor
BW	Bandwidth
CAD	Computer-Aided Design
CMOS	Complementary Metal-Oxide Semiconductor
COMSOL	COMSOL Multiphysics (simulation software)
CUI	Common User Interface
DC	Direct Current
DRIE	Deep Reactive Ion Etching
EMI	Electromagnetic Interference
FEM	Finite Element Method
FMCW	Frequency-Modulated Continuous Wave
GPIO	General-Purpose Input/Output
IUS	IEEE International Ultrasonics Symposium
LDV	Laser Doppler Vibrometer
LED	Light Emitting Diode
MCU	Microcontroller Unit
MEMS	Microelectromechanical Systems
MPE	Maximum Permissible Exposure
NIR	Near Infrared
PAI	Photoacoustic Imaging
PAS	Photoacoustic Spectroscopy
PCB	Printed Circuit Board
PZT	Lead Zirconate Titanate

LIST OF SYMBOLS

V	Volt
A	Ampere
W	Watt
J	Joule
Hz	Hertz
kHz,	kilohertz
µm	micrometer
nm	nanometer
°C	Celsius degrees
Ω,	Ohm
m/s	meters per second
λ	Wavelength
Δ	Delta
Π	Pi
${}_{s}O_2$	Oxygen Saturation
µJ	Microjoules
+/-	Plus/minus

INTRODUCTION

The ever-growing demand for high-resolution biomedical and structural imaging drives innovation in sensing technologies. Photoacoustic imaging (PAI) synergistically combines optical contrast with ultrasound penetration to visualize vascular structures, tumors, and molecular composition at high resolution (Attia et al., 2019). Yet state-of-the-art systems often rely on bulky, expensive nanosecond-pulsed lasers and large, narrowband piezoelectric arrays, limiting portability and cost. Advances in micro-electromechanical systems (MEMS) offer compact, low-power alternatives (Zhu et al., 2018): multi-frequency ultrasonic transducers for broadband reception and passive MEMS strain/displacement sensors that provide co-registered mechanical state. In parallel, high-power LEDs present a cost-effective, durable excitation source. This work is motivated by studying enabling components to an integrated future system: MEMS ultrasound, avalanche-driven LED illumination, and ultra-low-power mechanical sensing. This is mean to be relevant to a future PAI platform that enables affordable, portable imaging and related sensing applications (Beard, 2011; Jin & Liang, 2021).

Motivation

Photoacoustic imaging has emerged as a powerful imaging tool because it provides rich functional and structural information that few other modalities can match. PAI leverages the photoacoustic effect, wherein pulsed light absorbed by tissue causes ultrasonic waves that are then detected to form images. This approach yields high optical contrast and deep penetration, allowing visualization of features from organelles to whole organs with sub-millimeter resolution (L. V. Wang & Hu, 2012). Such capabilities make PAI invaluable for applications ranging from cancer diagnostics to vascular biology. However, conventional PAI hardware typically uses short-pulse lasers (often nanosecond Q-switched lasers) and large piezoelectric transducers optimized for narrow frequency bands. These lasers are costly, complex, and power-hungry, and bulk ultrasound probes cannot easily achieve simultaneous high resolution and deep penetration without multiple arrays or sequential imaging (Xu & Wang, 2006).

At the same time, rapid miniaturization and integration demands in modern sensing and monitoring (e.g. wearable devices, wireless sensor networks, implantables, and in vivo microprobes) call for sensors that are extremely small, low-power, and multifunctional. MEMS technology is ideally suited to these challenges. By virtue of their microfabrication, MEMS sensors can pack multiple sensing functions in a tiny chip. For example, MEMS-based ultrasonic transducers can be engineered with complex geometries (suspended membranes, cantilevers, resonant structures) that support multiple resonant frequencies.

This multi-frequency operation is critical in PAI: high-frequency ultrasound (>20 MHz) provides fine spatial resolution for superficial structures, while low-frequency ultrasound (1–10 MHz) penetrates deeper tissues albeit at lower resolution (H. Wang et al., 2021). A broad operational bandwidth thus enables a single transducer to capture both high-resolution and deep structures simultaneously. The result is a more versatile imaging system without the need for multiple narrowband probes (Van Heumen, Riksen, Singh, Van Soest, & Vasilic, 2023). When paired with co-located mechanical sensors, deformation and coupling changes can be measured and used to stabilize reconstructions across this wide acoustic band.

In parallel, co-registered mechanical sensing addresses a second bottleneck: motion and coupling variability that degrade PAI in handheld, wearable, or in vivo settings. Traditional strain or displacement sensors consume significant power and are bulky when high resolution is required. Passive MEMS strain/displacement sensors convert sub-micron motion into discrete electrical events via engineered contacts, requiring virtually no standby power. A concentric-ring implementation, for example, achieved ~2 μm displacement resolution over a ~20 μm range at ~2.8 μW total power, well below typical piezoresistive approaches. Embedded near the transducer or at the interface, these sensors report local deformation and contact quality, enabling motion compensation, calibration of acoustic coupling, and elastography-style material assessment in real time (Suster, Guo, Chaimanonart, Ko, & Young, 2006).

These advances set the stage for a future integrated, miniaturized PAI platform. By replacing costly lasers with avalanche-driven high-power LEDs and coupling multi-frequency MEMS ultrasound with passive mechanical readouts, the system reduces size, cost, and power while adding a feedback channel that quantifies motion and coupling. The result is improved image stability and repeatability in handheld and wearable use, and a pathway to point-of-care diagnostics, structural monitoring, and other environments where both acoustic and mechanical cues are informative.

The motivation of this work is therefore twofold: first, to overcome the hardware barriers of current PAI by leveraging MEMS and LED-based innovations; and second, to exploit the developed components' versatility in advanced sensing contexts beyond photoacoustic, such as structural (i.e., strain, displacement) sensing (Van Heumen et al., 2023).

Research Problem

Despite its promise, achieving a truly portable and cost-effective photoacoustic imaging system presents several intertwined challenges. The primary research problem tackled in this work is the design and integration of advanced MEMS and electronic subsystems for photoacoustic sensing, to replace bulky lasers and transducers with miniaturized, low-power alternatives (Hariri et al., 2018). Concretely, this involves several sub-problems.

1) Light Source and Pulse Generation

Conventional PAI uses Q-switched lasers to generate nanosecond pulses of light, but these are high-cost and high-power. An alternative is to use high-power LEDs, which are cheaper and more robust. However, LEDs have slower turn-on times and broader spectral output, which typically yield weaker and longer light pulses. Overcoming these limitations requires innovative drive circuitry. One proposed solution is the use of an avalanche transistor-based pulse generator that can produce short, high-voltage pulses to rapidly excite LEDs. The research problem is to develop such a pulse generator and evaluate whether it can drive LEDs to generate photoacoustically relevant pulses (Adachi & Hoshimiya, 2013).

2) Ultrasonic Transducer Design

The quality of PAI critically depends on the ultrasonic transducer. Commercial piezoelectric transducers are optimized for narrow frequency bands, limiting multi-scale imaging. The problem is to create MEMS ultrasonic transducers that support multiple resonant frequencies simultaneously, ensuring high sensitivity across a broad band. This requires novel microstructure design (e.g. floating/anchored membranes, cantilever arrays) and materials (e.g. thin-film piezoelectric layers) to realize broad response without sacrificing miniaturization (Suttikittipong, Parawee, Nicholas, & and Piyawattanametha, 2025).

3) Low-Power Strain/displacement Sensing Elements

Integrate passive MEMS strain/displacement sensors that operate via direct mechanical contact and consume microwatt-level power and tie their outputs explicitly to the PAI pipeline. The goal is micron-scale resolution and digital readout for three tasks: (i) motion compensation and gating, (ii) per-pulse calibration of acoustic coupling and alignment, and (iii) material or tissue stiffness estimation complementary to photoacoustic contrast.

Integrating sensing nodes (such as strain or displacement sensors) into the platform presents another challenge. Any active sensor usually requires continuous bias, which is prohibitive at microscale and low power budgets. The problem addressed here is to devise a passive MEMS strain sensor that operates via direct mechanical contact and consumes virtually no power in standby. The goal is to achieve micron-level resolution and digital output while keeping power consumption in the microwatt range (Mohammed, Moussa, & Lou, 2011). Ultimately, such a sensor could enable motion compensation and gating and allow for coupling calibration and alignment.

4) System Integration and Validation

Even with individual components, integrating them into a functioning system requires careful design. The subsystems (LED pulser, MEMS transducer, MEMS strain/displacement sensor, optics) must be synchronized and their interactions characterized. The problem includes building experimental platforms in which to mount these devices, interfacing analog and digital components, and validating performance (e.g. generating and detecting photoacoustic signals in both air and water mediums) (Yao & Wang, 2021).

5) Adaptability to other Applications

While the primary target is PAI, it is desirable that the developed components be adaptable to other advanced applications. For example, a multi-frequency MEMS transducer might serve in non-destructive testing or in vivo micro-ultrasound probes, and an ultra-low-power strain sensor could be used in structural health monitoring or implantable devices. The research problem thus also includes demonstrating the versatility of these components beyond the initial use-case (Liu, Teng, & Wu, 2015; Mohammed, Moussa, & Lou, 2008; Panas, Cullinan, & Culpepper, 2012).

Accordingly, this work tackles the problem of creating an integrated, MEMS-enabled photoacoustic imaging system by addressing light generation, signal detection, sensing, and system-level integration challenges. Each challenge is complex: driving LEDs to mimic laser pulses, designing broadband MEMS transducers, and inventing ultra-low-power MEMS sensors. Moreover, these must all function together reliably. Solving these will advance the state of the art in portable biomedical imaging and microscale sensing.

Research Objectives

To address the outlined problems, this work sets the following specific research objectives:

1) Develop a High-Power LED Pulse Generator

Design and implement an avalanche-transistor-based pulse generator capable of producing short, high-voltage pulses to drive high-power LEDs. Characterize the electrical and optical pulse characteristics and demonstrate their efficacy in generating photoacoustic signals.

2) Design and Fabricate Multi-Frequency MEMS Transducers

Engineer several micro-scale ultrasonic transducer designs (e.g. circular diaphragms, floating/anchored membranes, cantilever arrays) using the PiezoMUMPs process. Each design should support multiple resonant modes across a broad frequency range. Perform finite-element simulations and experimental characterization (e.g. laser Doppler vibrometry) to verify that these devices cover frequencies spanning at least 0.3–8 MHz.

3) Implement Passive MEMS Strain Sensors

Develop a MEMS passive strain/displacement sensor using a direct-contact transduction mechanism. Fabricate sensor variants (e.g. cantilever, stacked beam, concentric ring) and integrate them with a low-power microcontroller for digital readout. Aim for sub-5 µm displacement resolution over a range of ~20 µm, while limiting total power consumption to a few microwatts. Note that due to time constraints, we could not co-locate these sensors with the ultrasonic chip and incorporate their measurements into PIA workflows. Nonetheless, these are realised and fully characterized.

4) Integrate Subsystems and Validate Operation

Develop preliminary experimental setups of key subsystems, namely, the LED pulser, MEMS ultrasonic transducer, and MEMS strain/displacement sensor, along with essential signal conditioning, communication, and optical components where applicable. Use these setups to explore initial system interactions, focusing on generating photoacoustic signals with the LED source and conducting preliminary detection trials using the MEMS ultrasonic transducer. Employ the MEMS sensor to assess basic strain or displacement behaviors relevant to system calibration or feedback. While full integration and performance characterization across media (e.g., air, water) remain future goals, this stage emphasizes proof-of-concept validation and identifies key technical challenges for complete system-level integration in subsequent work.

These objectives collectively aim to replace bulky, high-power PAI hardware with a suite of innovative MEMS and electronic subsystems. The successful completion of these tasks should result in a demonstrable low-cost, miniaturized photoacoustic imaging prototype, as well as transferable technologies for other sensing domains.

Contributions

This work makes the following key contributions:

1) Low-Cost LED-Based Photoacoustic Radiance

Demonstrate a photoacoustic imaging setup using high-power LEDs driven by a novel avalanche oscillator pulse generator. The custom circuit generates nanosecond-scale high-voltage pulses that excite the LEDs, producing intense light flashes. Experiments showed that these LED pulses generate clear photoacoustic signals in both air and water, proving feasibility. Compared to lasers, this approach drastically reduces size, cost, and maintenance requirements while still achieving sufficient pulse intensity for tissue excitation (Allen & Beard, 2016). This contribution paves the way for affordable, portable PAI systems and expands the use of LEDs in biomedical imaging (Van Heumen et al., 2023).

2) Multi-Resonant MEMS Ultrasonic Transducers

Design and characterize a family of MEMS ultrasonic transducers that each support multiple resonant modes. Using the PiezoMUMPs process, four geometries were realized: circular diaphragms, floating crosses, anchored crosses, and cantilever arrays. Experimental measurements revealed that the circular diaphragm had a narrowband response (~1.7 MHz, Q≈268), whereas the complex structures exhibited broad spectral coverage from ~0.3 to >7.5 MHz. In particular, the cantilever array showed the densest modal distribution due to varying arm lengths, enabling asynchronous resonance. These multi-frequency devices overcome the bandwidth constraints of traditional piezoelectric transducers. By combining diverse mechanical designs on a single chip, the work demonstrates a pathway to compact transducers that capture both high-resolution superficial and deep-tissue signals simultaneously (Jaber, Ramini, Hennawi, & Younis, 2016; Uttamchandani, 1995). The form factor can be suited for co-location with the mechanical sensors.

3) Ultra-Low-Power MEMS Strain Sensor

A new MEMS passive strain/displacement sensor with a direct-contact detection mechanism was developed and validated. Three designs (cantilever, stacked beam, concentric ring) were evaluated, and a concentric ring configuration achieved the best trade-off: 2 µm resolution over a 20 µm range with contact resistances <20 kΩ. Crucially, the sensor requires no bias current until activation; the entire system (including signal conditioning and UART interface) consumes only 2.8 µW during operation. This is roughly 10% of the power used by the microstructure itself. The passive contact-based architecture is highly novel, diverging from conventional active piezoresistive sensors, and it enables high-precision monitoring in energy-constrained settings (e.g. wireless nodes, implantables). When integrated with the ultrasonic chip, these sensors could provide motion compensation and coupling calibration.

4) Integrated Experimental Platforms

The components above were integrated into test platforms that validate their interaction. For example, the LED pulser and MEMS transducer were paired to perform end-to-end photoacoustic signal generation and detection. The strain sensor was embedded with a low-power microcontroller to demonstrate digital readout under mechanical displacement. These systems confirmed that the submodules operate as intended and interact seamlessly. Notably, the LED-based PAI system produced detectable signals across different media, and the MEMS transducer responded over its designed multi-frequency band, confirming model predictions.

5) Framework for Broad Applications

Beyond the immediate focus on photoacoustic imaging, a significant contribution of this work is the demonstration of the versatility of the developed MEMS devices for other sensing applications. Several alternative use cases were evaluated to illustrate the potential of reusing the same MEMS components in varied domains:

The multi-frequency MEMS ultrasonic transducers, originally developed to detect broadband photoacoustic signals, were evaluated as air-coupled ultrasonic receivers in non-contact structural health monitoring systems. Their wide spectral response and small form factor enable deployment in distributed arrays for detecting acoustic emissions, identifying cracks in materials, or characterizing surfaces. In air or low-pressure environments, these devices demonstrated reliable sensitivity at both low and high frequencies, making them suitable for airborne acoustics and smart infrastructure sensing networks.

The MEMS strain sensors, while integrated into the PAI platform for detecting mechanical deformation and structural feedback, were also tested in quasi-static mechanical setups simulating wearable biomechanical monitoring and in-situ pressure sensing in flexible substrates. Their passive, direct-contact mechanism with ultra-low power consumption makes them ideal candidates for implantable biomedical sensors and IoT-enabled condition monitoring where energy harvesting or battery-free operation is essential. Their high resolution and robustness to environmental variations support operation in dynamic and harsh conditions.

Additionally, the avalanche-driven LED pulser, designed for light-based excitation in PAI, was demonstrated as a programmable optical pulse generator suitable for portable spectroscopic systems, low-cost LiDAR, and optical communication prototypes. Its ability to deliver nanosecond-scale, high-intensity light bursts at adjustable repetition rates opens applications in low-budget optical diagnostics and short-range communication in biomedical or industrial settings.

This multi-purpose evaluation highlights the design philosophy of cross-domain compatibility: components were intentionally developed with generalized architectures and scalable interfaces, enabling reuse across sensing modalities. The modularity of the developed subsystems (optical, mechanical, electrical) ensures that the technology can be adopted for a wide variety of sensing platforms—including miniaturized ultrasound probes, environmental monitoring drones, and smart medical implants—thereby amplifying the scientific and commercial impact of the research.

The combined contributions of the proposed circuit architectures, MEMS device designs, and system-level demonstrations provide a strong and coherent validation of the research objectives. The LED-driven photoacoustic imaging (PAI) system is presented in the article “Cost-Effective Photoacoustic Imaging Using High-Power LEDs Driven by an Avalanche Oscillator,” published in MDPI Sensors in March 2025, where a low-cost and energy-efficient excitation approach is experimentally demonstrated.

The development of multi-frequency MEMS transducers for enhanced photoacoustic performance is detailed in “Design and Characterization of Multi-Frequency MEMS Transducers for Photoacoustic Imaging,” submitted to MDPI Sensors in December 2025. In parallel, the concept of passive mechanical sensing is addressed in “Highly Integrated MEMS Passive Strain Sensor with a Direct Contact Detection Mechanism,” published in the Journal of Microelectromechanical Systems in November 2025. Collectively, these contributions establish a unified and technically rigorous advancement in low-power, MEMS-enabled sensing and photoacoustic system design.

Positioning of the Contributions Toward a Compact Photoacoustic Platform

This thesis presents a set of experimentally validated building blocks toward a compact and fully solid-state photoacoustic imaging platform. Rather than developing a complete imaging system at once, this work addresses the key subsystems required for such a platform: optical excitation, acoustic detection, and mechanical sensing. Each of the included papers contributes a validated subsystem that enables a future integrated implementation.

The LED-based photoacoustic excitation system presented in Chapter 2 establishes a compact and low-cost optical source capable of generating photoacoustic signals without the need for bulky pulsed lasers. This subsystem defines the optical excitation building block of the proposed platform. The passive MEMS strain and displacement sensors described in Chapter 3 provide mechanical awareness of the sensor–tissue interface, enabling motion compensation and coupling monitoring. These devices constitute the mechanical sensing building block required for stable portable operation. The multi-frequency MEMS ultrasonic transducers presented in Chapter 4 form the acoustic detection building block, enabling broadband reception within a compact MEMS-compatible architecture.

The individual subsystems were experimentally validated and demonstrated to operate within photoacoustically relevant conditions. Photoacoustic signal generation using LED excitation was demonstrated in both air and water environments. MEMS strain sensors were fabricated and experimentally characterized with micrometer-scale resolution. Multi-frequency MEMS ultrasonic transducers were designed and experimentally validated using laser Doppler vibrometry.

However, full system-level integration remains future work. In particular, a complete photoacoustic imaging system based on the proposed MEMS transducers has not yet been demonstrated. A complete imaging system combining LED excitation, MEMS ultrasonic detection, and mechanical sensing in a single immersed photoacoustic imaging platform has not yet been realized. Image reconstruction experiments using MEMS transducers, systematic immersed validation, and full integration of optical excitation, acoustic detection, and mechanical sensing represent the main steps required toward a fully integrated compact PAI platform.

Publications Arising from this Thesis

Parts of the research presented in this thesis have been disseminated through three papers that align with the three main subsystems developed in this work: LED-based optical excitation for photoacoustic signal generation, multi-frequency MEMS ultrasonic transducers for broadband acoustic detection, and passive MEMS strain/displacement sensing for ultra-low-power mechanical feedback. The papers stemming from this work are listed below:

- Prud'homme and F. Nabki, "Cost-Effective Photoacoustic Imaging Using High-Power Light-Emitting Diodes Driven by an Avalanche Oscillator," MDPI Sensors, vol. 25, no. 6, Art. no. 1643, 2025, doi: 10.3390/s25061643.
- Prud'homme and F. Nabki, "Design, Fabrication and Characterization of Multi-Frequency MEMS Transducer for Photoacoustic Imaging," MDPI Micromachines, vol. 17, no. 1, Art. no. 122, Jan. 2026, doi: 10.3390/mi17010122.
- Prud'homme, P. Okulov, and F. Nabki, "Highly Integrated MEMS Passive Strain Sensor with a Direct Contact Detection Mechanism," IEEE J. Microelectromech. Syst., manuscript resubmitted March 5th, 2026, under review following a major revision decision.

Thesis Outline

The structure of this thesis is as follows:

Chapter 1 provides a comprehensive overview of the scientific and technological foundations of the research presented in this work. The focus is on the underlying physical principles of PAI, the evolution of excitation light sources, the transition from conventional ultrasonic transducers to MEMS-based solutions, and the integration of optoacoustic systems with low-power MEMS sensors. The literature review concludes with an outline of the major challenges in current systems and the emerging opportunities created by MEMS-based miniaturized platforms for biomedical and multi-domain sensing.

Chapter 2 details the design of the avalanche-oscillator pulse generator, characterization of the LED light pulses, and experiments demonstrating photoacoustic signal generation and detection. The feasibility of an all-LED PAI system is evaluated, with discussions on performance in different media.

Chapter 3 covers sensor microfabrication, integration with electronics, and characterization. Resolution, hysteresis, and power consumption results are presented, highlighting the sensor's performance in autonomous monitoring roles.

Chapter 4 describes the design, fabrication, and testing of MEMS ultrasonic transducers with diverse geometries. Finite-element and laser vibrometry results are given, showing how each structure contributes to broadband frequency coverage. The potential imaging advantages of these devices are discussed.

Chapter 5 summarizes the thesis contributions and discusses their implications. It also outlines potential future developments, such as improving signal-to-noise ratios, miniaturizing packaging, and exploring new applications in biomedical diagnostics or environmental sensing.

CHAPTER 1

LITERATURE REVIEW

This literature review establishes the theoretical and technological framework underlying the development of a fully solid-state, multi-modal photoacoustic imaging platform. The discussion begins with a targeted review of the physics of photoacoustic generation, limited to the governing relationships most relevant to system-level design—specifically those that influence optical pulse shaping, thermal and stress confinement, and acoustic signal bandwidth. From this foundation, the review systematically examines three critical domains of the PAI pipeline: optical excitation and drive electronics, ultrasonic transduction mechanisms, and integrated mechanical sensing.

Optical excitation strategies are analyzed with a focus on the transition from laser-based systems to high-power light-emitting diodes, including the pulse generation techniques necessary to meet confinement criteria at reduced cost and complexity. The section on ultrasonic detection details the evolution from bulk piezoelectric elements to miniaturized MEMS transducers with engineered geometries for multi-frequency operation and broad spectral capture.

Finally, the review explores co-registered mechanical sensing approaches that enable real-time inference of strain and displacement via ultra-low-power MEMS sensors. Beyond their minimal power footprint and integration potential, these sensors offer a novel pathway to embed contextual awareness within the imaging system itself. By directly monitoring mechanical deformation and acoustic coupling at the point of contact, such sensors provide actionable feedback that can enhance image stability, support motion compensation, and enable elastography-style contrast without additional instrumentation.

1.1 Introduction to Photoacoustic Imaging

Photoacoustic imaging is a hybrid modality that exploits the physics of light–matter interactions and acoustic wave propagation to reconstruct images of internal tissue structures with both optical contrast and acoustic resolution. The process relies on the photoacoustic effect, which occurs when a short optical pulse is absorbed by a material, causing localized heating, rapid thermal expansion, and the emission of broadband acoustic waves. These waves can be detected using ultrasonic transducers and processed into images that reflect both anatomical and functional tissue properties (Xu & Wang, 2006).

The generation of photoacoustic signals involves a chain of coupled physical processes, typically divided into four conceptual stages: optical absorption and energy deposition, thermal and stress confinement, initial pressure generation, and acoustic propagation and detection. Each stage introduces parameters and constraints that are fundamental to the design of efficient, high-resolution, and low-power imaging systems. This section presents a concise but detailed review of the physical principles that underlie these stages, forming the theoretical foundation for the hardware architectures and MEMS-based designs explored in this thesis (Beard, 2011).

1.1.1 Optical Absorption and Energy Deposition

The photoacoustic process is initiated by the delivery of a short high-intensity pulse of light typically in the visible or near-infrared spectrum to a target medium. Within biological tissues specific molecules known as chromophores absorb this light selectively based on wavelength. In biological tissues, chromophores are optically absorbing constituents whose wavelength-dependent absorption determines the spatial distribution of deposited optical energy. Common endogenous chromophores include oxyhemoglobin, deoxyhemoglobin, melanin, lipids, and water, each exhibiting distinct absorption spectra (Hariri et al., 2018).

The spatial distribution of fluence depends on both the optical properties of the medium (absorption and scattering coefficients) and the geometry of the illumination system. In typical soft tissues optical absorption leads to a rapid but spatially confined rise in temperature. Although the temperature increase is usually small on the order of millikelvins if it occurs over a sufficiently short time and small volume it leads to rapid pressure generation through thermal expansion (Hariri et al., 2018).

Common endogenous chromophores include oxyhemoglobin, deoxyhemoglobin, melanin, lipids and water, each with unique absorption spectra. The efficiency of energy deposition at a location r and wavelength λ is governed by the absorption coefficient $\mu a\ (r,\lambda)$ and the local optical fluence $\phi(r,\lambda)$ expressed as:

$$A(r,\lambda) = \mu_a(r,\lambda) \cdot \phi(r,\lambda) \tag{1.1}$$

where:
$\mu_a\ is\ the\ local\ absorption\ coefficient\ \ [cm^{-1}]$
ϕ is the optical fluence $\left[{}^{J}/_{cm^2}\right]$
A is the absorbed optical energy density $\left[{}^{\mathrm{J}}/_{cm^3}\right]$
$r\ is\ the\ position\ vector$

In practical systems the efficiency of this stage is strongly influenced by the optical wavelength, beam geometry, pulse energy and the depth-dependent fluence profile. For superficial applications such as skin imaging blue or green light may be appropriate. For deeper tissue targets near-infrared light (650–950 nm) is preferred due to reduced scattering and absorption resulting in an optical window that permits greater penetration depths (Manwar, Islam, Ranjbaran, & Avanaki, 2022).

1.1.2 Thermal and Stress Confinement

The second critical stage involves the temporal constraints required for efficient conversion of thermal energy into acoustic pressure. For the photoacoustic effect to occur with high fidelity the heating process must be both thermally confined and mechanically confined within the target region. These conditions ensure that energy remains localized during the time it is being deposited and that mechanical expansion occurs impulsively rather than gradually.

Thermal confinement refers to the requirement that heat diffusion is negligible during the laser or LED pulse duration τ_p . This is quantified by comparing the pulse duration to the thermal diffusion time τ_{th}, given by

$$\tau_{\mathrm{th}} = \frac{d^2}{4\alpha} \tag{1.2}$$

where *d* is the characteristic dimension of the absorber and α\alphaα is the thermal diffusivity of the medium (typically $\sim 1.4 \times 10^{-7}$ m^2/s for soft tissue). If $\tau_p < \tau t_{hp}$ then thermal energy does not dissipate significantly during the pulse and the absorber can be considered thermally confined (Manwar et al., 2022).

Stress confinement requires that mechanical relaxation does not occur during the energy deposition period. That is, the tissue must not have time to expand while the heating process is still ongoing (Manwar et al., 2022).. The stress confinement condition is defined by:

$$\tau_s = \frac{d}{c_s} \tag{1.3}$$

where c_s is the speed of sound in the medium (approximately 1540 m/s in soft tissue). The pulse duration must satisfy $\tau_p < \tau_s$ to ensure stress confinement.

Taken together these two conditions impose upper limits on τ_p that vary with the size of the target absorber. For example a 100 µm capillary has a thermal confinement time of ~18 µs and a stress confinement time of ~65 ns. In practice to image microvascular structures or subcellular targets excitation pulses must be shorter than 100 ns.

1.1.3 Initial Pressure Generation

Once the energy is absorbed and confinement conditions are satisfied the localized temperature rise induces a transient pressure rise due to thermoelastic expansion. This process is described by the generation of initial pressure p_0 which serves as the source term for the acoustic wave equation (Jin & Liang, 2021). The magnitude of this pressure is proportional to the local energy absorption and is governed by the Grüneisen parameter Γ:

$$p_o(\mathrm{r}) = \Gamma A(r, \lambda) \tag{1.4}$$

The initial pressure distribution encodes both structural and functional information. Its amplitude reflects local optical absorption (e.g., blood volume) while its temporal shape contains depth-dependent details due to time-of-flight differences during acoustic propagation (Beard, 2011).

1.1.4 Acoustic Propagation and Detection

The final stage in photoacoustic signal generation is the propagation of the pressure wave from its point of origin to the surface where it is detected by an ultrasonic sensor. Once generated the pressure wave obeys the standard wave equation and travels outward in all directions undergoing some degree of acoustic attenuation scattering and mode conversion depending on the tissue architecture (Beard, 2011).

Because the excitation event is impulsive and spatially confined the resulting acoustic signal is broadband. The characteristic frequency content is determined by the size and geometry of the absorber. A simplified approximation relates the central frequency f_c of the emitted spectrum to the characteristic absorber size d:

$$f_c = \frac{c_s}{d} \tag{1.5}$$

Smaller absorbers generate higher-frequency signals while larger structures generate lower-frequency content. For example capillary-level absorbers (~10 µm) can produce signals above 15–20 MHz whereas large vessels (~1 mm) generate dominant components below 2 MHz. Biological tissues typically contain structures across a range of spatial scales resulting in photoacoustic signals that span from hundreds of kilohertz to tens of megahertz (Jin & Liang, 2021).

To preserve spatial and spectral information detection systems must exhibit wide bandwidth high sensitivity and low noise. Conventional piezoelectric transducers are often narrowband and optimized for fixed clinical frequencies limiting their ability to capture the full photoacoustic spectrum. This motivates the development of multi-resonant MEMS ultrasonic receivers as described in later chapters of this thesis to ensure sensitivity across a broader frequency range and support simultaneous imaging of superficial and deeper targets.

The physics of photoacoustic generation establishes clear performance targets for the design of imaging systems. Efficient optical absorption requires wavelength selection matched to tissue chromophores. Thermal and stress confinement dictate the need for sub-100 ns excitation pulses which influences driver circuit architecture. Initial pressure amplitude depends on the Grüneisen parameter which varies by tissue type and informs imaging contrast expectations. Finally the broadband nature of acoustic propagation necessitates detectors capable of multi-frequency operation.

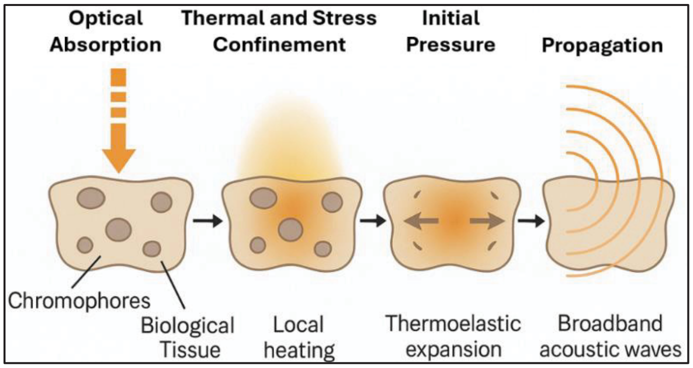

Figure 1.1 Photoacoustic Effect Process

These physical insights directly guide the engineering strategies developed in this thesis particularly the use of avalanche-transistor LED drivers broadband MEMS ultrasonic transducers and integrated passive sensors for motion and coupling awareness. Together these elements form a compact low-power platform that fully leverages the underlying physics to enable robust photoacoustic imaging in both biomedical and cross-domain diagnostic applications.

1.2 Optical Excitation Sources and High-Speed Drivers for PAI

The optical excitation source plays a central role in defining the performance, capabilities, and application space of a PAI system. Its characteristics govern not only the achievable spatial resolution and imaging depth but also determine critical factors such as device cost, system complexity, power consumption, and potential for miniaturization. From the standpoint of system engineering, the selection of an appropriate light source entails a multidimensional trade-off involving photophysical performance, integration feasibility, and clinical relevance.

Traditionally, PAI systems have predominantly relied on high-energy pulsed lasers capable of delivering nanosecond-scale light bursts with sufficient peak power to fulfill both stress and thermal confinement conditions. These systems are indispensable in research and high-performance clinical imaging due to their high signal-to-noise ratio (SNR), deep tissue penetration, and spectral tunability. However, their size, cost, and operational complexity impose severe limitations on their deployment in point-of-care, wearable, or resource-constrained environments (Allen & Beard, 2016; Van Heumen et al., 2023).

In recent years, the increasing demand for scalable, accessible, and portable photoacoustic systems has catalyzed research into alternative excitation technologies. High-power Light-Emitting Diodes, in particular, have garnered substantial attention owing to their favorable attributes: compactness, low cost, compatibility with low-voltage electronics, and high repetition rates. Despite their advantages, LEDs present non-trivial challenges, notably their limited peak power output and broader spectral bandwidth, which have historically limited their adoption in high-resolution PAI (Jin & Liang, 2021).

It contrasts conventional laser-based excitation systems with emerging LED-based approaches, elucidating their respective physical principles, performance limitations, and engineering implications. Special attention is devoted to the electrical driving circuitry required to enable nanosecond-scale pulse shaping in LED-based systems—particularly avalanche transistor-based oscillators—which represent a promising route for achieving compact, cost-effective, and clinically viable PAI platforms (Zhu et al., 2018).

1.2.1 Laser-Based PAI Systems

Since its inception, photoacoustic imaging has been intimately associated with the use of Q-switched pulsed lasers. These lasers are uniquely capable of delivering the high-peak-power, short-duration optical pulses required to induce efficient thermoelastic expansion within biological tissues. Pulse durations on the order of 5–10 nanoseconds are critical to ensure that both thermal and stress confinement conditions are satisfied, thereby optimizing the amplitude and bandwidth of the resulting photoacoustic signals (Allen & Beard, 2016; Yao & Wang, 2021).

Several classes of pulsed lasers have been extensively utilized in PAI research and clinical prototypes:

- Nd:YAG Lasers (1064 nm, 532 nm): Widely adopted due to their robust output energy, long operational life, and commercial maturity. Frequency-doubled variants enable dual-wavelength operation.
- Optical Parametric Oscillators (OPOs): When coupled with Nd:YAG or Ti:Sapphire lasers, OPOs afford wavelength tunability from the visible through the near-infrared (NIR) range (400–2500 nm), facilitating multispectral and molecular imaging.
- Dye Lasers: Provide exceptional spectral flexibility but entail cumbersome dye handling protocols and limited photostability.
- Ti:Sapphire Lasers: Employed in high-resolution, ultrafast, and multimodal imaging systems; compatible with two-photon excitation for advanced imaging workflows.
- Spectral Control and Tissue Penetration

A major advantage of laser-based excitation is the availability of narrowband, wavelength-tunable light sources that allow selective absorption targeting of intrinsic chromophores (e.g., oxy- and deoxy-hemoglobin, melanin, lipid, collagen) and exogenous contrast agents.

This spectral precision supports:

- Multispectral Unmixing: Enabling quantification of functional biomarkers, such as blood oxygen saturation or lipid content in plaques.
- Molecular Specificity: Facilitating targeted imaging using fluorescent or optoacoustic probes with distinct absorption spectra.
- Depth Optimization: Utilizing the optical window between 650–950 nm, where tissue absorption is minimized and scattering is reduced, to achieve deeper penetration.
- Nonetheless, optical fluence must conform to established safety thresholds, such as the ANSI standard limiting skin exposure to ~20 mJ/cm² in the NIR band, particularly in clinical or in vivo applications.

1.2.1.1 Practical Limitations

Despite their performance, laser systems present several drawbacks that inhibit their deployment in compact or wearable devices:

- Form Factor: Laser heads, cooling assemblies, and beam-shaping optics occupy significant physical volume.
- Energy Requirements: High-voltage and cooling demands result in substantial power consumption.
- Economic Cost: High cost for research-grade pulsed lasers with tunability, posing a barrier to widespread adoption.
- Maintenance Overhead: Optical alignment, periodic calibration, and consumables (e.g., dyes) contribute to operational complexity.

These limitations have accelerated the search for alternative optical sources that retain sufficient photoacoustic efficacy while offering improvements in size, cost, and system-level integration (Allen & Beard, 2016).

1.2.2 LED-Based Excitation PAI

High-power LEDs have emerged as promising alternatives to lasers in photoacoustic imaging. Unlike lasers, LEDs are inexpensive, compact, and mechanically robust. Their small footprint allows integration into portable and handheld devices, significantly reducing the complexity of optical alignment and system assembly. Another key advantage is their ability to operate at very high repetition rates, which enables frame averaging and supports real-time imaging applications. Moreover, LEDs are available across a wide spectral range, offering flexibility in selecting wavelengths relevant to various biomedical targets (Adachi & Hoshimiya, 2013; Allen & Beard, 2016).

Their inherent advantages over laser-based sources include:

- Miniaturization: Typical LED packages measure only a few millimeters.
- Safety: LEDs exhibit negligible risk of ocular or dermal injury under standard operating conditions.
- Affordability: Unit costs are substantially lower than for pulsed lasers.
- Power Supply Compatibility: Operate at low voltages, facilitating battery operation.
- High Repetition Rates: Capable of continuous or pulsed operation at kHz–MHz frequencies, supporting real-time imaging.

These characteristics align closely with the goals of modern medical device design, particularly in contexts such as home monitoring, ambulatory care, and telehealth-enabled diagnostics (Hariri et al., 2018).

1.2.2.1 Performance Challenges

Despite their benefits, LEDs face intrinsic limitations in the context of PAI:

- Peak Optical Power: Conventional high-power LEDs produce only microjoule-scale pulses—several orders of magnitude lower than Q-switched lasers.
- Spectral Broadening: LEDs typically exhibit FWHM of 20–50 nm, potentially reducing the specificity of chromophore targeting.
- Longer Pulse Durations: The electrical and thermal characteristics of standard drivers often lead to optical pulses >100 ns, impairing spatial resolution and violating confinement conditions.

To mitigate these drawbacks, this work employs avalanche-transistor-based drivers to deliver ultra-fast, high-current pulses to the LED, thereby reducing optical pulse duration and enhancing the amplitude of the induced photoacoustic signal (Hariri et al., 2018).

Nevertheless, LEDs face important performance limitations when compared with lasers. First, their pulse widths are typically longer, often on the order of tens to hundreds of nanoseconds, which can compromise compliance with thermal and stress confinement conditions. Second, their peak optical fluence is substantially lower than that of pulsed lasers, resulting in weaker photoacoustic signals, especially in deeper tissues. Finally, LEDs have relatively broad spectral emission compared to the narrow linewidth of lasers. While this spectral width provides versatility, it reduces the ability to perform highly selective molecular imaging. Taken together, these trade-offs highlight the need for advanced driver circuits that maximize the utility of LEDs by producing short, high-intensity pulses while mitigating their inherent limitations (Zhu et al., 2018).

1.2.3 High-Speed LED Pulse Generation and Drivers

The performance of LED-based photoacoustic imaging systems is determined not only by the LEDs themselves but also by the electronic circuits that drive them. In order to produce efficient photoacoustic signals, LEDs must be pulsed with high peak currents and sub-100 ns widths, a regime that requires specialized high-speed drivers rather than conventional LED power supplies. Several classes of pulse generators have been explored in photoacoustic imaging, each with its own advantages and limitations (Adachi & Hoshimiya, 2013; Allen & Beard, 2016).

Capacitor-discharge circuits represent one of the earliest methods used for generating short LED pulses. In these circuits, a capacitor is charged to a predetermined voltage and then rapidly discharged through the LED. Their main advantage is simplicity and relatively high current delivery, making them easy to implement. However, their switching speed is limited, leading to relatively long rise times and pulse widths. The efficiency of energy transfer is also low, and repeated high-frequency pulsing is difficult due to capacitor recharge times.

MOSFET- and GaN-transistor based drivers have also been employed, benefiting from the fast switching capabilities of modern transistors. These circuits can achieve shorter rise times and higher repetition rates compared to capacitor-discharge circuits. They are also relatively efficient and scalable. The main drawbacks are complexity in circuit design, sensitivity to parasitics, and the need for precise gate-driving signals. Furthermore, as the required pulse widths shrink toward tens of nanoseconds, the parasitic capacitances and inductances of the circuit become a critical bottleneck, limiting performance.

Avalanche-transistor pulsers, also known as avalanche oscillators, have emerged as the most promising solution for driving LEDs in photoacoustic imaging. These devices exploit the avalanche breakdown phenomenon of bipolar transistors to produce extremely fast and high-current switching events. When biased near breakdown, the transistor can be triggered to switch almost instantaneously, releasing the stored energy in a nanosecond-scale pulse with a very steep rise time. This enables LED excitation pulses with widths well below 100 ns and peak currents far exceeding those of conventional transistor-based drivers (Hariri et al., 2018).

The advantages of avalanche pulsers are significant in the context of portable and low-cost PAI. First, they allow LEDs to approximate the temporal characteristics of laser pulses, thereby satisfying stress confinement conditions required for efficient photoacoustic generation. Second, the circuits are compact and can be implemented with inexpensive off-the-shelf components, reducing both system size and cost. Third, avalanche pulsers can operate at relatively high repetition rates, which is essential for real-time imaging and averaging-based signal enhancement (Zhu et al., 2018).

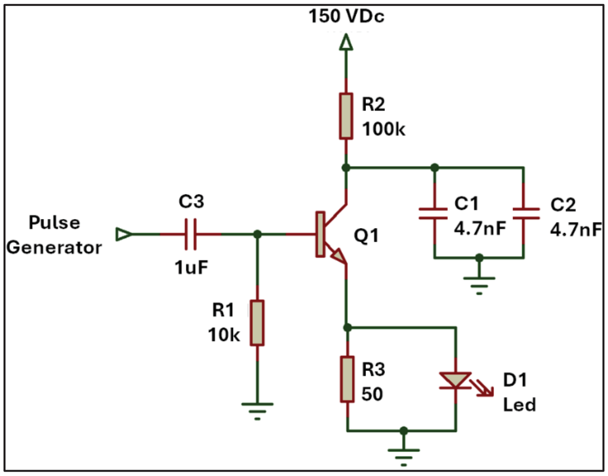

Figure 1.2 Diagram of the avalanche oscillator with LED

Despite these advantages, avalanche drivers present integration challenges. Their very fast switching events generate significant electromagnetic interference, which can couple into sensitive acquisition electronics. The extremely high currents can also stress the LEDs, raising thermal management and reliability concerns. Careful design of circuit layout, shielding, and heat dissipation is therefore essential to harness the benefits of avalanche pulsers while mitigating their drawbacks (Jinyuan, Bing, & Zenghu, 1998).

1.2.3.1 Representative Pulse Generator Approaches

While the underlying physics requires short, high-intensity pulses, the practical implementation of such drivers varies widely depending on the source, the intended application, and the trade-offs between cost, complexity, and efficiency. To provide perspective on the operational landscape, Table 1.1 summarizes representative studies that report different pulse generator implementations for photoacoustic imaging.

Table 1.1 Pulse Generators Reports for PAI

Reference	Pulse duration	Sample Rate
(Joseph Francis et al., 2020)	70 ns	4 KHz
(Bulsink et al., 2021)	70 ns	4.2 KHz
(Zhu et al., 2018)	100 ns	4 KHz
(Janggun et al., 2020)	35 ns	1.5 KHz
(Van Heumen et al., 2023)	70 ns	4 KHz
(Zeng, Liu, Di-Wu, & Ji, 2014)	100 ns	800 Hz
(Allen & Beard, 2016)	200 ns	500 Hz

The reported pulse durations span from as short as 35 ns to as long as 200 ns. At the lower end, pulses in the range of 35–70 ns are well suited to satisfy stress confinement conditions for small-scale absorbers, thereby enabling high-resolution imaging with broader acoustic bandwidths. In contrast, longer pulses around 200 ns relax these confinement requirements and produce narrower bandwidth signals, which are more appropriate for imaging larger or deeper structures where resolution can be traded for penetration and signal strength. This spread illustrates how different pulse durations can be tailored to balance resolution and depth in PAI applications.

Sample rate shows a similarly wide variation, from only 500–800 Hz in some early systems to as high as 40 kHz in more recent reports. Low repetition rates limit imaging speed and make real-time operation impractical, whereas higher rates allow frame averaging and dynamic imaging. For instance, studies operating at ~4 kHz demonstrate a compromise between per-pulse energy and acquisition speed, while work at tens of kilohertz highlights the feasibility of real-time imaging even when individual pulses are relatively weak. This range confirms that high repetition rates are increasingly emphasized in recent designs as a pathway to portable and clinically viable photoacoustic devices.

Beyond pulse duration and optical energy considerations, the temporal characteristics of the excitation source directly determine practical imaging performance in photoacoustic systems. The pulse duration governs compliance with thermal and stress confinement conditions and therefore influences the achievable acoustic bandwidth and spatial resolution. The repetition rate, in contrast, directly determines the achievable imaging speed. In scanning-based configurations, the total acquisition time increases with the number of measurement positions and decreases with increasing pulse repetition rate. Systems operating at low repetition rates may require several seconds to acquire a single image, restricting operation to static targets, whereas higher repetition rates enable faster acquisition and support dynamic imaging or frame averaging for improved signal-to-noise ratio. For example, repetition rates on the order of 100 Hz can be sufficient for proof-of-concept or laboratory imaging of static targets, particularly when signal averaging is used to improve signal-to-noise ratio, although such rates generally remain insufficient for real-time imaging. Consequently, pulse width and repetition rate must be selected not only to ensure efficient photoacoustic generation but also to achieve acquisition times compatible with practical imaging requirements.

1.3 Ultrasonic Detection for Photoacoustic Imaging

In photoacoustic imaging (PAI), ultrasonic detection constitutes the essential bridge between optical excitation and signal acquisition. While nanosecond optical pulses generate thermoelastic expansion and subsequent pressure transients within tissue, the ultimate quality of the reconstructed image depends critically on the acoustic transducer. Parameters such as sensitivity, bandwidth, frequency response, spatial aperture, and integration feasibility determine whether the system can achieve high-resolution anatomical mapping, functional assessment, or quantitative diagnostics (H. Wang et al., 2021).

Over the past decades, the field of ultrasonic transduction has progressed from centimeter-scale bulk piezoelectric elements to advanced microfabricated MEMS devices capable of enabling compact, broadband, and application-specific PAI platforms (Ren, Li, Shi, & Chen, 2022).

1.3.1 Conventional Piezoelectric Transducers

Conventional ultrasonic detection in biomedical imaging has been dominated for decades by bulk piezoelectric crystals. These devices exploit the direct piezoelectric effect, whereby an applied acoustic stress generates an electric potential across a piezoelectric material. Structurally, they consist of a piezoelectric layer sandwiched between metallic electrodes, often complemented by a backing layer for acoustic damping and a front matching layer to optimize impedance coupling with soft tissue (Y. Yang et al., 2013; Zheng et al., 2022).

The resonance frequency is fundamentally determined by the thickness of the piezoelectric element; for instance, a 10 MHz transducer requires a ceramic plate on the order of 200 µm.

At higher frequencies, the requirement of sub-100 µm thickness imposes substantial challenges in fabrication, mechanical fragility, and yield.

Piezoelectric ceramics such as lead zirconate titanate (PZT) dominate clinical ultrasound due to their high electromechanical coupling and sensitivity. Lithium niobate ($LiNbO_3$) offers excellent thermal stability and a high Q-factor, while polymeric films such as polyvinylidene fluoride (PVDF) provide mechanical flexibility and acoustic impedance closer to that of tissue, making them suitable for conformal or intraluminal devices. Nevertheless, each material presents inherent trade-offs in terms of robustness, manufacturability, and frequency bandwidth.

Although highly effective in conventional ultrasonography, bulk piezoelectric transducers reveal key shortcomings when applied to PAI. Their resonant nature leads to a narrowband frequency response, capturing only a limited portion of the inherently broadband photoacoustic spectrum generated by absorbers of varying sizes (D. Yang, Xing, Yang, & Xiang, 2007)

This compromises spectral richness and hampers multi-scale reconstruction. In addition, their physical footprint—typically millimeter-scale—hinders integration with optical excitation modules or wearable form factors. Electrical impedance mismatches, often in the megaohm range, require complex matching networks to couple effectively with modern low-noise amplifiers.

A fundamental constraint is the inverse relationship between resolution and penetration depth. High-frequency ultrasound improves spatial resolution but suffers from strong attenuation in tissue. For instance, a 20 MHz probe with 80% bandwidth provides axial resolution of approximately 40 µm, yet attenuation above 0.5 dB/cm/MHz limits its use to superficial imaging. Conversely, probes in the 1–2 MHz range penetrate several centimeters but sacrifice resolution, making them unsuitable for resolving fine vascular or cellular structures. In PAI, where absorbers generate inherently broadband signals, the inability of bulk probes to capture both low- and high-frequency content severely restricts functional and multi-scale imaging capabilities.

From a critical standpoint, while conventional piezoelectric probes are robust and clinically validated, their technological ceiling is increasingly evident. Efforts to miniaturize them often come at the cost of durability and reproducibility, while attempts to broaden their frequency range have proven challenging due to intrinsic material resonances. This creates a structural barrier to their adaptation for modern PAI systems, where spectral richness and compact form factors are non-negotiable.

1.3.2 MEMS Ultrasonic Transducers

Microelectromechanical systems (MEMS) have emerged as a transformative alternative to bulk piezoelectrics, enabling scalable, miniaturized, and customizable transducers. MEMS fabrication leverages advanced semiconductor processes such as thin-film deposition, surface and bulk micromachining, and deep reactive ion etching (DRIE), thereby achieving wafer-level uniformity and integration with complementary electronics (Suttikittipong et al., 2025; J. Wang, Zheng, Chan, & Yeow, 2020). Their reduced mass and dimensional control allow for frequency tuning and broadband operation, both of which are highly desirable for PAI.

Two principal MEMS architectures have been developed: piezoelectric micromachined ultrasonic transducers (PMUTs) and capacitive micromachined ultrasonic transducers (CMUTs). PMUTs operate in flexural rather than thickness mode, employing thin-film piezoelectric layers such as AlN, ScAlN, or PZT deposited over micromachined membranes.

This configuration yields lower acoustic impedance and a more favorable match with biological tissues, as well as broadband responses in the low- to mid-MHz range (Kumar, Rab, Pant, & Maji, 2018). CMUTs, on the other hand, employ electrostatic actuation across a vacuum gap. Their capacitive structure provides intrinsically wide bandwidth and excellent integration with CMOS electronics, facilitating on-chip multiplexing and signal conditioning.

However, CMUTs typically require high DC bias voltages (20–100 V), which raises concerns for low-power, wearable, or implantable systems.

A direct comparison between PMUTs and CMUTs reveals complementary strengths and weaknesses. PMUTs are more energy efficient in low-voltage environments and inherently better matched acoustically to soft tissue, making them particularly well suited for low-power, wearable, or flexible devices. Their main limitation lies in reduced sensitivity at higher frequencies compared to CMUTs. CMUTs, in contrast, excel in bandwidth and integration density, and their compatibility with standard CMOS processing makes them highly attractive for large-scale imaging arrays. Yet, the requirement for high bias voltages introduces power management and safety concerns, particularly in portable or implantable systems. This divergence in capabilities explains why both PMUT and CMUT development continues in parallel, as each architecture aligns with different target applications in PAI.

Nevertheless, MEMS devices face their own critical barriers. The fabrication of PMUTs with consistent thin-film quality across large wafers can lead to yield challenges, while CMUTs are prone to reliability issues such as membrane collapse and dielectric charging (Ren et al., 2022; Zheng et al., 2022).

Furthermore, while wafer-level integration promises cost reduction, translating laboratory prototypes into robust, biocompatible, and sterilizable clinical tools remains an unresolved challenge. This gap between laboratory performance and clinical reliability highlights a central tension in MEMS development: the balance between the flexibility of microfabrication and the stringent requirements of medical deployment.

More broadly, MEMS transducers bring unique advantages over traditional probes. Their scalability enables the realization of dense arrays with hundreds of elements on a single wafer, reducing cost and improving sensitivity via coherent summation (Khoshnoud & Silva, 2012).

Their planar geometry facilitates co-integration with optical excitation sources such as high-power LEDs, with ASIC-based amplification, and with wireless telemetry modules for untethered operation. Most importantly, their miniaturization potential opens the door to novel device classes—including intravascular catheters, endoscopic probes, and wearable imaging patches—that would be unattainable with bulk piezoelectric technologies.

As a result, while MEMS clearly surpass conventional piezoelectric probes in scalability, form factor, and integration potential, their pathway to clinical adoption requires addressing manufacturing reproducibility, long-term reliability, and regulatory compliance (Inc, 2014). These hurdles define the frontier of current research and development in MEMS for PAI.

To bridge these limitations, researchers have moved beyond single-mode MEMS designs and increasingly pursue multi-frequency and broadband strategies, which are discussed in the following section.

1.3.3 Multi-Frequency and Broadband MEMS Strategies

Despite the progress in MEMS-based ultrasonic transducers, both PMUTs and CMUTs are often constrained by narrowband responses centered on a dominant resonance mode. This limitation restricts the ability to capture the inherently broadband spectra generated in photoacoustic imaging. To address this, recent efforts have focused on multi-frequency designs that leverage modal superposition, geometric variations, and structural optimization to achieve multiple distinct resonance peaks across a wide frequency range (Ren et al., 2022; Zheng et al., 2022).

Several geometrical strategies have been explored, including diaphragms of variable thickness, arrays of cantilevers, and hybrid architectures such as floating or anchored cross-shaped membranes. These structures create multiple vibrational modes, each contributing to different resonance frequencies and thus extending the overall detection bandwidth.

Design optimization is typically performed using finite element modeling (FEM) to predict mode shapes and frequency responses, while laser Doppler vibrometry (LDV) is widely employed for experimental validation of membrane vibration profiles (Pandya, Kim, Roy, & Desai, 2014)

This compilation illustrates several important trends. The choice of resonator shape and size exerts a strong influence on operating frequency. For instance, square PMUT membranes with dimensions on the order of 1000 µm resonate in the low-MHz regime, while circular diaphragms with sub-100 µm diameters can reach into the tens of MHz (Kumar et al., 2018). This scaling relation arises from the dependence of membrane stiffness and mass loading on geometry, highlighting the capacity of MEMS processes to finely tune operational frequency by lithographic control.

The table also underscores the trade-off between frequency and application scope. Devices operating in the sub-MHz to low-MHz regime are well suited for deep tissue imaging due to reduced attenuation at lower frequencies, but they sacrifice spatial resolution (Mohammed et al., 2008)

Conversely, high-frequency PMUTs in the 8–22 MHz range deliver superior resolution for superficial targets but at the cost of reduced penetration depth. Multi-frequency or variable-geometry approaches attempt to bridge this gap by providing broader spectral coverage within a single device architecture. The diversity of MEMS geometries and their corresponding acoustic performance is summarized in the following Table 1.2.

Table 1.2 Similar works for MEMS transducers

Ref	**Shape**	**Dimensions (µM)**	**Resonator Type**	**Frequency (Hz)**
(Y. Yang et al., 2013)	Square	1000 µM	pMUT	2 MHz
(Dangi et al., 2018)	Circular	125 µM	pMUT	10 MHZ
(Zheng et al., 2022)	Variable	Various	pMUT	1-8MHz
(Sun, Wang, Ning, & Zhang, 2022)	Circular	170 µM	pMUT	508 KHz
(Lu, Tang, Fung, Wang, et al., 2015)	Circular	100 µM	pMUT	22 MHz
(Lu, Tang, Fung, Boser, & Horsley, 2015)	Circular	50 µM	pMUT	8 MHz
(J. Wang et al., 2020)	Square	250 µM	cMUT	5 MHz
(H. Wang et al., 2021)	Circular	220 µM	pMUT	1.2 MHz
(Sadeghpour, Zilonova, Hooge, & Kraft, 2021)	Circular	160 µM	pMUT	6 MHz

The inclusion of CMUT devices in this comparative landscape highlights their distinct operating principles. For example, (J. Wang et al., 2020) demonstrated a square CMUT resonator operating at 5 MHz with strong potential for array integration. CMUTs generally offer wide bandwidth and compatibility with CMOS processing, but their dependence on high bias voltages may limit use in low-power or wearable PAI systems.

From the standpoint of PAI, this evidence confirms that no single transducer geometry suffices to cover the entire spectral range needed for multi-scale imaging. Instead, broadband and multi-frequency strategies must be pursued. By combining different resonator geometries, carefully tuning membrane dimensions, and integrating multiple modes within a single array, MEMS devices can provide richer frequency responses that enhance image reconstruction, improve absorber discrimination, and enable simultaneous visualization of structures across different depths and sizes (Zheng et al., 2022).

A critical distinction also emerges when comparing MEMS technologies with conventional piezoelectric probes. Traditional probes are well established, but their bulk dimensions, limited bandwidth, and difficulties in integrating optics and electronics restrict their suitability for modern PAI. MEMS transducers, by contrast, provide miniaturization and form factors compatible with catheters, endoscopes, and wearable devices.

They offer superior scalability through wafer-level fabrication, enabling dense arrays that capture a wider range of frequencies. Most importantly, broadband MEMS arrays have the potential to deliver both high-resolution superficial imaging and deeper tissue penetration, an achievement beyond the reach of conventional piezoelectric devices (Wojciechowski, Boser, & Pisano, 2004).

In addition to these advantages, the detailed design of MEMS resonators strongly influences their broadband behavior. Modal density, or the number of closely spaced resonance modes within a given frequency span, directly determines how uniformly the acoustic spectrum can be sampled. A higher modal density enables smoother frequency coverage but often comes at the expense of reduced Q-factor.

Conversely, high-Q resonators improve sensitivity and signal-to-noise ratio, but narrow the effective bandwidth. Likewise, back chamber design, including the use of air gaps or vacuum cavities behind membranes, plays a central role in tuning compliance and acoustic impedance. These parameters highlight that achieving true broadband operation requires not only structural variation but also a careful balance between sensitivity, stability, and manufacturability.

Yet, challenges remain even in these advanced strategies. Multi-frequency MEMS designs often face fabrication complexity, as achieving consistent modal superposition across large arrays requires sub-micrometer precision. Variability between devices can degrade array-level performance, limiting clinical robustness. Furthermore, while FEM and LDV provide powerful design and validation tools, real-world deployment involves additional constraints such as thermal stability, packaging biocompatibility, and long-term mechanical reliability (Okulov, 2017). These practical considerations highlight that although MEMS broadband strategies are conceptually compelling, significant translational work remains to ensure their scalability beyond laboratory demonstrations.

The packaging and array-level considerations are essential for translation into practical PAI systems. Transparent or back-illumination-compatible encapsulation layers allow co-integration with LED-based excitation, while wafer-scale fabrication ensures large arrays with high device uniformity. When combined with ASIC-based front-end electronics and wireless telemetry, these multi-frequency MEMS platforms move beyond laboratory demonstrations toward fully integrated, portable, and wearable PAI solutions.

1.4 Mechanical Sensing for Photoacoustic Imaging

Photoacoustic imaging fundamentally relies on a delicate triad of interactions between optical excitation, acoustic detection, and mechanical coupling at the interface between sensor and sample. In conventional benchtop systems, mechanical stability is assumed or externally constrained; however, once PAI migrates toward handheld, wearable, or minimally invasive formats, this assumption collapses. The mechanical boundary between the transducer array and the tissue becomes dynamic—subject to micro-motions, pressure fluctuations, and variable acoustic coupling media (gel layers, membranes, air gaps). Even sub-micron deformation or angular misalignment can perturb acoustic impedance and alter time-of-flight or amplitude, resulting in phase errors that compromise image reconstruction, signal coherence, and spectral unmixing accuracy (Erlöv et al., 2021; Mohammed et al., 2008).

The impact of these distortions extends beyond image sharpness. In quantitative PAI, where optical absorption coefficients are estimated to infer oxygen saturation or hemoglobin concentration, unstable coupling introduces multiplicative errors that mimic physiological variation (Taruttis et al., 2016). In multi-wavelength or multi-frequency acquisitions, the lack of mechanical repeatability between frames further distorts differential metrics such as fluence-normalized absorption or acoustic attenuation mapping. Consequently, mechanical stability and its measurement are not auxiliary aspects of PAI—they are prerequisites for reproducible, quantitative performance (B. Park, Oh, Kim, & Kim, 2023).

Traditional solutions, such as external motion-tracking cameras or ultrasound speckle correlation, attempt to infer displacement indirectly (Erlöv et al., 2021). While effective in rigid laboratory setups, these approaches fail in compact or wearable devices, where space, power, and computational budgets are highly constrained. Moreover, they sense motion only at the global scale, overlooking microscopic strain or pressure variations at the acoustic interface—the very phenomena that most strongly influence acoustic coupling.

Embedding co-registered mechanical sensing within the PAI head therefore represents a paradigm shift: instead of estimating motion externally, the system becomes self-aware of its mechanical state. Co-located strain or displacement sensors can report local deformations in real time, providing a direct electrical signature of contact quality, pressure uniformity, and transient motion. When coupled with the acoustic and optical channels, these signals form a feedback loop that enables adaptive acquisition strategies—for example, triggering illumination only during stable contact, calibrating coupling losses dynamically, or compensating for surface curvature and motion in reconstruction algorithms.

The scientific relevance of mechanical readouts extends further. Mechanical information encodes material stiffness, viscoelastic response, and tissue elasticity—parameters that are diagnostically meaningful and complementary to optical absorption. Thus, co-registered mechanical sensing not only stabilizes PAI but also enriches it with an additional contrast dimension, paving the way for hybrid photoacoustic–elastographic modalities that can infer both biochemical and biomechanical properties simultaneously. In the broader context of portable imaging, these developments bring PAI closer to becoming a multimodal, context-aware diagnostic tool rather than a purely optical-acoustic system (B. Park et al., 2023).

1.4.1 Sensing Mechanisms and Associated Power Constraints

Mechanical readouts can be implemented through a variety of transduction mechanisms, each embodying a different trade-off among sensitivity, power consumption, and integration complexity. For PAI systems operating under strict energy and form-factor constraints, these trade-offs are critical.

1.4.1.1 Piezoresistive sensing

Piezoresistive sensors exploit the change in electrical resistivity of a doped semiconductor or metallic film under mechanical strain. They offer a direct and linear relationship between stress and output voltage, making them conceptually simple and readily compatible with analog conditioning circuits. Their disadvantages, however, are intrinsic: continuous biasing is required to sense resistance changes, which leads to non-negligible static power consumption and thermal drift. At the microscale, self-heating and 1/f noise further degrade performance.

Typical operating power ranges from hundreds of microwatts to several milliwatts—orders of magnitude higher than acceptable for wearable or battery-less systems (Mohammed et al., 2011).

1.4.1.2 Capacitive sensing

Capacitive MEMS strain sensors measure the variation in capacitance between deformable plates. Their differential nature provides excellent noise immunity and sub-micron sensitivity, and they are broadly used in accelerometers and pressure sensors. Yet for photoacoustic integration, they pose significant challenges: parasitic capacitance from packaging, the need for alternating-current excitation, and susceptibility to humidity and contamination. Maintaining sub-micron gaps requires complex fabrication and increases integration difficulty with acoustic front-ends (Yoo & Choi, 2021).

1.4.1.3 Optical and interferometric sensing

Optical strain sensors—including Fabry-Perot interferometers, fiber Bragg gratings, and on-chip waveguide structures—deliver nanometer-scale precision and immunity to electromagnetic interference. They have been successfully used in high-end ultrasound probes and laser calibration systems. However, they require external light sources, precise alignment, and optical readout components, making them unsuitable for ultra-compact, battery-operated PAI units. Their power and cost overheads outweigh their precision benefits in consumer or field-deployable systems (Ansari, Zhang, Desjardins, & Beard, 2018).

1.4.1.4 Passive contact-based MEMS sensing

The last category, and the one most relevant to this thesis, consists of direct-contact MEMS strain or displacement sensors. These devices detect mechanical deformation through the closure of micro-fabricated contacts between flexible beams and fixed electrodes (Nguyen, Tanii, Takahata, & Shimoyama, 2019). The resulting binary electrical state (contact or open circuit) eliminates the need for analog amplification or continuous excitation. No energy is consumed until the mechanical displacement reaches the designed threshold. Once contact occurs, a simple pull-up resistor or microcontroller input pin can detect the event digitally (Okulov, 2017).

Table 1.3 Comparative landscape of mechanical strain sensors

Ref	**Type of sensor**	**Sensing Principle**	**Detection Actuator**
(Mohammed et al., 2011)	Strain Sensor	Piezoresistive Layer	Analog Output in function of strain
(Wojciechowski et al., 2004)	Strain Sensor	MEMS Resonator	Resonance frequency shift in function of strain
(Do, Erbes, Yan, Soga, & Seshia, 2016)	Strain Sensor	MEMS Resonator	Resonance frequency shift in function of strain
(Suster et al., 2006)	Strain Sensor	Capacitance	Capacitance variation in function of strain
(Kumar et al., 2018)	Force Sensor	Piezoresistive Layer	Analog Output in function of the force
(Chu, Mills, & Cleghorn, 2008)	Force Sensor	Capacitance	Capacitance variation in function of the force
(Pandya et al., 2014)	Force Sensor	Piezoresistive Layer	Analog Output in function of the force
(Nguyen et al., 2019)	Elasticity Sensor	Piezoresistive Layer	Analog Output in function of deformation
(Moore & Moheimani, 2014)	Displacement Sensor	Capacitance	Capacitance variation in function of strain

This passive principle drastically reduces average power consumption—down to the microwatt or even nanowatt level—and allows integration with low-voltage CMOS electronics. Furthermore, since the sensing event is inherently digital, data acquisition and wireless transmission can be event-driven rather than continuous, conserving both energy and bandwidth.

From a design standpoint, the suitability of a given sensing approach for co-registration with PAI depends on four metrics: (1) resolution and repeatability of displacement detection, (2) total active and standby power, (3) form factor and mechanical compliance with the transducer substrate, and (4) ease of electrical integration. Among the surveyed options, only the passive MEMS contact architecture simultaneously meets all four, justifying its selection for this research (Okulov, 2017).

1.4.1.5 Passive MEMS Strain/Displacement Sensors

Passive MEMS strain sensors exploit a binary transduction mechanism based on controlled mechanical contact. In their rest state, a suspended micro-beam remains electrically isolated from a fixed electrode. External deformation—induced by substrate strain, contact pressure, or vibration—deflects the beam until the designed gap closes. The resulting contact creates an electrical pathway that can be detected as a logic transition. Because no bias voltage or current is required to maintain the open state, the sensor consumes effectively zero power during standby (Mohammed et al., 2008).

This direct-contact paradigm contrasts sharply with the continuous analog readout of piezoresistive or capacitive devices. It transforms mechanical deformation into discrete digital events that can be timestamped, counted, or used as triggers for higher-level system actions such as initiating an image frame or recalibrating acoustic coupling. The simplicity of this mechanism ensures exceptional robustness and immunity to noise: there is no analog drift, no bridge balancing, and no thermal coefficient to compensate.

Integration with PAI Transducers

When co-located with the MEMS ultrasonic transducer, passive strain sensors enable mechanical co-registration of each photoacoustic frame. The MEMS ultrasonic array can detect the acoustic pressure waves generated by optical absorption, while the adjacent strain sensor records local deformation, probe pressure, or drift simultaneously.

Motion and Coupling Compensation

The sensor output can gate image acquisition to periods of mechanical stability, or provide correction factors for variable coupling efficiency. This is crucial in handheld or wearable probes, where gel thickness and applied pressure fluctuate over time.

Elastography-style Mapping

By correlating photoacoustic amplitude changes with local strain readings, one can infer tissue stiffness or elasticity without requiring external ultrasound excitation. This dual-contrast capability transforms a conventional PAI system into a hybrid photoacoustic–mechanical imager.

Mechanical Safety and Feedback Control

In wearable or implantable configurations, the sensors can serve as overload detectors, ensuring that the applied pressure remains within safe limits for tissue or device packaging. From a packaging perspective, the sub-millimeter footprint and planar topology of the sensors make them compatible with flip-chip bonding or flexible-substrate assembly alongside the ultrasonic die. Because both devices are MEMS-based, they share similar mechanical compliance, thermal expansion coefficients, and fabrication materials—minimizing stress mismatch and simplifying encapsulation.

Signals Most Useful for PAI and Related Sensing Platforms

Mechanical signals derived from passive MEMS sensors can be categorized into three operational classes, each contributing differently to imaging stability, quantitative calibration, and biomechanical interpretation.

Gating Signals

Gating signals are instantaneous digital events that synchronize optical and acoustic subsystems. The moment a stable mechanical contact is verified, the LED excitation source can be triggered with precise temporal alignment to the acoustic acquisition window. This ensures that each photoacoustic frame is captured under identical coupling and mechanical boundary conditions. In LED-based systems, where excitation fluence and pulse shape may vary slightly between cycles, gating by contact detection guarantees temporal coherence, suppressing phase errors and improving signal averaging across frames. Such hardware-level synchronization becomes increasingly important in multi-frequency PAI systems, where disparate acoustic bands must be coherently combined to reconstruct broadband images (Xia, Chen, Maslov, Anastasio, & Wang, 2014).

Coupling Calibration Signals

Variations in applied pressure or coupling media thickness directly modulate the acoustic impedance at the transducer–tissue interface. Passive strain sensors placed adjacent to the ultrasound element can therefore act as coupling monitors, continuously quantifying contact pressure or micro-slippage. These calibration signals enable real-time correction of amplitude and phase fluctuations that otherwise degrade quantitative reconstructions. For example, a gradual drift in coupling pressure during handheld imaging may appear as a false change in optical absorption; incorporating mechanical feedback allows the algorithm to decouple optical absorption variations from mechanical artifacts. In advanced implementations, coupling data could even be used to modulate the LED driving current or adapt the acoustic receive gain dynamically, producing an energy-adaptive PAI acquisition loop (Attia et al., 2019).

Deformation and Stiffness Metrics

The temporal evolution of contact events, their hysteresis, and their relative distribution across sensor arrays provide a window into local stiffness and viscoelasticity. When mapped spatially, these measurements can reconstruct an elastographic contrast complementary to optical absorption maps. In soft biological tissues, mechanical stiffness correlates with pathological states such as fibrosis, edema, or tumor infiltration. By capturing strain-dependent signals passively, the same MEMS network that stabilizes imaging can thus also contribute to diagnostic differentiation. This opens the possibility of hybrid photoacoustic–elastographic imaging without requiring external mechanical actuation, where tissue stiffness is inferred directly from passive deformation signatures (Hai, Yao, Li, Li, & Wang, 2016).

Beyond these three canonical signal types, the same sensing principles find broader relevance across biomedical microsystems where mechanical awareness at the point of contact is critical. For instance, in intravascular or micro-endoscopic probes, minute deformations of the probe tip reflect variations in local vascular pressure or wall stiffness. Excessive force at the tip may precede vessel rupture or tissue perforation. Embedding passive MEMS strain sensors near the distal end of such probes allows continuous monitoring of mechanical stress while consuming negligible power and requiring no optical fibers or additional wiring. Their digital, threshold-based response is inherently compatible with miniature catheter electronics, providing a safeguard against accidental over-pressure in delicate anatomical structures (Pandya, Sheng, & Desai, 2017).

Similarly, in implantable or epidermal devices, these sensors can detect subtle strain patterns associated with organ motion, blood pulsation, or tissue swelling. A sub-millimeter MEMS array adhered to cardiac or vascular tissue could, for example, monitor local wall strain to infer hemodynamic load or detect early signs of aneurysmal expansion. In orthopedic implants, integrated strain sensors could quantify load redistribution following surgery, enabling long-term assessment of bone healing or prosthetic performance. The combination of passive operation and digital output aligns with the stringent energy budgets of implanted devices, where continuous analog sensing is infeasible (Jin & Liang, 2021).

In the context of soft robotic or bio-inspired actuators, passive MEMS strain sensors can serve as proprioceptive elements—registering flexion, grip force, or contact feedback without the overhead of active electronics. When co-fabricated with thin-film drivers or flexible substrates, they form part of an integrated sensory network that mimics biological tactile feedback mechanisms. Their binary contact logic simplifies system integration while providing valuable real-time information about the mechanical state of the structure (Lei et al., 2025).

By merging these mechanical readouts with the optical and acoustic channels of a PAI system—or with other physiological sensing modalities such as temperature or impedance—the platform effectively evolves into a multi-domain, self-calibrating diagnostic tool. The convergence of optical, acoustic, and mechanical data not only stabilizes image formation but also introduces richer analytic dimensions for in situ material characterization, physiological monitoring, and closed-loop control of micro-devices operating in dynamic biological environments (Nyayapathi, Zheng, Zhou, Doyley, & Xia, 2024).

Mechanical Awareness as a Design Principle

The integration of passive mechanical sensing into photoacoustic and related systems represents more than a technical refinement; it defines a new design philosophy for intelligent sensing platforms. A mechanically aware system perceives not only the signals it measures but also the mechanical state through which those signals are acquired. As photoacoustic imaging migrates toward handheld, wearable, and minimally invasive architectures, ensuring measurement fidelity amid motion, pressure variation, and environmental perturbations becomes indispensable. Passive MEMS strain sensors provide a route to achieving this fidelity without compromising size, energy efficiency, or manufacturability (Karpiouk, Wang, & Emelianov, 2010).

From a systems perspective, mechanical co-registration closes the feedback loop between excitation, detection, and contact mechanics. It allows photoacoustic devices to autonomously recognize and respond to their mechanical boundary conditions, transforming them from passive recorders into adaptive agents capable of real-time self-correction. This paradigm can extend naturally to smart catheters, microneedle arrays, or implantable acoustic microsystems, where spatially distributed sensors continuously assess mechanical stress to prevent tissue injury or mechanical failure (Hui et al., 2017).

In biomedical research, mechanically aware probes could enable intravascular pressure mapping, micro-surgery guidance, or neurovascular monitoring, where detecting the onset of excessive strain may prevent catastrophic rupture or ischemic damage. Similarly, hybrid PAI–mechanical probes could image vascular morphology while simultaneously quantifying the wall tension that governs hemodynamic risk. These concepts align with the growing trend toward minimally invasive diagnostics that combine multimodal sensing and autonomous safety features in a single miniature platform .

Beyond the medical sphere, the implications of ultra-low-power mechanical awareness are broad. In aerospace engineering, MEMS strain and displacement sensors embedded in aircraft wings or turbine blades can provide early warning of material fatigue, delamination, or vibration anomalies—functions traditionally requiring bulky wired networks. In civil infrastructure, distributed arrays of passive sensors can monitor bridges, tunnels, and pipelines for micro-cracks or load-induced deformation, supporting long-term structural-health assessment with negligible maintenance power. In robotics and industrial automation, such sensors enable lightweight tactile feedback and precision force control, essential for collaborative or bio-inspired robots operating alongside humans (Okulov, 2017; Preethichandra, Suntharavadivel, Kalutara, Piyathilaka, & Izhar, 2023).

1.5 Compact and Integrated Photoacoustic Imaging Systems

In recent years, considerable research effort has been directed toward the development of compact and portable photoacoustic imaging systems aimed at reducing cost, size, and system complexity while preserving clinically relevant imaging performance. Conventional laboratory photoacoustic imaging platforms typically rely on Q-switched lasers and bulk piezoelectric ultrasonic probes, which provide high optical pulse energies and excellent detection sensitivity. However, these systems are often bulky, expensive, and difficult to integrate into portable or wearable devices. As a result, the field has increasingly focused on the development of solid-state optical excitation sources, miniaturized ultrasonic receivers, and integrated system architectures capable of enabling compact photoacoustic imaging platforms (Attia et al., 2019).

Portable photoacoustic systems based on compact pulsed lasers have demonstrated the feasibility of handheld and point-of-care imaging devices. These systems typically employ fiber-delivered laser excitation combined with conventional piezoelectric probes. While such approaches reduce system size compared with laboratory-scale instruments, the laser sources remain relatively costly and require complex optical alignment and power management. Consequently, the development of fully solid-state excitation approaches has become an important research direction for next-generation photoacoustic imaging systems (Beard, 2011).

High-power light-emitting diodes have emerged as promising alternatives to pulsed lasers for compact photoacoustic imaging platforms. LEDs offer important advantages including low cost, mechanical robustness, compact size, and compatibility with low-voltage electronic drivers. Modern high-power LED systems can operate at repetition rates ranging from hundreds of hertz to several kilohertz, allowing signal averaging to compensate for reduced pulse energy. Several studies have demonstrated LED-based photoacoustic systems capable of generating detectable signals in biological tissues and tissue-mimicking phantoms. These systems highlight the potential for low-cost photoacoustic imaging devices suitable for portable and resource-limited environments (Adachi & Hoshimiya, 2013; Allen & Beard, 2016).

Despite these advantages, LED-based excitation presents important challenges. The optical fluence generated by LEDs is typically orders of magnitude lower than that of Q-switched lasers, which limits imaging depth and reduces signal-to-noise ratio. As a result, LED-based systems often rely on high repetition rates and signal averaging to achieve sufficient measurement sensitivity. The electrical driver circuits required to generate short, high-current excitation pulses also represent a key technological challenge. These constraints have motivated the development of specialized high-speed LED drivers capable of producing nanosecond-scale optical pulses while maintaining compact system size and low cost.

In parallel with developments in optical excitation, significant progress has been made toward the miniaturization of ultrasonic detection systems. Conventional piezoelectric transducers remain widely used due to their high sensitivity and established clinical performance. However, their millimeter-scale dimensions and limited integration capability restrict their suitability for compact and fully integrated photoacoustic systems. MEMS ultrasonic transducers have therefore attracted growing attention as candidates for next-generation photoacoustic receivers (Suttikittipong et al., 2025).

MEMS transducers offer several advantages compared with bulk piezoelectric probes, including reduced size, wafer-level fabrication, and compatibility with integrated electronics. Both piezoelectric micromachined ultrasonic transducers and capacitive micromachined ultrasonic transducers have been investigated for photoacoustic detection. These devices enable compact receiver architectures and have demonstrated the feasibility of MEMS-based photoacoustic detection. Nevertheless, many reported MEMS devices remain limited in bandwidth or sensitivity, and relatively few demonstrations have addressed broadband detection suitable for multi-scale photoacoustic imaging (H. Wang et al., 2021).

Another important challenge in compact photoacoustic systems is the mechanical stability of the sensor–tissue interface. In portable and handheld configurations, variations in contact pressure and mechanical coupling can introduce significant measurement variability. Conventional photoacoustic systems typically assume stable mechanical coupling or rely on external positioning systems to maintain alignment. However, these approaches are difficult to implement in compact or wearable devices. The integration of mechanical sensing within the photoacoustic probe represents a potential solution by enabling direct monitoring of displacement and contact conditions during operation. Despite its potential benefits, embedded mechanical sensing has received relatively limited attention in the photoacoustic imaging literature.

Taken together, these developments indicate a clear trend toward compact and fully integrated photoacoustic imaging platforms based on solid-state components. However, most reported systems address only individual subsystems rather than complete integrated architectures. Many compact systems combine LED excitation with conventional ultrasonic probes, while MEMS-based detection is often demonstrated using laser excitation sources. Fully solid-state systems combining compact optical excitation, MEMS-based broadband ultrasonic detection, and embedded mechanical sensing remain relatively unexplored (Hai et al., 2016; Okulov, 2017).

The work presented in this thesis addresses this technological gap by developing and experimentally validating the key building blocks required for a compact MEMS-enabled photoacoustic imaging platform. Avalanche-transistor-driven LED excitation provides a compact and low-cost optical source capable of generating photoacoustic signals under experimentally relevant conditions. Multi-frequency MEMS ultrasonic transducers provide broadband acoustic detection within a miniaturized architecture compatible with integrated systems. Ultra-low-power MEMS mechanical sensors provide direct monitoring of mechanical deformation and acoustic coupling conditions. Together, these subsystems define the technological basis for a future compact and fully solid-state photoacoustic imaging platform.

1.6 Conclusion

The development of integrated photoacoustic imaging systems based on microfabricated components represents a fundamental rethinking of how optical, acoustic, and electronic domains can be co-designed for next-generation sensing applications. This thesis has laid the groundwork for that vision by establishing and experimentally validating the individual technological building blocks required for a future fully integrated photoacoustic microsystem. Rather than attempting to produce a complete instrument, the work presented here focuses on developing, characterizing, and interrelating the essential subsystems that will eventually compose such a platform. It therefore represents the first stage in a broader developmental trajectory—one in which feasibility, compatibility, and energy efficiency are proven before full integration.

The transition from traditional laser-based excitation to solid-state light-emitting diode sources exemplifies this paradigm shift. While lasers provide excellent fluence and spectral purity, their cost, size, and energy demand are incompatible with portable or wearable formats. The thesis demonstrates that these constraints can be overcome through an avalanche-driven pulser and LED array capable of producing nanosecond-level optical bursts with controlled amplitude. This approach retains the affordability and robustness of LEDs while achieving the confinement necessary for photoacoustic generation. Electrical and thermal measurements confirm safe operation within the junction limits and effective optical delivery for signal generation in tissue-mimicking phantoms. The developed architecture establishes a reproducible method for achieving confined, low-cost excitation—a key enabling technology for future compact and energy-aware photoacoustic systems.

On the acoustic side, the research develops and validates microelectromechanical ultrasonic transducers designed to achieve broadband reception within a single element. Using tailored diaphragm geometries and multiple resonant modes, these devices cover a spectral range from approximately 0.3 to 8 MHz, bridging the gap between shallow, high-resolution imaging and deeper penetration regimes. Experimental characterization confirms the predicted broadband response and sensitivity. Although implemented and tested as discrete components, these devices demonstrate that wideband acoustic detection is feasible within microfabrication limits and provide a scalable foundation for later array-level integration.

A third block concerns passive mechanical feedback, addressing one of the main weaknesses of portable and wearable PAI systems—the instability of probe-sample coupling. The thesis introduces MEMS strain and displacement sensors that operate on a direct-contact principle with near-zero standby power. They produce discrete digital signals corresponding to mechanical deformation, allowing coupling pressure, motion, or strain to be monitored with only a few microwatts of total consumption. Their simplicity, compactness, and digital nature make them ideal companions for low-power photoacoustic modules and demonstrate that mechanical awareness can be achieved without complex analog electronics. When positioned near the acoustic element, these sensors provide the contextual information required to stabilize reconstructions and, in future iterations, to extract elastography-style mechanical contrast.

The study also examines the prospects for system-level integration of the optical, acoustic, and mechanical subsystems. Their combined operation was analyzed conceptually, and electrical and thermal interactions were characterized to ensure mutual compatibility. However, monolithic or hybrid physical integration was not implemented in this work, as it would require advanced heterogeneous fabrication and packaging processes beyond the scope of the available facilities. Recognizing these constraints, the thesis defines a clear integration roadmap—outlining how shared substrates, common timing logic, and co-fabrication steps could be realized in future research. In this way, the work positions itself not as the endpoint, but as the starting framework for a long-term effort toward complete microsystem realization.

This thesis establishes the technical feasibility and conceptual foundation for solid-state, mechanically aware photoacoustic imaging. The individual subsystems developed here—confined LED excitation, broadband MEMS ultrasonic detection, and passive mechanical sensing—demonstrate that each of the critical functions required for integrated PAI can be achieved at the microscale with low power consumption and manufacturable processes. Together, they define a cohesive architecture that will guide future integration and optimization efforts. The outcomes of this research therefore serve as the cornerstones of a modular platform from which fully self-contained photoacoustic systems can be built in subsequent work.

The following chapters elaborate on these foundational contributions. Chapter 2 presents the design, simulation, and experimental validation of the avalanche-driven LED pulser, focusing on pulse dynamics, confinement metrics, and optical output performance. Chapter 3 details the design and characterization of the multi-frequency MEMS transducers, including their finite-element modeling, fabrication, and broadband frequency response measurements. Chapter 4 introduces the passive strain and displacement sensors, describing their fabrication, electrical behavior, and integration strategies with acoustic elements for mechanical co-registration. Collectively, these chapters demonstrate the feasibility of each building block and outline how they interconnect conceptually. They establish this thesis not as a final integration report, but as the point of departure for a new generation of compact, low-cost, and intelligent photoacoustic microsystems that will emerge from future research and fabrication advances.

CHAPTER 2

COST-EFFECTIVE PHOTOACOUSTIC IMAGING USING HIGH-POWER LEDS DRIVEN BY AN AVALANCHE OSCILLATOR

Alberto Prud'homme [a] and Frederic Nabki [a]

[a] Department of Electrical Engineering, École de Technologie Supérieure
1100 Notre-Dame West, Montréal, Quebec, Canada H3C 1K3

Paper published in MDPI Sensors special issue *"Photonics for Advanced Spectroscopy and Sensing"*, March 2025

Abstract:

Photoacoustic imaging (PAI) is an emerging modality that merges optical and ultrasound imaging to provide high-resolution and functional insights into biological tissues. This technique leverages the photo-acoustic effect, where tissue absorbs pulsed laser light, generating acoustic waves that are captured to reconstruct images. While lasers have traditionally been the light source for PAI, their high cost and complexity drive interest towards alternative sources like light-emitting diodes (LEDs). This study evaluates the feasibility of using an avalanche oscillator to drive high-power LEDs in a basic photoacoustic imaging system. An avalanche oscillator, utilizing semiconductor avalanche breakdown to produce high-voltage pulses, powers LEDs to generate short, high-intensity light pulses. The system incorporates an LED array, an ultrasonic transducer, and an amplifier for signal detection. Key findings include successful generation of short light pulses with sufficient intensity to excite materials, and the system's capability to produce detectable photoacoustic signals in both air and water environments. While LEDs demonstrate cost-effectiveness and portability advantages, challenges such as lower power and broader spectral bandwidth compared to lasers are noted. The results affirm that LED-based photoacoustic systems, though currently less advanced than laser-based systems, present a promising direction for affordable and portable imaging technologies.

Keyword: photoacoustic imaging (PAI); avalanche oscillator; photoacoustic effect; ultrasonic sensors; port-able imaging systems; acoustic wave propagation

2.1 Introduction

Medical imaging plays a crucial role in diagnosing and monitoring various diseases and conditions. One promising modality that has gained significant attention in recent years is photoacoustic imaging, which combines the advantages of both optical imaging and ultrasound to provide high-resolution and functional information about biological tissues.

The photoacoustic effect, also known as the optoacoustic or thermoacoustic effect, has gained attention in medical imaging due to its ability to provide insights into tissue morphology, function, and composition. This effect involves generating acoustic waves through laser light absorption in tissues (L. V. Wang & Hu, 2012).

Photoacoustic imaging (PAI) combines the strengths of optical and ultrasound imaging. It offers high optical contrast by utilizing selective laser light absorption (Beard, 2011). This feature enables visualization of tissue structures with excellent resolution, surpassing the limitations of pure optical imaging. Furthermore, photoacoustic imaging allows deep tissue penetration, making it suitable for imaging organs like the breast, skin, brain and prostate (L. V. Wang & Hu, 2012).

The PAI mechanism initiates with the delivery of pulsed laser light into the tissue of interest, resulting in selective optical absorption. This absorption induces rapid thermoelastic expansion and subsequent generation of broadband ultrasonic waves. These photoacoustic resultant signals are subsequently captured by ultrasound transducers and converted into electrical signals for computational reconstruction of detailed images (Yao & Wang, 2021). In PAI, lasers serve as the primary light source for tissue excitation. The choice of laser parameters, including wavelength, pulse duration and energy, significantly impacts the imaging outcomes.

The selection of laser wavelength depends on the desired imaging depth and the absorption characteristics of the target tissue. For instance, near-infrared wavelengths between 700 and 1300 nm are commonly employed due to their deeper tissue penetration and absorption by endogenous chromophores like hemoglobin (L. V. Wang & Yao, 2016). The pulse duration and energy levels of the laser pulse affect the photoacoustic signal strength, resolution and potential tissue damage. Shorter pulse durations, ranging from 10 ns to a few hundred nanoseconds, are desirable for higher resolution imaging (Kim, Favazza, & Wang, 2010).

Advancements in laser technology have led to the development of novel laser sources specifically designed for PAI. For instance, optical parametric oscillators (OPOs) offer tunable laser outputs, enabling multispectral imaging for the characterization of different tissue components based on their unique absorption spectra (C. Zhang, Maslov, & Wang, 2010). Fiber-based laser systems have also emerged, offering compact and flexible designs that facilitate the integration of photoacoustic imaging into various clinical settings (Jin & Liang, 2021).

Despite the benefits of using laser systems as excitation sources, their acquisition, maintenance, and operational costs are extremely high. Additionally, power consumption and equipment dimensions complicate the creation of portable systems, which has created a new tendency towards using alternative sources of excitation.

The utilization of light-emitting diodes (LEDs) as a light source in photoacoustic imaging systems offers several notable benefits and considerations. These characteristics contribute to the growing interest and exploration for various imaging applications.

One significant advantage of LEDs is their cost-effectiveness compared to traditional laser sources. LEDs are relatively inexpensive, making them more accessible for research laboratories and clinical settings (Zhu et al., 2018). Furthermore, LEDs have a compact and lightweight design, allowing for the development of portable and handheld photoacoustic imaging systems. The portability and ease of use make LEDs suitable for point-of-care applications and imaging in resource-limited settings.

LEDs also offer flexibility in wavelength selection. By using different LED configurations or employing LEDs with varying peak wavelengths, a wide range of wavelengths can be achieved for multispectral imaging. This enables researchers to explore different optical absorption properties and enhance tissue characterization (L. V. Wang & Yao, 2016).

Another advantage of LEDs is their long operational lifetime. LEDs have a significantly longer lifespan compared to lasers, reducing the need for frequent replacements and maintenance. This characteristic contributes to the cost-effectiveness of LED-based photoacoustic imaging systems.

However, there are limitations associated with using LEDs in photoacoustic imaging. LEDs typically have lower power radiation compared to lasers, which can result in reduced signal-to-noise ratios and imaging depths. The limited power output restricts the imaging of deep-seated tissues or structures (Zhu et al., 2018). Moreover, the spectral bandwidth of LEDs is broader compared to lasers, potentially affecting imaging specificity and the ability to differentiate different tissue components (Laufer et al., 2012).

Light source control typically involves two key aspects: light source control and synchronization with the acoustic detection system. Light source control includes features such as precise current control, modulation capability, and synchronization inputs for external triggering. In the case of lasers, various types can be utilized, such as Q-switched Nd:YAG lasers, optical parametric oscillators, or tunable dye lasers, depending on the specific imaging requirements (Su, Ermilov, Liopo, & Oraevsky, 2013; L. V. Wang, 2009). These laser sources offer the desired characteristics in terms of wavelength, pulse duration, and energy output.

Synchronization between the light and the acoustic detection system is crucial for accurate image acquisition. Timing and triggering circuits ensure precise synchronization between the light pulses and the detection system, enabling efficient capture of the photoacoustic signals (Manwar, Li, Kratkiewicz, Zhu, & Avanaki, 2023). This synchronization allows for the proper temporal alignment of the light excitation and the subsequent acoustic wave detection.

Additionally, modulation techniques can be employed to enhance imaging capabilities. Frequency-modulated continuous wave (FMCW) laser systems, for instance, enable depth-resolved imaging by sweeping the laser frequency and detecting the corresponding photoacoustic responses at different depths (Razansky, Buehler, & Ntziachristos, 2011).

The feasibility of low power portable photoacoustic systems requires the replacement of complex light source control systems, which must be capable of generating electrical pulses with durations in the nanosecond range and capable of obtaining the maximum amount of light from the LEDs, for which high voltages and currents are used. An affordable, low-cost option capable of delivering the necessary performance is to use an avalanche oscillator.

The avalanche oscillator (AO), also known as the avalanche transit-time oscillator (ATT), has potential applications in photoacoustic imaging when used with LEDs. By leveraging the principles of avalanche breakdown in semiconductor devices, the AO can generate high-voltage pulses suitable for driving LEDs in photoacoustic imaging systems.

In these applications, a reverse-biased p-n junction diode or a bipolar transistor serves as the active device in the AO circuit. When a reverse voltage is applied, the device operates in the reverse-biased breakdown region, leading to avalanche breakdown and the rapid generation of high-voltage pulses. By appropriately designing the device geometry, selecting the bias voltage, and optimizing other parameters, the AO can produce pulses at frequencies suitable for driving LEDs used in photoacoustic imaging.

The purpose of this work is to evaluate the feasibility and characterization of an avalanche oscillator exciting a high-power LED to be implemented as a basic photoacoustic imaging system, establishing the basis for future optimization work for a cost-effective portable photoacoustic imaging system.

2.2 Materials and Methods

This work comprises three primary components, which must function synergistically to establish the photoacoustic imaging system. The first component involves an avalanche oscillator responsible for generating pulses to drive the LED array. The second component includes an amplifier for the ultrasonic transducer, which facilitates the detection of the ultrasonic echo produced by the sample. Finally, the third component encompasses the characterization setup, designed to conduct comprehensive testing under specific conditions, thereby validating the anticipated outcomes.

An avalanche oscillator is an electronic circuit that exploits the avalanche breakdown phenomenon in semiconductor devices to generate high-frequency oscillations. This phenomenon occurs when a high voltage is applied to a semiconductor junction, causing a rapid and uncontrolled increase in current as electrons gain sufficient energy to ionize atoms in the lattice, leading to a chain reaction of generated electron-hole pairs. This highly non-linear process can produce oscillations in the microwave frequency range, often reaching several gigahertz.

The circuit typically includes a transistor or diode biased beyond its breakdown voltage, along with resonant circuits to stabilize the frequency of oscillation. The abrupt nature of the avalanche breakdown results in sharp current pulses, which, when coupled with a resonant LC circuit or a strip line resonator, can sustain oscillations at very high frequencies (Jinyuan et al., 1998).

Avalanche oscillators are critical in applications requiring stable and precise high-frequency signals. They are commonly used in microwave communication systems, radar equipment, and signal generation for test and measurement instruments. One of the primary advantages of avalanche oscillators is their ability to achieve higher frequencies than many conventional oscillators, making them valuable in advanced electronic and communication technologies. Moreover, their simplicity and ability to generate large power outputs with minimal external components make them an attractive option for high-frequency circuit design (Culshaw, Giblin, & Blakey, 1975).

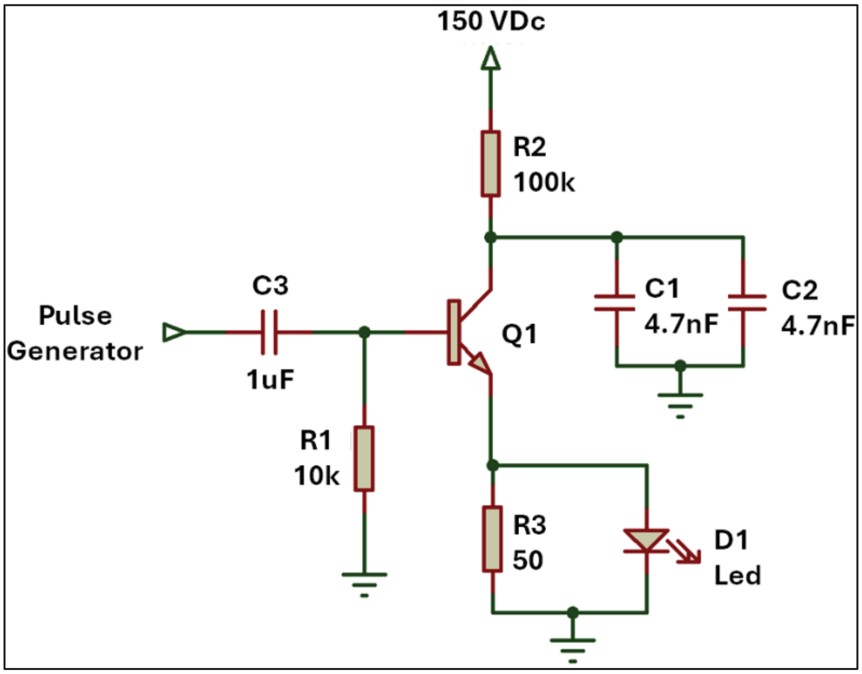

Figure 2.1 Diagram of the avalanche oscillator with LED

The avalanche oscillator in Figure 2.1 was designed utilizing the Diodes Incorporated FMMT413TD avalanche transistor, which has a peak current of 50A and a breakdown voltage exceeding 150V. The oscillator is powered by a 150V DC source GW INSTEK GPE-2323, which is just below the breakdown level. The choice of passive components was made in accordance with the manufacturer's guidelines to achieve a pulse of up to 50A and a duration in the range of a few nanoseconds.

In the avalanche circuit used for this work, the resistor R_2 plays a crucial role in regulating the current that charges capacitors C_1 and C_2, so the voltage across the capacitors gradually increases. This process continues until the voltage reaches the breakdown voltage of the transistor. At this point, the transistor enters the avalanche breakdown region, resulting in a rapid discharge of the capacitors. This discharge generates a pulse with a duration on the order of a few nanoseconds, characterized by extremely high current in this case of 50A.

In this work, the actual transistor breakdown voltage, approximately 160V, was intentionally not used. Instead, an alternative method was employed to induce discharge by applying an external pulse to the base of the transistor. This pulse initiates the quick discharge in the transistor for the voltage across the capacitors to reach the LED.

In order to control the oscillation frequency, a function generator (RIGOL DG1022) producing a 1V square wave with a 5% duty cycle is employed. This setup effectively triggers the discharge of the capacitors. The signal from the function generator was filtered and biased using components C_3 and R_1, resulting in a stable avalanche oscillator with uniform pulse amplitude and period. By adjusting the frequency of the base pulses, the postprocessing of the signal was significantly facilitated, reducing the noise factor during the self-oscillation of the closed-loop avalanche transistor.

The characterization of the oscillator was conducted using a RIGOL MS05104 oscilloscope. The tests presented in this work were conducted using a configuration with a 100 MHz bandwidth and an 8 GSa/s sampling rate, providing nanosecond-range resolution.

The array of LEDs can include multiple devices to increase the body excitation area during exploration. This approach has been demonstrated in other studies to enhance performance (Hariri et al., 2018). However, for the characterization phase of this study, only one LED was utilized, enabling the full luminous capacity to be focused on small areas and reducing the impact of disparities among the physical properties of each LED.

The LED used was the OSRAM SBRM4.24-V6V9-1-1-700-R33 with a central wavelength of 660 nm. Each LED has a Luminous Flux of 1040mW, with a forward voltage potential of 2V and a current of 1.4A.

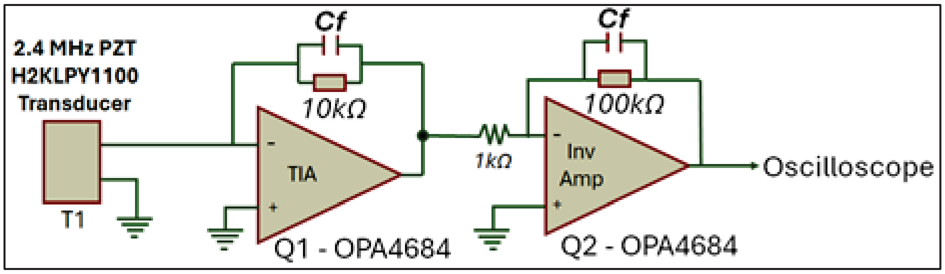

Figure 2.2 Schematic of the amplification circuit

The wavelength employed in the LED can span a wide range, nevertheless, 660 nm was selected owing to its capability to excite both organic and synthetic materials, thereby affording greater versatility during the preliminary

stages of this study. Subsequently, LEDs having different wavelengths can be substituted without compromising the integrity of the system (Adachi & Hoshimiya, 2013; Meng et al., 2019).

In order to effectively capture the ultrasonic signal emitted after the light pulse excitation, the essential components encompass an ultrasonic transducer, in conjunction with a high-gain, low-noise amplifier is required. Figure 2.2 depicts the setup used in this work, which includes a transimpedance amplifier (TIA) OPA4684 from Texas Instruments as the first stage, followed by a series-connected inverting amplified powered by a symmetric power supply of +/-2.5V.

A critical component in the reception stage is the ultrasonic transducer, where the central frequency, directionality type and bandwidth impact its sensitivity, affecting resolution and maximum detection depth. The most commonly used transducers range in frequency from 1 MHz to 20 MHz, with higher frequencies providing greater resolution but reduced depth capability (Manwar et al., 2022; S. Park, Mallidi, Karpiouk, Aglyamov, & Emelianov, 2007). The ultrasonic transducer used in this work was the H2KLPY1100 from Unictron with a central frequency of 2.4MHz with a linear pattern perpendicular to the front face of the device.

One of the significant limiting factors in the application of devices employing LEDs as light sources lies in the inherent rising and dropping times characteristic of the LED.

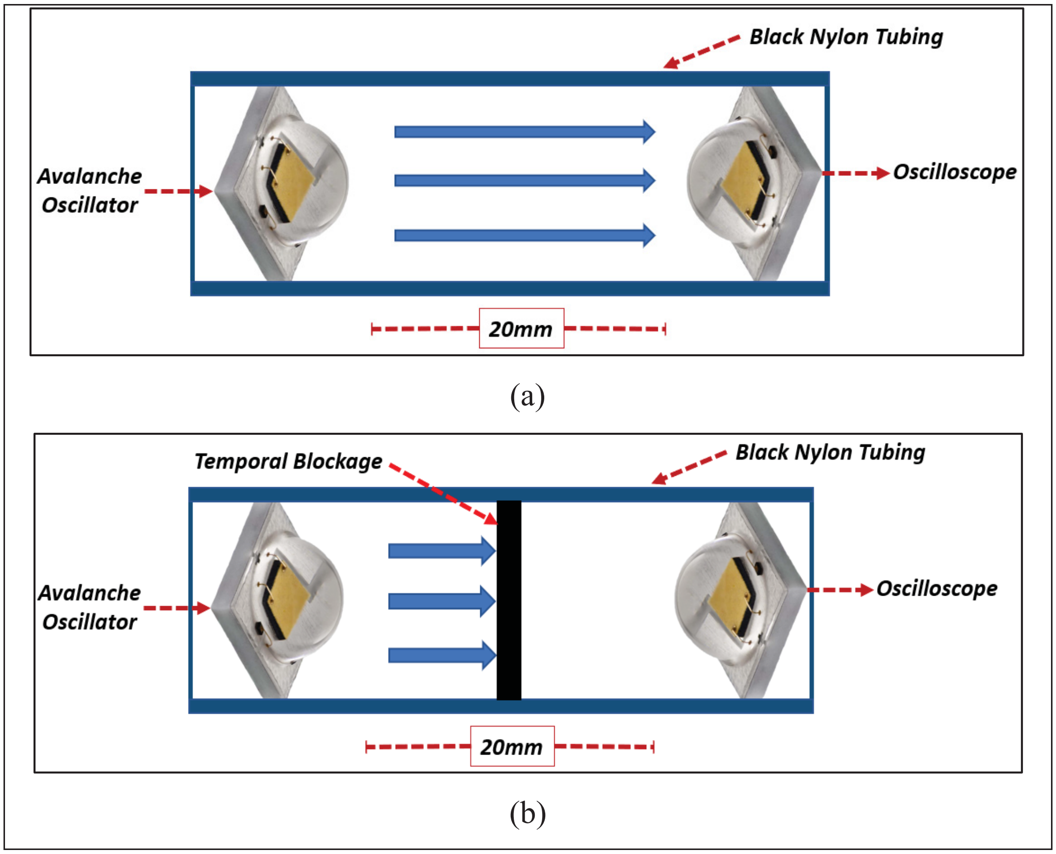

(a)

(b)

Figure 2.3 (a) Light pulse duration measurement setup without temporal blockage, (b) light pulse duration measurement setup with blockage

While it is feasible to measure the rise time and the duration of the electrical pulse with a high degree of accuracy using conventional electronic testing methodologies using an oscilloscope, determining the exact duration of the resultant optical pulse presents a more complex challenge.

Figure 2.3a shows the diagram of the setup used for measuring the duration of the light pulse generated by the LED. This was carried out using another LED of the same model placed inside a black nylon tube to prevent external light contamination. Using the same LED model ensures that the sensitivity of the receiving device is within the same range as the emitting source. In Figure 2.3b, the same setup is shown but with a black nylon plastic body between the two LEDs, preventing light from passing through the tube.

By comparing measurements taken with and without the optical blockage, it becomes possible to directly evaluate and isolate the system's response, ensuring the signal originates solely from the optical excitation of the LED. For the measurement of the light pulse, an oscilloscope was used with the LED directly connected with a 5-ohm resistor in parallel, ensuring rapid discharge after LED excitation. The resistor value was carefully optimized through extensive testing to prevent any influence on the measured pulse duration. The selected low resistance minimized the RC time constant of the circuit, thereby preserving the rise and fall times of the pulse. Although the resistor affected the pulse amplitude, its contribution to the RC time constant was negligible. It is important to note that the LED's inherent capacitance can extend pulse duration when combined with higher resistance values due to an increased RC time constant. By choosing a 5-ohm resistor, the impact of the LED's capacitance was effectively minimized, maintaining the temporal characteristics of the light pulse.

Once the pulse duration was confirmed, it was essential to evaluate whether the light pulse's intensity and duration were sufficient to excite the material and induce the generation of an ultrasonic signal. This assessment involved verifying that the material's response to the light pulse was adequate and that the generated ultrasonic signal was of sufficient amplitude. Furthermore, it was necessary to determine whether the amplifier could adequately amplify the ultrasonic signal for effective detection and analysis by the oscilloscope. This evaluation ensured the proper operation and reliability of the entire system, from light pulse generation to ultrasonic signal detection.

For the experiment, a black polyethylene membrane was selected for evaluation due to its high absorption of the light spectrum emitted by the LED, making it an appropriate material for this test (S. L. Chen, Huang, Ling, Ashkenazi, & Guo, 2009). Figure 2.4 illustrates the test setup, which consisted of a white PETG plastic casing fabricated using 3D printing. The LED was positioned on one side, oriented toward the centroid of the casing, while an Electret microphone (model CMEJ-0627-42-SP from CUI DEVICES) was placed on the opposite side. The microphone was directly connected to the TIA and subsequently to the oscilloscope.

The membrane was positioned equidistantly between the LED and the microphone, with a distance of 4 mm from each component and a negligible thickness of approximately 0.1 mm. Measurements were taken with and without the membrane in place. This approach confirmed that the signal captured by the microphone originated from the photoacoustic effect of the membrane in response to the light pulse.

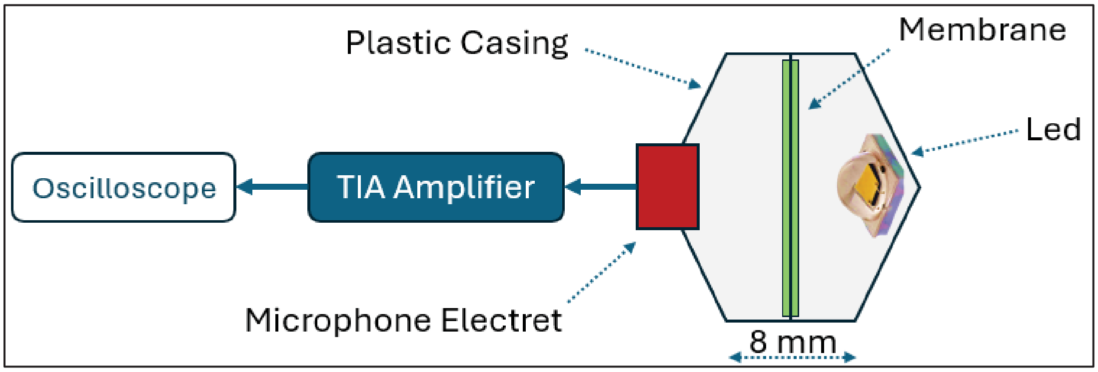

Figure 2.4 Experimental setup showing the LED, microphone, and black polyethylene membrane in a 3D-printed PETG casing for photoacoustic signal detection in air.

Figure 2.5 illustrates the setup for the latest characterization test, designed to evaluate the system under conditions closely resembling real-world applications. In this setup, the driving medium was distilled water with a total dissolved solids (TDS) level of less than 1 ppm to minimize electrical noise and undesired induction, as the entire system was submerged. A rectangular Pyrex recipient was used to house the setup.

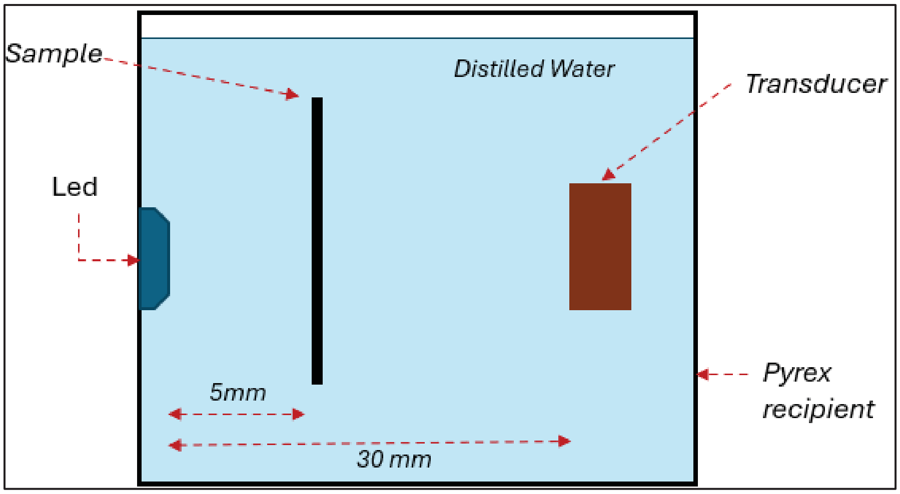

Figure 2.5 Experimental setup for system characterization in distilled water, showing the LED, transducer, and chlorophyll sample in a Pyrex recipient.

The excitation source was the same LED used in previous tests, secured to one of the recipient's inner surfaces and sealed with cold silicone. This sealing prevented contact between the LED's cables and pads with the water, reducing the potential for signal noise. The transducer was positioned at the same height as the LED, aligned with a 30 mm separation.

The sample for this study was a concentrated solution of pure chlorophyll supplied by Trophic. This chlorophyll concentrate was selected due to its spectral absorption characteristics, which closely match the 660 nm wavelength emitted by the LED. Chlorophyll exhibits primary absorption peaks between 430 nm and 452 nm (blue-green region) and a secondary absorption band from 642 nm to 682 nm (red region) (Aboonajmi & Faridi, 2016; M. Chen & Blankenship, 2011). These absorption regions have comparable coefficients, enabling efficient utilization of the chlorophyll concentrate under experimental conditions.

The chlorophyll solution was contained within a capillary tube (model WG-1364-1.7) from SP Wilmad-LabGlass. The tube, made of Pyrex, was 100 mm long with an outer diameter of 1.7 mm and an inner diameter of 1.3 mm. It was positioned 5 mm from the LED at the midpoint of the liquid column, ensuring the light beam maximally illuminated the tube containing the sample.

2.3 Results

The initial test, conducted prior to evaluating the photoacoustic effect, aimed to validate the operation of the avalanche oscillator. The circuit, shown Figure 2.1, was assembled to determine the transistor's actual breakdown voltage. At 159 V DC, the transistor exhibited erratic oscillations, indicative of near-threshold behavior. Stable oscillations were achieved at 160 V DC, with an average frequency over a second of 2.79 kHz, a pulse width of 22 ns (10% to 90% amplitude). The output waveform reached a peak voltage of 142 V DC, confirming stable oscillator performance under higher voltage conditions.

These results validate the oscillator circuit's reliable operation and its capability to generate high-intensity pulses with short durations, demonstrating its suitability for the intended application. Subsequent tests were conducted using a 150 V DC power supply, with the transistor discharge controlled by short pulses. To improve the control over the generated pulses, an external 1 V pulse was used.

This external pulse allows for more precise control of the pulse generation, enabling easier management of the averaging process, metrics, and post-processing. By synchronizing the pulse with the system, the control over the oscillation frequency and data consistency is significantly improved, facilitating more accurate analysis and measurements.

The subsequent test aimed to evaluate the pulse duration generated by the oscillator at a supply voltage of 150 V DC. A burst of 50 pulses of 1 V DC was used to directly discharge the capacitors into the LED, and the output signal was subsequently averaged. Figure 2.6 presents two graphs: Figure 2.6a shows the measurement at the oscillator output with no LED connected, only a 50-ohm resistor to ground.

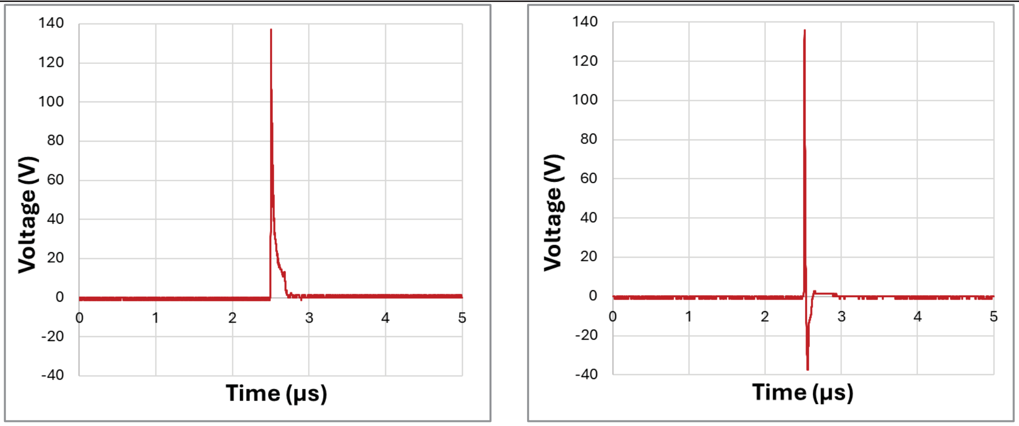

(a)

(b)

Figure 2.6 Oscillator output pulse measurements: (a) without LED connected, using a 50-ohm resistor; (b) with LED connected to the oscillator output.

The subsequent test aimed to evaluate the pulse duration generated by the oscillator at a supply voltage of 150 V DC. A burst of 50 pulses of 1 V DC was used to directly discharge the capacitors into the LED, and the output signal was subsequently averaged. Figure 2.6 presents two graphs: Figure 2.6a shows the measurement at the oscillator output with no LED connected, only a 50-ohm resistor to ground.

In this configuration, the pulse duration was 39.3 ns with a standard deviation (STD) of 0.51 ns equivalent to a variation of 1.3%, with a peak voltage of 137 V with a STD of 2.94 V. As expected, the pulse duration was longer due to the absence of an LED load at the oscillator output.

Figure 2.6b shows the results of the same test with the LED connected to the oscillator output as configured in Figure 2.1. In this case, the pulse duration was 19.5 ns with a STD of 0.57 ns equivalent to a 2.9% variation, with a peak amplitude of 134 V with a STD of 5.56 V. Additionally, the discharge phase of the capacitor, influenced by the small capacitance of the LED, was observed after the electrical pulse ended.

Considering these specifications, the corresponding energy per pulse was calculated to be approximately 13.37 μJ. This parameter is critical for evaluating the system's photoacoustic signal generation and facilitates direct comparisons with previously reported LED-based photoacoustic sources.

This test demonstrates that a simple avalanche oscillator can excite a high-power LED for durations under 50 ns, delivering a current of 50 A and more than 130 V. This provides sufficient energy to emit a short, high-intensity light pulse.

While the results confirmed the generation of short, high-amplitude electrical pulses, one limitation of LEDs in photoacoustic systems is their relatively slow transition from being completely off to reaching peak intensity, as well as their recovery time. To address this, the subsequent test measured the duration of the light pulse emitted by the LED. The same LED model was used, positioned as illustrated in
Figure 2.3.

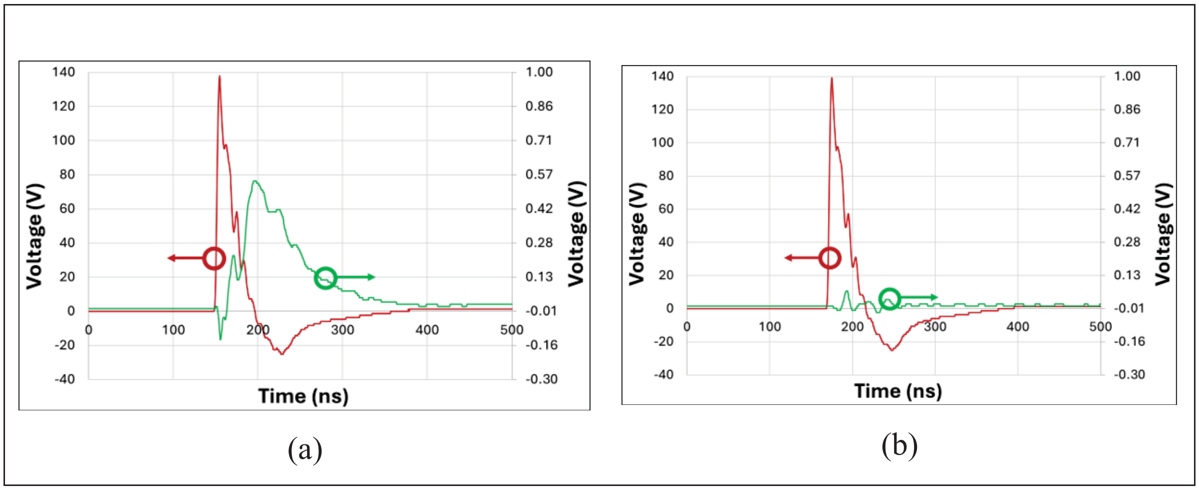

(a)

(b)

Figure 2.7 Comparison of electrical and optical pulse measurements. Electrical pulse supplied to the LED (red) and corresponding light pulse measured by the TIA (green). (a) Pulse duration measurement without blockage, and (b) pulse duration measurement with blockage

Figure 2.7 shows the results obtained from the optical pulse measurement. Figure 2.7a shows the response of the LED functioning as a sensor, represented by the green line, while the red line corresponds to the electrical pulse supplied to the other LED serving as the emitter.

Figure 2.7b presents the same signals but with the blockage placed between the LEDs. Note that LEDs exhibit similar rise and discharge times. For practical purposes, the duration of the measured electrical pulse can be approximated as half of the generated optical pulse.

In Figure 2.7b, a slight disturbance is observed during the electrical pulse, attributed to the electromagnetic pulse generated by the short, high-intensity pulse. This disturbance is unrelated to the emitted light, as the LEDs are optically isolated. In Figure 2.7a, the signal obtained from the TIA peaks at 0.54 V with a duration of 71.5 ns with a 2.12 ns STD equivalent to a 2.9% variation. Given that both LEDs exhibit similar electrical properties, the emitted light pulse can be estimated to have a duration of approximately 36 ns—roughly double the duration of the electrical pulse. While the LED's response is slower than that of a laser, it is sufficiently short for photoacoustic system applications.

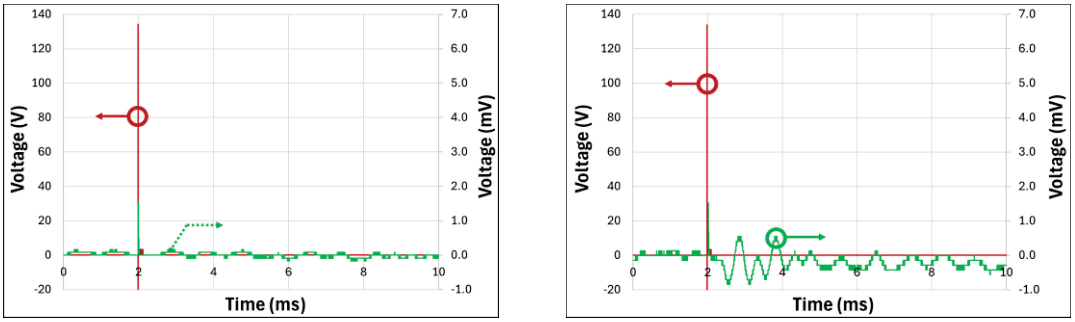

(a)

(b)

Figure 2.8 Acoustic signal evaluation: (a) TIA output without a membrane, showing no acoustic response (green) from the electrical excitation signal from the oscillator (red); (b) TIA output with a membrane, showing a detectable acoustic response (green) following the electrical excitation pulse (red).

After confirming the light pulse duration within the range suitable for such systems, a preliminary evaluation was conducted to assess whether the emitted light intensity was sufficient to excite a material compatible with the wavelength used.

For this test, the setup shown in Figure 2.4 was employed, enabling the precise measurement of acoustic signals generated by light pulses incident on the membrane. The acoustic pulses were captured by a microphone within the casing.

Figure 2.8 presents the results of these tests, with and without the membrane, conducted under the same parameters as the pulse duration tests to ensure consistency in system evaluation. In Figure 8a, the membrane was not included in the test, and the red line represents the electrical signal from the oscillator, while the green line shows the TIA output voltage from the microphone. A short-duration peak with an amplitude of up to 1.6 V is observed, caused by electromagnetic interference during the electrical pulse. However, this peak is unrelated to the recorded acoustic signal. As expected, no acoustic response is observed, as the light intensity was insufficient to excite any casing material at that distance, and no membrane material was present.

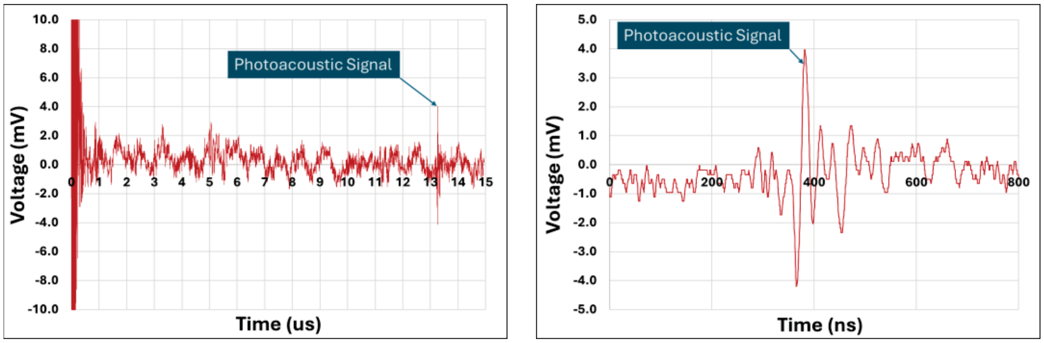

(a) (b)

Figure 2.9 (a) Photoacoustic signal measured in water, (b) Zoomed-in view of the photoacoustic signal measured in the water

In Figure 2.8b test results are shown with the membrane present. The green curve represents the acoustic response captured by the microphone following the light pulse that excited the membrane within the casing. The signal exhibits a maximum amplitude of 0.55 V and a frequency of approximately 1.55 kHz, which depends on the mechanical properties of the membrane and casing. The observed response is a damped acoustic wave, consistent with expected behavior.

These results demonstrate that the LED, when driven by the oscillator, emits sufficient light intensity to excite the membrane and generate a detectable acoustic pulse. This finding highlights the potential of LEDs as a simple and effective method for producing acoustic signals without requiring complex instrumentation, validating the system's operation.

The final experiment aimed to assess the luminous intensity emitted by the LED to excite a sample submerged in water. Water was chosen as an effective medium for simulating photoacoustic wave behavior, mimicking real-world conditions. Given the speed of sound in water at approximately 1497 m/s, the distance between the excited sample and the ultrasonic transducer was calculated accurately.

Figure 2.9 illustrates the measurements obtained at the TIA output, which monitored the ultrasonic transducer's detected signals. Figure 2.9a shows the full duration of the measurement, including the initial emission pulse, which generates electrical noise captured by the system. This range also importantly encompasses the subsequent acoustic signal detected by the transducer after the LED light pulse excited the sample.

The average acoustic signal detection time was approximately 13.25 µs, consistent with the calculated distance between the sample and the transducer. This confirms that the LED's luminous intensity was sufficient to excite the sample and generate an ultrasonic pulse detectable by the transducer across a water media.

The detected photoacoustic signal in water shown in Figure 2.9b exhibits a maximum amplitude of approximately ±4.0 mV, which presents a significant challenge in terms of the signal-to-noise ratio (SNR). The SNR is a critical parameter that defines the system's ability to distinguish the useful signal from background noise. In this case, the maximum amplitude of the detected signal is ±4.0 mV, while the background noise, measured under similar conditions, shows a maximum amplitude of ±1.2 mV. The SNR is calculated as the ratio of the maximum signal amplitude to the maximum noise amplitude, resulting in an SNR of approximately 3.33 (10.5 dB). This ratio is relatively low, indicating that the signal can be susceptible to noise interference, especially considering the high gain of the TIA used in the system.

To enhance the SNR and mitigate the impact of noise, signal averaging was employed. With 50 samples averaged per measurement, and a LED pulse rate of 100 Hz, the SNR improves, though at the cost of a reduced system refresh rate, which is limited to 2 Hz. While this refresh rate is significantly lower than typical commercial systems, it is necessary to attenuate the noise and improve the reliability of photoacoustic signal detection.

It is important to note that this trade-off between SNR improvement and temporal resolution has significant implications for the system’s ability to capture rapid dynamic changes in the signal. The reduced refresh rate affects the temporal resolution and, consequently, the imaging depth. However, this challenge could be addressed through advancements in amplifier design, improved cable shielding, and more effective electrical noise isolation. These optimizations would reduce the need for extensive averaging, allowing for higher sampling rates without sacrificing SNR, thereby improving both temporal resolution and imaging depth, ultimately leading to more precise and reliable photoacoustic measurements.

2.4 Discussion

The results of this study demonstrate the feasibility of employing a simple and cost-effective avalanche oscillator to generate electrical pulses capable of driving a high-power LED to produce light pulses suitable for PAI systems. Unlike conventional PAI setups that rely on

Nd:YAG lasers, which remain the industry standard, or alternative LED-based approaches that utilize laser pulse generators and advanced pulse-shaping electronics, this work eliminates the need for such costly and complex equipment. The avalanche oscillator directly produces short-duration pulses without requiring external pulse-shaping circuits, reducing overall system complexity and improving portability while maintaining effective optical excitation for PAI applications.

Table 2.1 summarizes various studies that have investigated alternative devices to Nd:YAG lasers, primarily employing laser diodes and LEDs. However, a key distinction of those works is their reliance on sophisticated pulse generation hardware, which significantly increases cost and limits accessibility.

Table 2.1 Alternative works about photoacoustic systems

Ref.	Wavelength	Pulse duration	Sample Rate	Average	Transducer
(Joseph Francis et al., 2020)	850 nm	70 ns	4 KHz	64	7 MHz
(Bulsink et al., 2021)	750 nm	70 ns	4.2 KHz	20	7.1 MHz
(Zhu et al., 2018)	850 nm	100 ns	4 KHz	384	10 MHz
(Janggun et al., 2020)	850 nm	35 ns	1.5 KHz	200	7 MHz
(Van Heumen et al., 2023)	940 nm	70 ns	4 KHz	640	7 MHz
(Zeng et al., 2014)	905 nm	100 ns	800 Hz	128	4.53 MHz
(Allen & Beard, 2016)	580 nm	200 ns	500 Hz	1000	3.5 MHz
(Dai, Yang, & Jiang, 2017)	405 nm	200 ns	40 KHz	4000	2.25 MHz
T.W.	660 nm	19.5 ns	100 Hz	50	2.4 MHz

The wavelengths utilized in the referenced studies range from 405 nm to 940 nm, depending on the optical properties of the biological tissues under investigation. The proposed system employs a 660 nm LED, well within the biologically relevant range, and its driving circuit can be readily adapted for alternative LED wavelengths, allowing optimization for specific imaging applications.

Pulse durations reported in these studies range between 35 ns and 200 ns. The avalanche oscillator developed in this work generates pulses as short as 19.5 ns, demonstrating its capability to produce even shorter pulses than those typically used. This flexibility allows for an increase in emitted power by easily adjusting the pulse duration. This shorter pulse width allows for increased peak optical power, potentially improving imaging contrast and penetration depth. Additionally, the system provides a level of tunability, enabling adaptation to specific diagnostic needs without the need for complex external pulse-shaping electronics.

Sampling averages in these studies vary significantly, from as few as 20 samples to as many as 4000, reflecting trade-offs between signal-to-noise ratio and temporal resolution. Sample rates reach up to 40 kHz, demonstrating the capabilities of advanced optical diagnostic equipment. The avalanche oscillator developed in this work operates at a frequency of 2.79 kHz in a closed-loop configuration. While this frequency is lower than some commercial LED-based systems, the design allows for straightforward adjustments via circuit modifications or external control signals, making it highly adaptable to diverse application requirements.

Furthermore, the ultrasonic transducer used in this study operates at 2.4 MHz, which is within the range reported in the literature (2.2 MHz to 10 MHz). While some advanced systems utilize transducers up to 20 MHz, the selection of 2.4 MHz ensures a balance between resolution and cost-efficiency, reinforcing the practicality of the proposed system for point-of-care and portable applications.

Table 2.1 highlight the potential of the proposed device as a viable alternative to more sophisticated and expensive systems. Unlike prior LED-based PAI systems, which typically require external laser pulse generators, this work achieves comparable pulse characteristics with a much simpler and more cost-effective approach. Moreover, the system's modularity opens opportunities for integrating multiple LEDs to further enhance optical power output, expanding its applicability across various PAI modalities. This research establishes a foundational step toward the development of highly accessible and scalable LED-based PAI systems, paving the way for future optimizations and broader adoption in biomedical imaging.

The slower response time of LEDs compared to lasers inherently affects both imaging speed and spatial resolution. Given the actual oscillator configuration, the system can operate at a sustained frequency of 2.79 kHz in closed-loop mode. Assuming the same averaging of 50 samples, this would yield a final imaging frame rate of 55 Hz. Furthermore, the system configuration could be optimized to further increase this frequency. However, such optimizations fall beyond the scope of this work.

In terms of spatial resolution, the system employs a 2.4 MHz transducer, which sets a theoretical axial resolution of approximately 320 μm in water, calculated based on the acoustic wavelength. The lateral resolution is primarily governed by the LED's illumination profile and the numerical aperture of the transducer, leading to an estimated resolution in the sub-millimeter range. While these values indicate a modest compromise in resolution compared to laser-based systems, they align with the goal of developing a cost-effective and portable alternative for photoacoustic imaging applications. Future optimizations, including narrower LED pulse widths and improved detection techniques, could further enhance the system's imaging performance.

The broader spectral bandwidth of LEDs presents both challenges and opportunities for photoacoustic imaging. While it may introduce spectral crosstalk between chromophores, potentially reducing imaging specificity, it also enables the possibility of multispectral imaging without requiring multiple narrowband laser sources. Crosstalk can arise not only from the

LED’s broad emission spectrum but also from overlapping absorption spectra of different chromophores, variations in tissue composition, and optical scattering effects that mix signals from adjacent regions. Additionally, acoustic crosstalk can occur due to limited spatial resolution, where signals from multiple absorbers within the ultrasound focal region become indistinguishable. Achieving effective spectral separation would necessitate additional hardware, such as bandpass optical filters, or software-based spectral unmixing algorithms to isolate specific chromophores. Regarding real-world applications, tissue scattering remains a key limitation, as the LED’s lower peak power reduces penetration depth compared to lasers, making deep-tissue imaging more challenging.

For future biomedical applications, it is essential to consider safety aspects such as LED power limits and potential thermal effects on tissues. While the current work utilizes synthetic materials for testing, transitioning to biological samples introduces additional considerations.

The power of the LED, specifically in terms of its irradiance and the resulting tissue heating, must be carefully controlled to avoid thermal damage to surrounding tissues. The use of pulsed LEDs may reduce the risk of thermal accumulation; however, careful calibration is necessary to ensure that the pulse duration and intensity remain within safe limits for biological tissues. Lasers, which are often employed in more advanced systems, can offer significantly higher power levels than LEDs, raising further concerns about the potential for tissue damage if not carefully managed.

Furthermore, the ethical implications of using photoacoustic imaging in biological tissues should be acknowledged, particularly with regard to tissue exposure to optical radiation. Establishing clear safety protocols for optical power limits and pulse parameters, as well as conducting in vivo safety assessments, will be important as the technology progresses toward clinical applications. However, these considerations are beyond the scope of this work, which focuses on the development of the underlying technology and system performance. Addressing these concerns will ensure the safe integration of this system into biomedical diagnostics while maintaining its effectiveness in non-invasive imaging.

2.5 Conclusion

This work has successfully demonstrated the feasibility of utilizing an avalanche oscillator to drive high-power LEDs for photoacoustic imaging applications. By leveraging the avalanche breakdown phenomenon, the oscillator generated high-voltage pulses with durations suitable for exciting LEDs, which subsequently emitted intense light pulses capable of inducing measurable photoacoustic effects.

The experimental results validated the effectiveness of the proposed LED-based photoacoustic imaging system. The system demonstrated the ability to produce detectable photoacoustic signals in both air and water environments, confirming its potential for diverse applications. The use of distilled water as a medium allowed for accurate simulation of real-world conditions.

Compared to traditional laser sources, LEDs offer several key advantages, including lower cost, compact size, and long operational lifetimes. While LEDs exhibit slower response times and broader spectral bandwidths than lasers, the findings show that they are sufficiently capable of generating high-intensity light pulses for inducing photoacoustic responses. These attributes make LEDs particularly attractive for portable and point-of-care imaging systems, where affordability and ease of integration are important.

This work underscores the potential of combining cost-effective components, such as avalanche oscillators and high-power LEDs, to develop photoacoustic systems with practical utility. These findings pave the way for broader adoption of LED-based photoacoustic imaging technologies in applications ranging from biomedical diagnostics to underwater acoustics. Future work could focus on improving signal-to-noise ratios, enhancing system isolation to reduce electromagnetic interference, and increasing refresh rates through optimized averaging techniques and transducer designs.

Author Contributions: A.P did all the experimental work, data acquisition, and analysis. F.N contributed expertise, direction, materials, and experimental tools.

Funding: The authors wish to thank the Natural Science and Engineering Research Council (NSERC) of Canada for its financial support of this work.

Acknowledgments: The author would like to thank CMC Microsystems for providing the layout design tools and enabling chip fabrication.

Conflicts of Interest: The authors declare no conflict of interest.

CHAPTER 3

HIGHLY INTEGRATED MEMS PASSIVE STRAIN SENSOR WITH A DIRECT CONTACT DETECTION MECHANISM

Alberto Prud'homme [a], Paul Okulov [b], and Frederic Nabki [a]

[a] Department of Electrical Engineering, École de Technologie Supérieure
1100 Notre-Dame West, Montréal, Quebec, Canada H3C 1K3

[b] IPR Innovative Products Resources, Inc.,
Sainte-Anne-de-Bellevue, QC, H9X 1B5, Canada.

Paper submitted after responding to the major revision to *IEEE JMEMS*, March 2026

Abstract:

A passive, ultra low power microelectromechanical systems (MEMS) strain sensor that converts micrometer-scale displacement into discrete resistance steps via engineered mechanical contacts is presented. Three topologies, cantilever, stacked beam, and concentric ring, were fabricated in the PiezoMUMPs process and interfaced to a microcontroller (MCU) for digital readout. The concentric-ring device, which employs doubly supported beams with circular pads, provided the best balance of robustness, electrical continuity, and resolution: it resolves uniform 2-μm increments over a 0-20 μm range with contact resistances <20 kΩ under full load. A custom characterization platform using a 50-nm-resolution motorized stage and precision resistance metrology validated the stepwise response and showed <±2 μm hysteresis across the operating range, except near the upper limit. Because transduction is passive, no bias current is required before the first closure. The full system (transducer and MCU) operates with an average power consumption of 2.8 μW at 1 Hz. This contact-based approach enables scalable, highly energy-efficient strain and displacement monitoring in applications such as wireless sensor nodes, structural health monitoring, and implants.

Keywords: MEMS strain sensor, passive sensing, direct contact, PiezoMUMPS, ultra-low power.

3.1 Introduction

Accurate strain quantification is important in safety and reliability in aeronautics, civil infrastructure, and biomedical systems (Javed, Mansoor, & Shah, 2019; Khoshnoud & Silva, 2012; Kon, Oldham, & Horowitz, 2007). At small scales, microelectromechanical systems (MEMS) enable embedded strain sensing with compact form factors, supporting applications that span pressure and deformation monitoring, displacement tracking in confined mechanisms, vibration and fatigue assessment, and networked wireless diagnostics (Liu et al., 2015; Song et al., 2020; Y. Zhang, Howver, Gogoi, & Yazdi, 2011). In these contexts, limited energy budgets and stringent robustness requirements drive the need for stain sensing approaches that minimize electronics overhead while maintaining precision.

Widely used MEMS strain-sensing modalities present well-known trade-offs. Piezoresistive devices are simple to integrate but demand continuous bias and exhibit thermal drift (Panas et al., 2012). Capacitive sensors offer high sensitivity yet rely on low-noise, parasitic-aware readout and careful packaging (Aebersold et al., 2006). Optical schemes provide electromagnetic immunity but incur alignment complexity, high power consumption and cost (Westerveld et al., 2014). Resonant techniques achieve excellent resolution but require active drive, frequency tracking, and related control circuits (Do et al., 2016; Wojciechowski et al., 2004). These factors complicate deployment in energy and space-constrained systems where long battery-life operation is important.

Direct-contact transduction is an attractive alternative explored in this work. Engineered micro-contacts close under displacement, producing discrete electrical states that map to strain or motion. Such contact-based sensing can be intrinsically passive, with essentially no current draw prior to the first closure, and it interfaces naturally to digital electronics. In turn, the design burden shifts to achieving robust contact geometry, continuity, and low/consistent contact resistance under small gaps and process tolerances (Okulov, 2017). Reliable stepwise behavior despite alignment errors and non-ideal conductive sidewalls is therefore critical for practical realization.

Accordingly, this work moves beyond the typical strain-transducer concept by co-designing a micro-contact array and an event-driven readout interface so that the sensing node can remain in a deep-sleep state and only dissipate energy upon contact closure, while producing inherently discrete (i.e., step-coded) electrical states that can be acquired without an always-on analog front-end. A highly integrated passive MEMS strain sensor that converts micrometer-scale displacement into discrete resistance transitions using micro-contact arrays is realized in the commercial PiezoMUMPs process and its state is read out using a 1.8 V microcontroller.

Three topologies were implemented to address the challenges of the direct-contact-based architecture: (i) cantilever-based, (ii) parallel doubly supported beams, and (iii) a concentric-ring variant, achieving a 2 μm step size over a 0-20 μm displacement range. At the system level, because the transducer is electrically inactive until contact closure, the interface electronics can be fully duty-cycled: the microcontroller can remain in deep-sleep and wake only on a contact event, while the step-coded output enables direct digital capture without an always-on analog front-end.

Relative to prior art, the approach emphasizes manufacturability and energy efficiency while directly addressing contact reliability. In the PiezoMUMPs stack, a 10 μm single-crystal silicon layer is surface-doped only to ~2-3 μm depth. Therefore, axial misalignment can bring insulating regions into contact, increasing resistance and risking missed displacement steps. The proposed geometries, particularly the concentric-ring, mitigate these effects by increasing effective contact area, controlling pressure distribution, and reducing torsional susceptibility, which collectively improve electrical continuity under displacement. The resulting step-coded output simplifies the readout chain to high-value pull-down resistors and direct digital capture. This eliminates the need for precision analog front-ends, and allows always-on microwatt-level operation, compatible with energy-harvesting or duty-cycled wireless nodes for applications such as structural health monitoring and implants.

Overall, the combination of passive micro-contact transduction with compact digital integration complements existing piezoresistive, capacitive, optical, and resonant solutions, and offers a scalable pathway to low-power, high-robustness strain and displacement monitoring across embedded applications.

This paper is organized as follows. Section II details device structures, electronics, and the characterization setup; Section III presents measurement results; Section IV discusses implications and situates performance relative to prior sensing modalities, and is followed by a conclusion.

3.2 System Integration

This work presents the design and implementation of a MEMS-based strain sensor capable of measuring structural deformation with displacements up to 20 µm. The architecture emphasizes energy efficiency, comprising three main components: the MEMS direct-contact transducer, the readout electronics, and the experimental characterization setup.

The first component, the MEMS direct-contact transducer, converts mechanical displacement induced by external loads (i.e., strain) into measurable electrical responses. Its geometry and contact design determine the sensitivity, resolution, and repeatability of the transduction mechanism, forming the core of the sensing system.

The second component is the electronic circuit, which interfaces directly with the transducer to detect and process the electrical signals generated during contact events. It converts variations in contact resistance into discrete digital outputs, enabling direct displacement quantization without the need for analog front-end amplification or complex conditioning stages.

Finally, the experimental setup provides precise mechanical actuation and electrical measurement for device characterization. Although external to the sensing module, it is essential for validating mechanical behavior, contact integrity, and readout performance under controlled displacement and loading conditions.

3.2.1 Transducer Fabrication and Design

The MEMS transducers were fabricated using the commercial PiezoMUMPs microfabrication process from Science Inc. A schematic cross-sectional view of the microstructure is shown in Figure 3.1. The process provides a 10 µm-thick single-crystal silicon device layer that is surface-doped to form a conductive region, as shown in Figure 3.1(a). An aluminum nitride (AlN) film, included in the process as a piezoelectric layer, is sandwiched between this doped silicon, acting as a bottom electrode, and a patterned metal top electrode. In the present work, however, this piezoelectric layer is not exploited for actuation or sensing. A silicon dioxide (SiO_2) layer is incorporated where needed to electrically isolate the silicon from the overlying metal stack.

The fabrication sequence begins with the deposition of a 200 nm-thick oxide layer on the silicon substrate, which is selectively etched to define vias for electrical contact with the silicon. The 0.5 µm-thick AlN film is then deposited and patterned to define the nominal piezoelectric regions. Subsequently, a metal stack comprising 20 nm of chromium and 1 µm of aluminum is deposited and patterned to form the top electrodes, wire-bonding pads, and routed interconnects above the oxide layer where appropriate (Inc, 2014).

Deep reactive ion etching (DRIE) is first used to pattern the silicon structures and then to remove the silicon substrate beneath the defined features, releasing suspended structures anchored only at designated points. This released configuration provides the desired mechanical compliance, determined primarily by the geometry and anchoring of each microstructure, while the chromium-aluminum metallization at the pads and interconnects ensures stable electrical connections to the external circuitry.

Figure 3.1(b) illustrates the layered composition of the active region of the proposed transducer. The suspended structure is designed to establish controlled contact with an opposing movable element under external mechanical loading. The sensing function resides in the doped silicon layer, which is patterned into geometries that selectively engage when displacement occurs. As specific regions of the doped silicon come into contact, discrete changes in electrical resistance are produced, providing measurable indicators of strain or displacement. The surface doping ensures sufficient conductivity to accurately resolve these resistance transitions.

Accordingly, each transducer consists of a movable silicon element and a stationary silicon structure, the latter connected to external circuitry through wire-bonded pads anchored to the substrate to capture the resistance changes generated by the structural contacts.

Adherence to process design rules is required to ensure reliable fabrication. In particular, the PiezoMUMPs process specifies a minimum gap of 2 μm between adjacent silicon features. This constraint directly limits the smallest achievable separation between contact elements and therefore bounds the resolution of the contact-based sensing mechanism, as discussed subsequently.

A defining characteristic of the PiezoMUMPs process is the shallow doping depth, typically extending only ~2–3 μm into the 10 μm-thick silicon layer. Although adequate for lateral conductivity, this limited profile complicates reliable axial contacts between silicon elements. Any vertical misalignment due to deformation can shift contact points beyond the doped region, increasing contact resistance and degrading signal integrity and long-term reliability.

Because electrical conduction occurs primarily within this thin doped layer, precise vertical alignment and sufficient contact pressure are critical design considerations for robust contact-based MEMS transducers, representing a primary challenge addressed by this work (Uttamchandani, 1995).

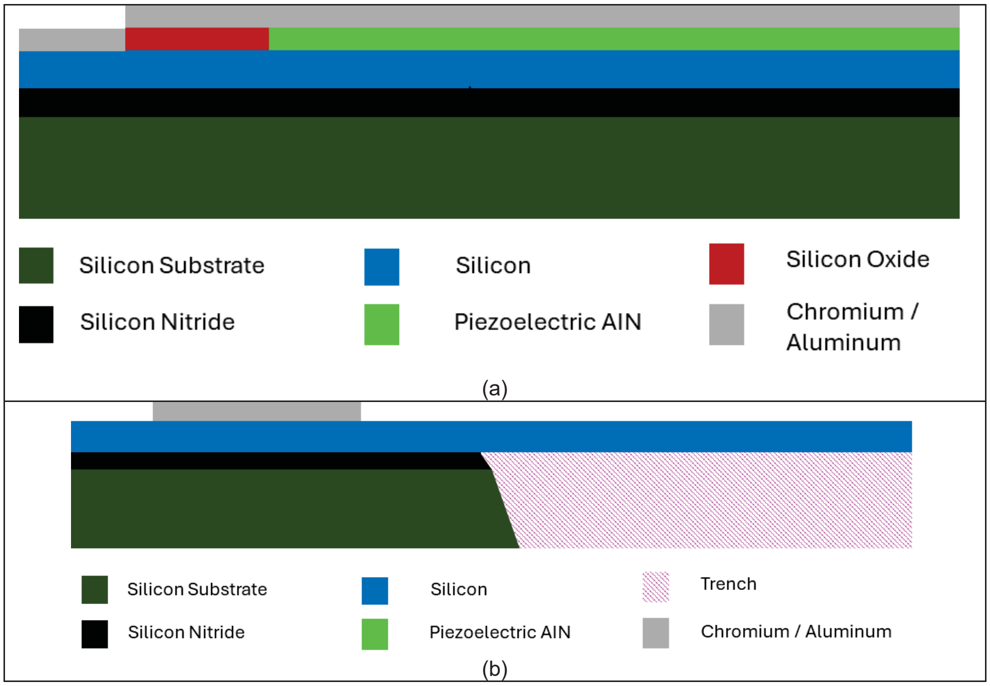

Figure 3.1 (a) PiezoMUMPS available fabrication layers,
(b) PiezoMUMPS layers used in the micro-strain micro-structure

Three MEMS device variants, denoted as Device A, Device B, and Device C, were designed and fabricated in this work. Although their mechanical configurations and electrical readout methods differ, all three share the same fundamental contact-based operating principle described previously.

Device A, depicted in Figure 3.2(a), consists of a suspended structure supported by four flexural arms, each measuring 225 µm in length and 2.5 µm in width. These support arms provide mechanical compliance, enabling controlled out-of-plane displacement. A central circular opening (60 µm in diameter) in the suspended mass accommodates a stainless-steel microneedle, which precisely actuates displacement during experimental characterization.

The stationary structure, anchored to the substrate, integrates ten cantilever beams per side, each 90 µm in length and inclined at a 15° angle relative to their anchors. These cantilevers act as fixed electrical contacts connected to the external readout circuitry via wire-bonded pads. Corresponding movable cantilever arms extend from the suspended mass, angled similarly to ensure proper alignment. The contact pairs formed between movable and stationary cantilevers are spaced in incremental 2 µm steps. Thus, an initial displacement of 2 µm engages one cantilever pair per side (the uppermost pair shown in Figure 3.2(a)), a displacement of 4 µm engages two pairs per side, and so forth until full engagement of all contact pairs at a 20 µm displacement.

The angled arrangement of cantilever beams progressively increases contact pressure as displacement advances, thereby enhancing electrical conduction and reducing contact resistance between structures.

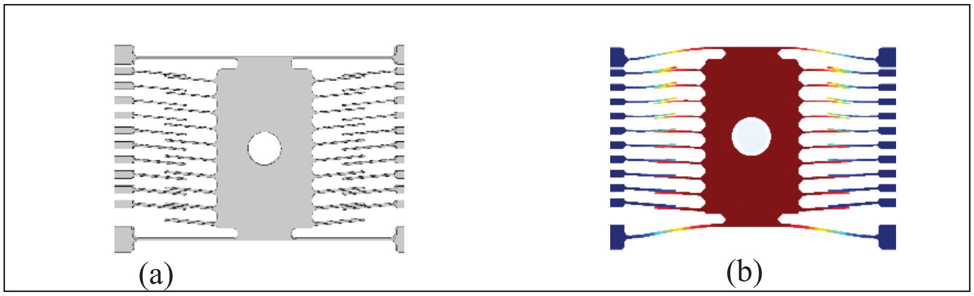
(a) (b)

Figure 3.2 Device A, (a) Layout of the suspended body and surrounding fixed cantilevers, (b) FEM simulation of the strain generated by a 20 µm displacement

Figure 3.2(b) shows a finite element method (FEM) simulation conducted using COMSOL, illustrating deformation of the four suspension arms under a 20 µm displacement. The simulation reveals the pressure distribution across the contact arms, indicating that upper contacts experience higher strain due to their earlier engagement, while lower contacts encounter less strain, engaging at larger displacements.

Figure 3.3(a) provides a scanning electron microscope (SEM) micrographs of fabricated Device A. On each side, 125 µm × 125 µm contact pads and associated connections are visible, along with the underlying trench that allows structural suspension Figure 3.3(b) shows a closer view of the cantilever contacts inclined at 15°, opposite to the displacement direction. This angular orientation was chosen to prevent torsional displacement of the suspended structure, ensuring symmetrical contact engagement on both sides. Although pairs of cantilevers are positioned identically, only one cantilever per pair connects electrically to the pads.

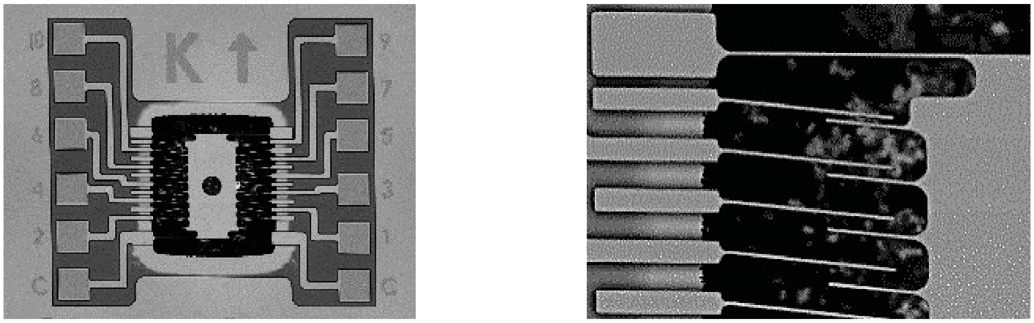

(a)

(b)

Figure 3.3 Device A, (a) SEM micrograph of the transducer,
(b) close-up to the contacting arms

Device B, shown in Figure 3.4, implements an alternative mechanical topology, employing parallel doubly supported beams instead of cantilevers. This configuration significantly enhances structural stability and minimizes torsional sensitivity, which can otherwise compromise contact alignment in flexible designs. As displacement increases, the resulting rise in contact pressure, together with frictional forces at the interfaces, improves electrical engagement and further stabilizes the contact configuration.

Figure 3.4(a) presents the layout of Device B, highlighting its parallel doubly supported beams and a central displacement mass. Each contact pair consists of two beams, each measuring 630 μm in length and 2.5 μm in thickness. A central mass, measuring 80 μm × 10 μm, serves as the contact interface and provides mechanical isolation to ensure adequate spacing between contacts. As in Device A, the central mass incorporates a 60 μm aperture to accommodate a microneedle used for controlled displacement. The double-support configuration significantly reduces torsional misalignment during mechanical loading. Contacts are again spaced at uniform 2 μm intervals.

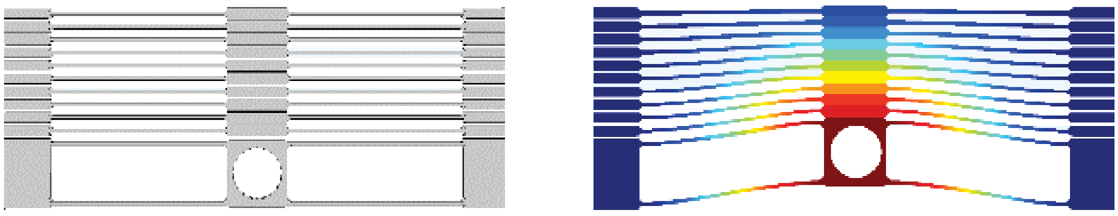

(a) (b)

Figure 3.4 Device B (a) layout design showing the parallel doubly-supported beams and central displacement mass, and (b) FEM simulation illustrating the pressure distribution and beam deformation resulting from a 20 µm vertical displacement applied at the center.

Figure 3.4(b) shows FEM simulation results for Device B under a central vertical displacement of 20 µm. The simulated pressure distribution confirms that the earliest contacts experience the highest loading, with subsequent contacts engaging at progressively lower pressures, consistent with the intended incremental deformation mechanism. To ensure robust electrical continuity between sequential contacts despite potential misalignment or dopant variability, the doped contact regions were maximized and the central contact blocks were extended to increase overlap while preserving structural flexibility.

Figure 3.5 presents SEM and optical microscope views of fabricated Device B. Figure 3.5(a) shows the overall device architecture, including the suspended beams and contact regions. Each side incorporates five electrical contact pads corresponding to interconnected contacts, with additional pads allocated for the movable central mass used during characterization. Figure 3.5(b) provides a magnified SEM view of the central mass region, highlighting the contact pairs that activate at 2 µm and 4 µm displacement increments, as well as the filleted geometries designed to permit controlled flexure while minimizing stress-induced fracture.

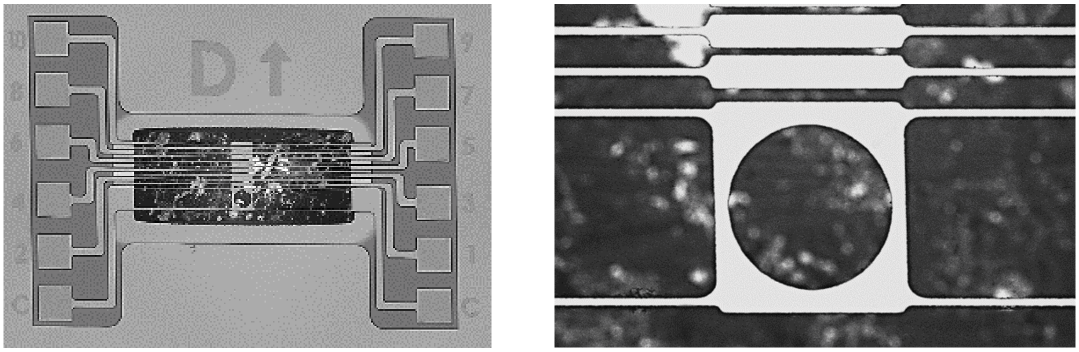

(a) (b)

Figure 3.5 Device B: (a) SEM image showing the overall architecture of the device, including the suspended beams and contact regions; (b) close-up SEM image highlighting the geometry and alignment of the contact interfaces.

The final design, Device C, refines the parallel-beam concept by integrating concentric semicircular contact interfaces, which enhance the effective contact area and optimize pressure distribution

Figure 3.6(a) illustrates the layout of Device C. The movable structure is ring-shaped, with a central 60 μm diameter aperture for microneedle insertion. The ring thickness is 5 μm, and the doubly supported beams are 2.5 μm thick and 650 μm long.

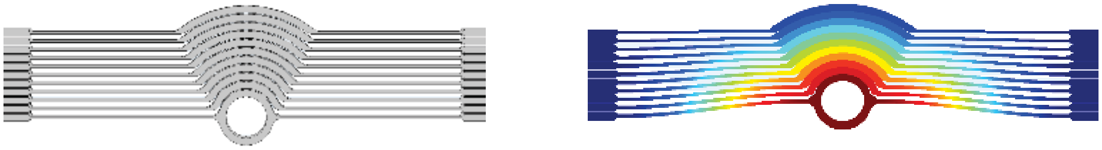

(a) (b)

Figure 3.6 Device C: (a) layout design featuring a ring-shaped movable mass with semicircular contact arms; (b) FEM simulation illustrating the pressure distribution and beam deflection under a 20 μm displacement.

Contact arms, again spaced at uniform 2 µm intervals, incorporate semicircular contact segments at their midpoint. Successive semicircular contacts increase in size by 2 µm, with each diameter further scaled by 5% relative to the previous one. This incremental sizing reduces stiction and enables progressive, reversible engagement.

To maintain a consistent overall beam length while accommodating progressively larger contact areas, the supporting arms are correspondingly shortened. This adjustment compensates for center-of-mass shifts and reduces susceptibility to torque-induced misalignment. Consequently, later-stage beams undergo substantially smaller displacements than the initial beams: whereas the first contact beam accommodates the full 20 µm displacement, the final beams experience less than 1 µm. The increased stiffness of these shorter beams produces higher contact pressures for a given deflection, reducing contact resistance and enhancing detection sensitivity at the moment of contact.

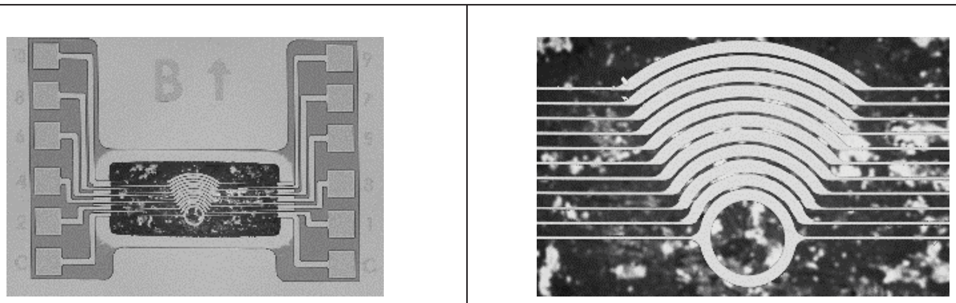

(a) (b)

Figure 3.7 Device C: (a) SEM image showing the complete microstructure with ring-shaped movable mass and contact beams; (b) close-up SEM view of the semicircular contact features and spacing.

Figure 3.6(b) presents FEM simulation results showing the pressure distribution across the concentric contact regions during a 20 µm displacement. The optimized distribution promotes precise alignment of doped contact surfaces and mitigates risks of misalignment, overlap, or mechanical fracture under load.

Figure 3.7 shows SEM and optical microscope images of fabricated Device C, with five concentric contacts per side, uniformly spaced at 2 μm intervals. Contact pad connections alternate between device sides, facilitating interconnect routing while preserving mechanical symmetry.

Figure 3.7(a) and (b) provide SEM views of the overall microstructure and detailed contact geometry, respectively. The central mass is designed to withstand mechanical loading without deformation, thereby avoiding inadvertent stiction or unreliable electrical contacts.

3.3 Readout Electronics

An electronic readout system was developed to interpret mechanical responses and translate them into measurable displacement values. Figure 3.8(a) shows the schematic of this readout circuit, which is based on an STM32L0-series microcontroller (MCU) selected for its ultra-low-power characteristics, suitable for energy-sensitive applications.

The transducer movable mass is electrically connected to a 1.8 V reference voltage line (VDO), while each stationary contact connects to an individual general-purpose input/output (GPIO) pin on the MCU. To prevent false activations from floating inputs, each GPIO line is tied to ground through a high-value (100 MΩ) pull-down resistor. Figure 3.8(b) details the resulting voltage-divider network associated with the ten discrete contact pads.

Operation begins when the movable mass undergoes an initial displacement of approximately 2 μm, establishing electrical contact with the first stationary contact through the doped silicon layer and equalizing their potentials. Each additional 2 μm increment in displacement sequentially engages further stationary contacts until all ten are activated at a total displacement of 20 μm. This stepped contact sequence produces discrete, identifiable voltage states that directly encode displacement.

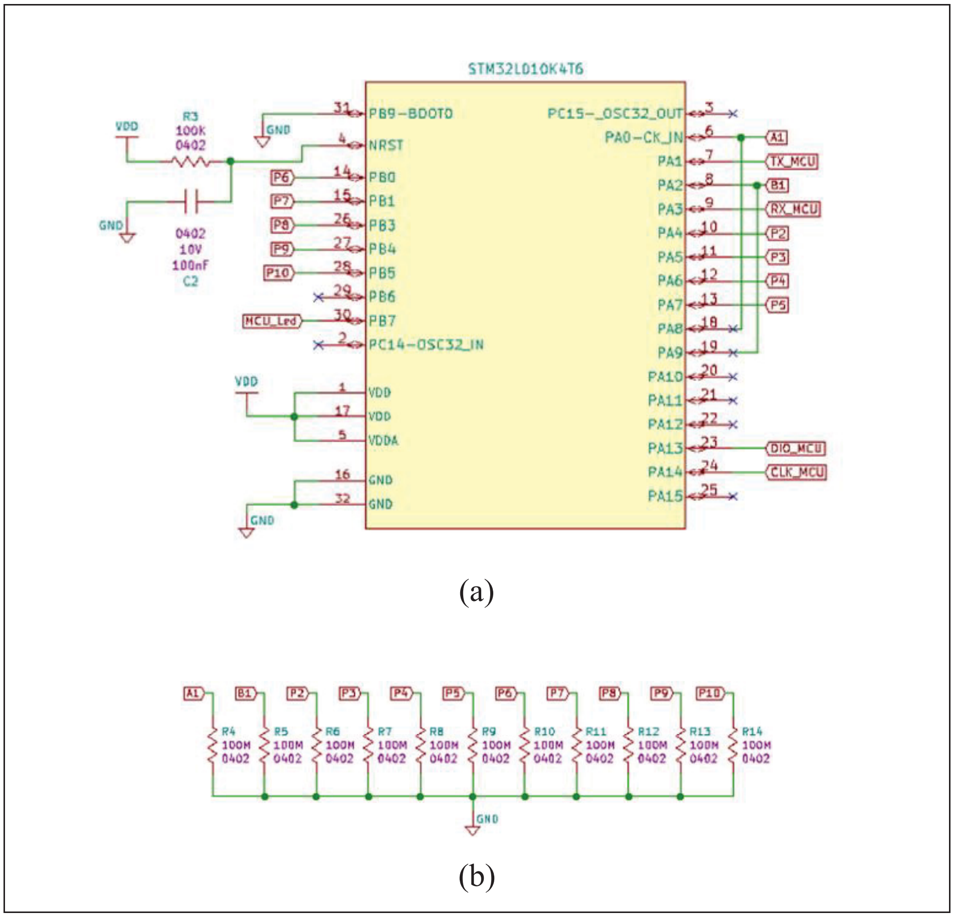

(a)

(b)

Figure 3.8 Sensor readout electronics: (a) circuit schematic of the complete sensor system; (b) schematic of the high-resistance voltage divider network.

The use of high-value pull-down resistors ensures that even brief mechanical contacts generate voltages exceeding the MCU’s digital detection threshold. This strategy enables sensitive detection without requiring large contact forces, achieving accurate displacement measurements with extremely low current consumption. Communication with external systems is handled via the MCU’s universal asynchronous receiver–transmitter (UART) interface, and a micro-LED is included to aid debugging and initial verification.

The final integrated readout printed circuit board (PCB) is shown in Figure 3.10. It employs a 28-pin quad flat no-lead (QFN) socket, enabling rapid evaluation and interchangeability among different transducer designs by simply exchanging the QFN-packaged device.

For compatibility with mechanical characterization equipment, the PCB dimensions were chosen larger than strictly necessary, and all electronic components were placed on a single side of the board to avoid potential short circuits or issues with mechanical fixtures. Although miniaturization was not a primary objective, a preliminary layout study indicates that substantial size reduction is feasible. By removing the QFN socket and distributing components on both PCB sides, the system footprint could be reduced to approximately 12 mm × 12 mm, with further reductions possible through smaller component packages and optimized board layouts for space-constrained applications.

3.3.1 Characterization Setup

In this work, the sensing mechanism is characterized using externally imposed displacement via the controlled microneedle positioned through the central circular opening in order to validate the passive contact-based transduction and discrete step outputs. In a complete strain-sensing implementation, a packaging/mechanical integration approach is required to couple host-structure strain into the suspended mass of the MEMS transducer as a predictable in-plane relative displacement

Figure 3.9 illustrates the experimental setup, which provides three distinct functions. First, it ensures precise displacement control using a Thorlabs KMTS25E motorized stage with a maximum travel of 25 mm and incremental resolution of 50 nm. This high-resolution stage allows for precise positioning of the transducer, allowing up to 40 incremental steps within each 2 µm displacement interval to characterize the transducers' electrical contacts.

Second, the setup measures electrical resistance across contacts at different displacement stages using a Keithley DMM6500 digital multimeter. Resistance data give reveals the evolution of contact quality under increasing mechanical load, reflecting torsion effects, stress distributions, and potential alignment issues.

Thirdly, the setup allows for evaluation of the integrated sensor performance, combining the MEMS transducer with the electronic readout circuit.

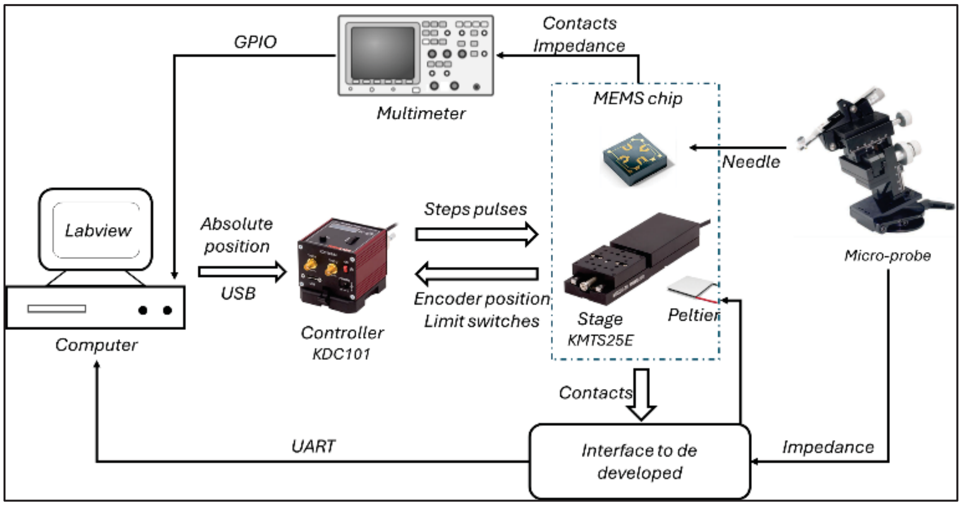

Figure 3.9 Diagram of the characterization setup

System control and data acquisition are implemented using a LabVIEW-based interface, with real-time control and response visualization. Figure 3.10 presents a photograph of the characterization setup. Accurate preparation prior to testing is aided by a Cyclops 4K Ultra HD digital microscope, offering magnifications up to 140X. This magnification enables precise alignment and detailed visual inspection of the transducer's features. Electrical resistance measurements were performed at room temperature (~21°C) under ambient laboratory conditions, without active control of humidity or atmospheric pressure.

Figure 3.11 shows a close-up view of the experimental arrangement, illustrating precise positioning of the stainless-steel microneedle within the 60 µm aperture of the MEMS microstructure under test. Accurate microneedle placement is achieved using a Thorlabs PT3A/M three-axis manual translation stage, offering 25 mm travel per axis and 250 nm positional resolution. Initially, the microneedle is positioned safely away from the transducer. The motorized stage actuator is then reset to the zero-displacement position. Subsequently, the manual stage carefully aligns the needle within the device aperture. Once properly positioned, the actuator advances until initial minimal electrical contact is detected, defining the reference point for displacement measurements.

Following this initial alignment, automated characterization begins. The motorized actuator incrementally advances the microstructure against the needle in nanometer-scale steps. At each increment, either contact resistance or voltage-divider output is measured, depending on experimental requirements.

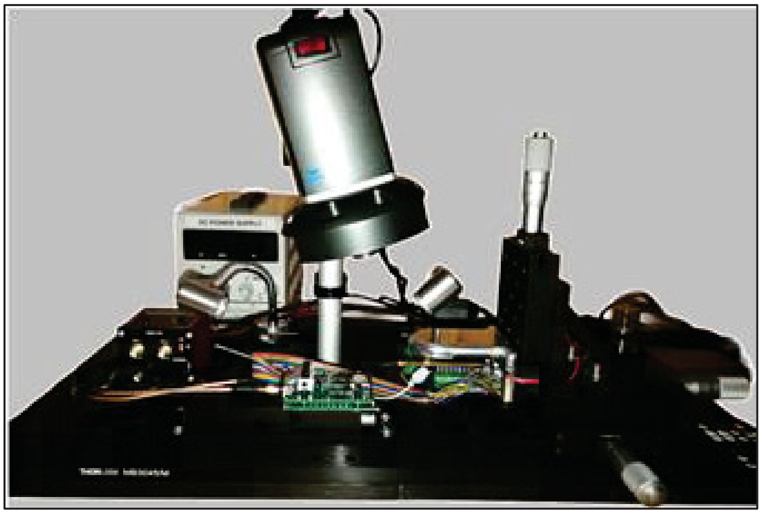

Figure 3.10 Photograph of the characterization setup

Upon achieving the target displacement of 20 µm, the measurement process transitions into a retraction phase. Initially, the actuator withdraws by 4.5 µm, a displacement chosen specifically to compensate for mechanical backlash without causing actual reverse movement of the structure. Subsequently, the actuator again incrementally advances through the 20 µm range, taking measurements at consistent intervals. This forward-reverse sequence continues until contact between the microneedle and microstructure becomes negligible, typically with positional variations within ±1 µm attributable to mechanical backlash. Completion of this forward-reverse cycle constitutes a full characterization sequence for each tested device configuration.

3.4 Measurement Results

Each fabricated MEMS transducer was subjected to two complementary experimental tests to characterize mechanical and electrical performance. First, resistance measurements between device contacts were recorded over a displacement range of 20 µm, at increments of 500 nm. These measurements enabled detailed analysis of contact quality, electrical continuity, and stability under progressively increasing mechanical loads.

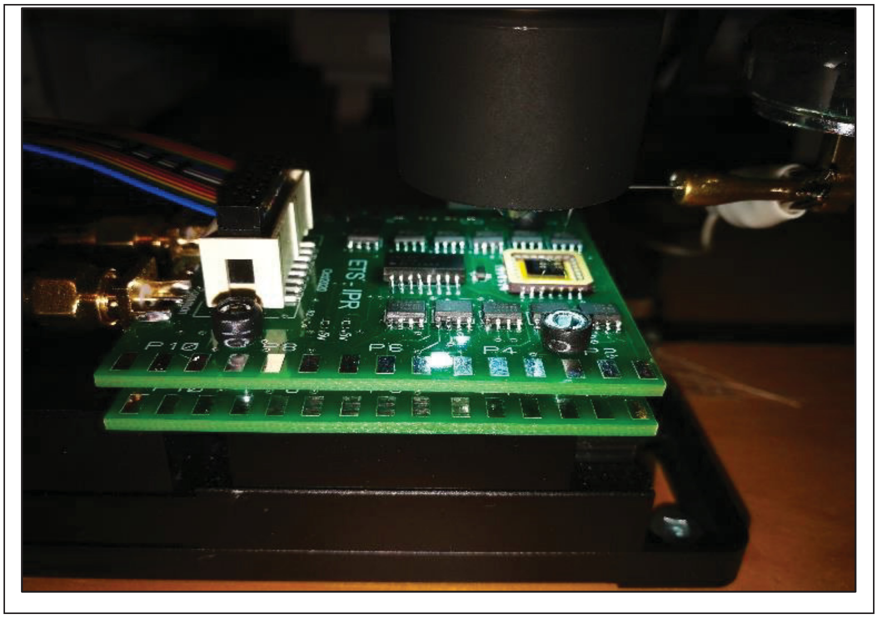

Figure 3.11 Close-up of the micro-needle and PCB on the motorized stage

Second, integrated system performance was evaluated using the readout electronics described previously. This assessment involved monitoring transducer response throughout a complete forward and backward displacement cycle.

3.4.1 Device A characterization

Figure 3.12(a) illustrates the first contact measured resistance variation of Device A as a function of displacement. At an initial displacement of approximately 2 µm, a low-pressure contact occurs, resulting in a resistance reading near 50 MΩ. Prior to this displacement, the measured resistance remains effectively infinite, indicating no physical electrical contact.

From 2 μm to approximately 10.5 μm displacement, resistance values remain relatively stable between 50 MΩ and 60 MΩ, reflecting limited mechanical contact. Beyond 10.5 μm displacement, the resistance decreases sharply to approximately 50 kΩ, signifying increased mechanical engagement, enhanced contact pressure, and larger effective conductive areas.

Figure 3.12(b) provides a zoomed-in view of the resistance fluctuations occurring between 14 μm and 16 μm displacement. Within this region, pronounced resistance variations occur, indicative of transitional mechanical contact and evolving conduction paths. Beyond approximately 16 μm displacement, resistance stabilizes near 30 kΩ, suggesting consistent mechanical contact engagement and saturation.

Resistance variations across the displacement range primarily result from Device A's cantilever-based contact configuration. Cantilevers supported at only one end experience substantial flexural deformation upon mechanical engagement. As displacement increases, the effective contact area changes dynamically due to combined bending deformation, torsional rotation of beams, and surface roughness interactions at the contact interfaces.

An important factor influencing the measured resistance is torsional deformation. Increased mechanical load during displacement induces beam torsion, reducing the effective contact area and elevating resistance. The interplay among torsion, flexural bending, and surface roughness thus explains the dynamic resistance variations observed experimentally.

Figure 3.12 compares the nominal displacement imposed by the microneedle positioning system (forward and reverse cycles) with the displacement inferred from the integrated transducer electronics output states, providing a direct assessment of measurement accuracy and hysteresis under cyclic loading. The x-axis labeled "Measurement Samples" represents the sequence index of repeated measurements acquired during successive displacement cycles (i.e., acquisition order). Device A exhibits notable limitations in resolving the full 0-20 µm range due to the mechanical and electrical limitations discussed previously, which affect contact consistency and electrical continuity. Within the portion of the sweep where stable step transitions are observed, deviations of up to approximately 4 µm occur between the imposed displacement and the displacement inferred from the detected contact transitions.

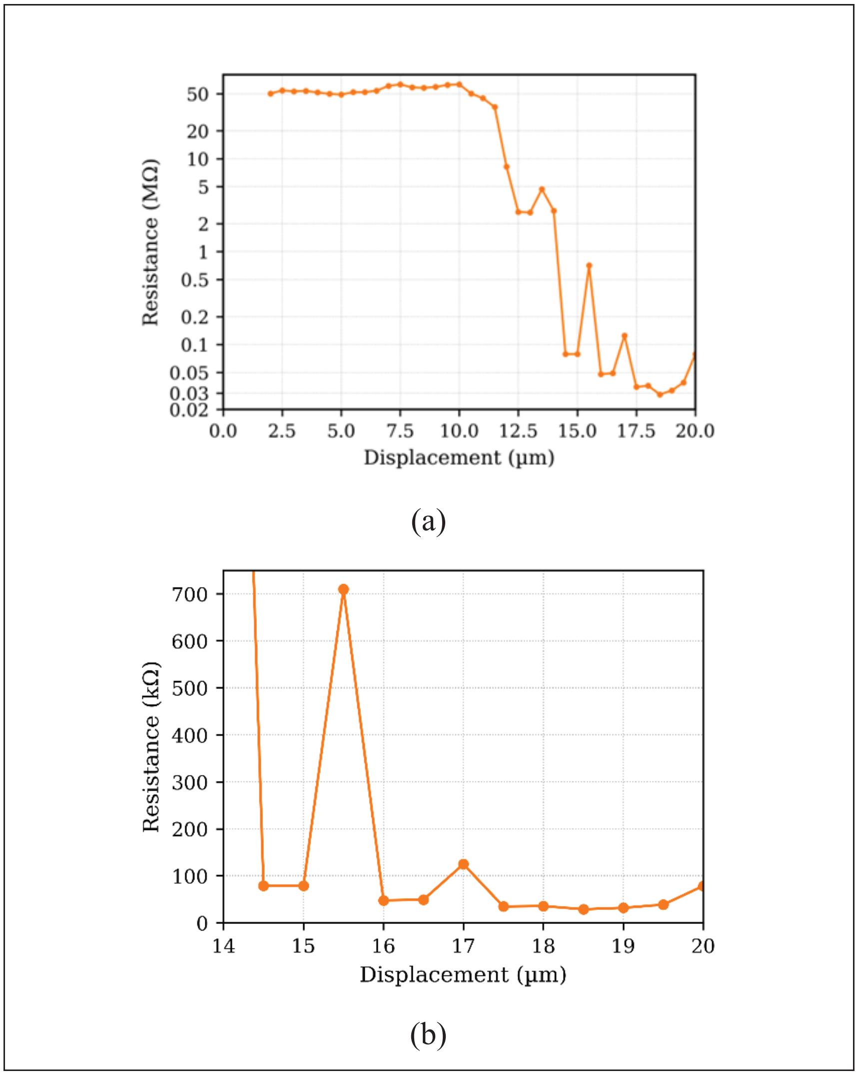

(a)

(b)

Figure 3.12 Device A motion resistance characterization: (a) Measured resistance variation across the full 20 µm displacement range; (b) Close-up of the resistance transition region (14-16 µm displacement).

Additionally, significant hysteresis is observed during reverse displacement: the inferred displacement drops sharply beyond approximately 10 µm and recovers only partially near approximately 4 µm.

Figure 3.13 compares actual imposed displacements (forward and backward cycles) with those measured by the integrated transducer-electronics sensor. This assesses measurement accuracy and responsiveness under cyclic loading. As can be seen, Device A exhibits notable limitations in accurately resolving the full 20 µm displacement range, with measurement discrepancies up to ~4 µm. Additionally, significant hysteresis occurs during reverse displacement such that measured displacement drops sharply beyond 10 µm and recovers only partially near approximately 4 µm.

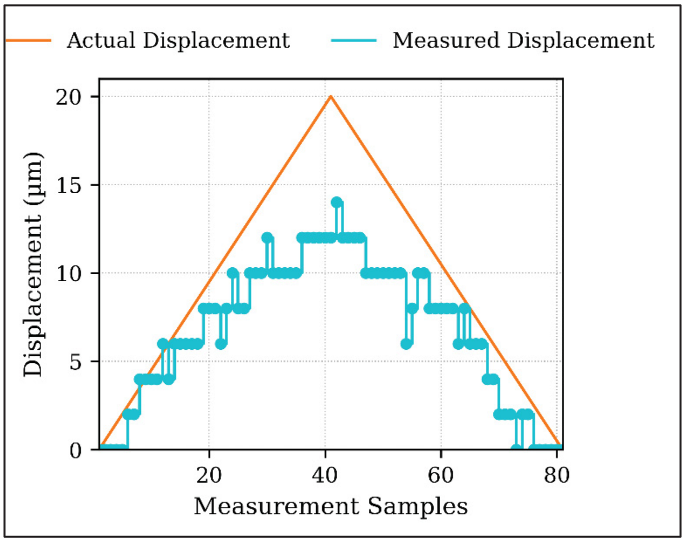

Figure 3.13 Device A comparison of actual displacement with sensed output

Erratic responses observed during forward displacement are attributable to intermittent electrical contact. Measurement inaccuracies during reverse cycles likely result from mechanical obstruction caused by unintended overlap of contacts. Specifically, torsional deformation of the cantilever beams under mechanical loading causes vertical misalignment along the Z-axis, which can lead to lateral sliding or crossing of contacts. Such unintended overlaps temporarily lock contacts during reverse displacement, significantly reducing measurement accuracy until the beams return to proper alignment. These phenomena also impose additional mechanical stresses at the beam anchors, potentially reducing structural reliability over extended usage.

3.4.2 Device B characterization

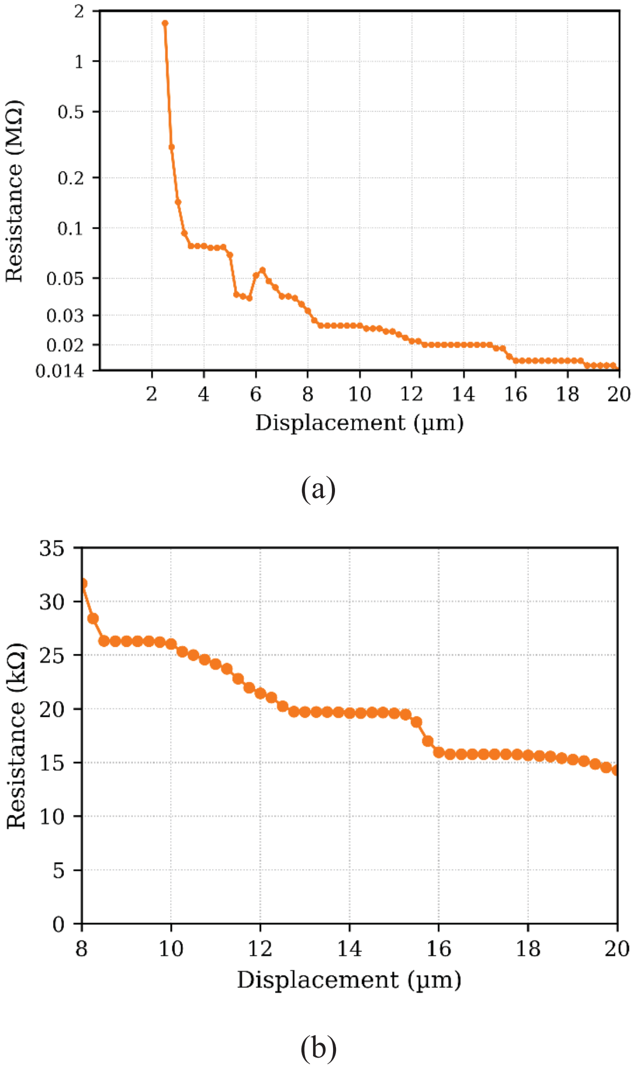

Figure 3.14 Device B resistance characterization:
(a) Measured resistance variation across the full 20 μm displacement range; (b) Close-up of the resistance transition region (8-20 μm displacement).

Figure 3.14(a) presents the first contact measured resistance results for Device B, whose mechanical design (described previously in Figure 3.4) addresses limitations identified in Device A. Device B exhibits a clearer initial resistance transition, decreasing from effectively infinite to approximately 1.7 MΩ at about 2.5 µm displacement, significantly improving initial contact detection. However, a slight offset (~500 nm) between initial physical contact and measurable resistance change indicates a minor response offset.

At approximately 3 µm displacement, stable mechanical coupling is established, reflected by resistance values decreasing below 100 kΩ. Beyond this point, resistance decreases steadily and linearly with further displacement, consistent with progressively increasing contact pressure, demonstrating more reliable contact characteristics than device A Figure 3.14(b) shows a close-up on the first contact resistance behavior from 8 µm to 20 µm displacement. Over this range, resistance decreases linearly by approximately 15 kΩ, confirming Device B's consistent and predictable response under incremental loading.

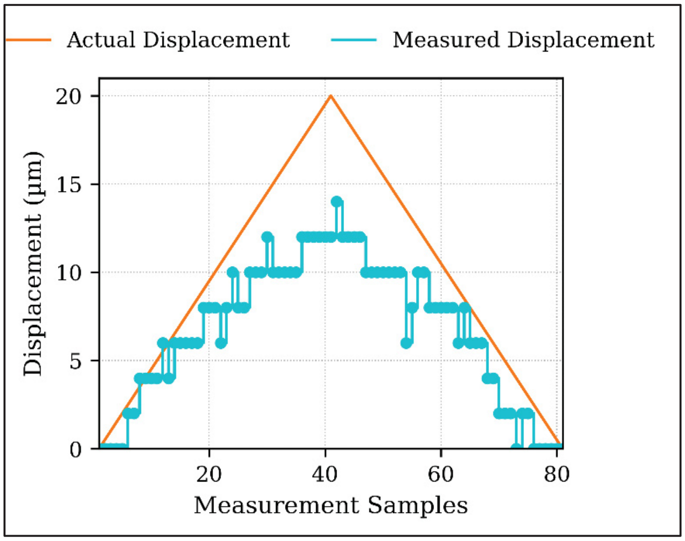

Figure 3.15 Device B Comparison of actual displacement with sensed output.

Figure 3.15 compares actual imposed displacement values with measurements from the integrated transducer-electronics sensor. These results indicate substantial improvement over Device A, particularly within the initial 0-8 µm displacement range, where measured displacement closely tracks actual values. However, above approximately 10 µm, measurement accuracy declines significantly. The maximum displacement detected by the transducer reaches about 14 µm instead of the actual 20 µm imposed displacement. This loss of accuracy at higher displacement values suggests the need for further optimization to fully utilize Device B's improved structural configuration at larger displacement. Nonetheless, measurements taken during the return (reverse) displacement phase highlight Device B's improved capability to accurately track displacement, with only minor discrepancies primarily caused by pressure variations and associated hysteresis. Overall, these results confirm Device B's enhanced displacement tracking over most of its operating range relative to Device A.

3.4.3 Device C characterization

Figure 3.16(a) presents the first contact measured resistance for Device C across a displacement range from 0 to 20 µm. At the initial contact displacement of approximately 2 µm, resistance is near 4 MΩ. Beyond this point, resistance rapidly decreases, reducing its variation at around 4 µm displacement.

This sharp resistance drop results from effective mechanical engagement and increasing contact pressure. With continued displacement beyond this threshold, resistance further decreases slightly and stabilizes, indicating robust and well-established contact conditions.

The initial resistance characteristics of Device C closely match those of Device B, attributable to their similar doubly supported beam configurations. This reinforced structural design significantly enhances mechanical rigidity, stabilizing contact surfaces and minimizing torsion or asymmetrical deformation during displacement. Enhanced mechanical stability reduces lateral and vertical misalignment, effectively preventing contact overlap, a potential source of operational failure. Consequently, Device C exhibits predictable and stable electrical resistance across its operating displacement range.

Figure 3.16(b) highlights the contact stability region in greater detail, illustrating resistance decreasing progressively from approximately 100 kΩ to 18 kΩ. This relatively low and stable resistance confirms robust contact integrity. After approximately 4 µm displacement, Device C maintains stable electrical contact with minimal relative resistance variation, confirming reliable mechanical engagement.

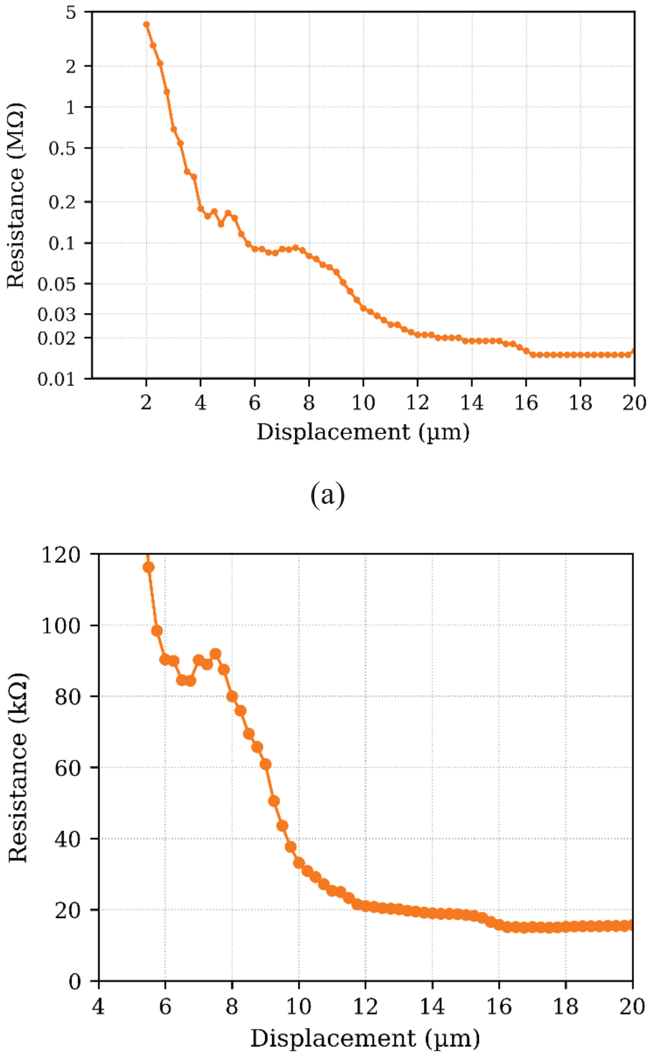

(a)

(b)

Figure 3.16 Device C - (a) Resistance during the 20µm displacement, (b) Close-up to the lowest resistance measured

Figure 3.17 compares actual imposed displacement values to measurements from the integrated sensor system for Device C. Results demonstrate significantly improved accuracy relative to Devices A and B (i.e., typically within ±2 µm across most of the range). However, measurement inaccuracies appear at higher displacements between 18 and 20 µm, likely due to mechanical instability or incomplete final contact engagement. These inaccuracies may result from deformation effects or insufficient surface coupling at maximum displacement.

During the reverse displacement phase, Device C generally exhibits satisfactory performance, though notable anomalies occur while reversing between 16 µm and 12 µm. Within this reverse motion range, abrupt measured displacement shifts are observed, indicating delayed release of the circular contact interfaces as mechanical pressure reduces. After overcoming this transient phenomenon, displacement measurements stabilize, returning consistently to the initial position.

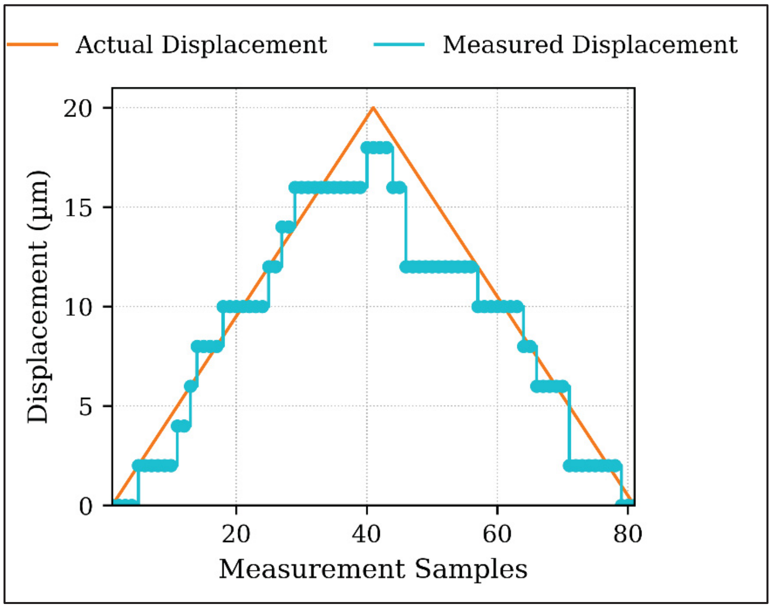

Figure 3.17 Device B - Real displacement compared with the Measured Displacement of the MEMS

Overall, Device C substantially outperforms Devices A and B due to two key design factors. First, the doubly supported beams significantly enhance structural rigidity, reducing susceptibility to torsion and unwanted deformation. Second, enlarged semicircular contacts significantly increase effective contact area, providing more stable mechanical engagement.

3.5 Discussion

Experimental results confirm that the MEMS microstructures successfully operate as strain transducers, achieving displacement measurements up to 20 μm with 2 μm resolution. Such resolution suits applications requiring precise detection of small structural deformations.

The hysteresis and resistance-state variability observed in Devices A and B are primarily attributed to torsional deformation of the suspended structures, which tilts the contact areas and produces non-uniform engagement across the contact interface. During loading, contact is expected to initiate locally and progressively expand as displacement increases. During unloading, elastic recovery leads to a different spatial release sequence. This difference in engagement/release sequence yields a different contact-overlap history for the same nominal displacement and therefore produces hysteresis in the decoded step state. In addition, when doped area overlap is partial, small variations in tilt and alignment can cause cycle-to-cycle variability in the effective conductive overlap, increasing the likelihood of unstable or missing resistance steps. These observations indicate that torsional compliance and contact geometry are the dominant contributors to hysteresis in the proposed structures and motivate torsion-stiff, symmetric suspensions and contact layouts that minimize contact area tilt and partial doping area overlap.

Device C consistently outperformed Devices A and B due to distinct mechanical advantages. However, all three devices exhibited certain measurement inaccuracies related primarily to intermittent electrical continuity during mechanical engagement. This issue is attributed to the shallow doping depth (~2~3 μm) in the 10 μm-thick silicon layer, which renders the devices highly sensitive to vertical misalignment during operation. Z-axis misalignments can shift mechanical contact regions to undoped, nonconductive silicon, causing elevated resistance and inconsistent signal detection.

Doped silicon surfaces exposed to air naturally form a thin native oxide layer at room temperature (Morita, Ohmi, Hasegawa, Kawakami, & Suma, 1989). In silicon MEMS contacts, the effective contact resistance is commonly modeled as a tunneling component in series with constriction resistance through microscopic conduction spots, with local disruption of the oxide film under mechanical loading (Kogut & Komvopoulos, 2003). As a result, the native oxide contributes to the measured contact resistance and can introduce variability during repeated contact cycles. In addition, any tangential micro-sliding at the contact interface during engagement may locally disrupt the native oxide and thereby reduce the effective contact resistance. Nevertheless, the dominant topology-dependent trends observed in this work remain primarily governed by contact geometry and mechanical deformation.

The shallow doping depth (i.e., ~2-3 µm) in the 10 µm-thick silicon layer makes electrical conduction highly dependent on whether the effective contact occurs within the near-surface doped region. Consequently, small vertical misalignments, torsional deformation, or fabrication-induced variations in sidewall profile can shift the contact location into undoped silicon, producing elevated resistance, intermittent continuity, or missed displacement steps. This sensitivity can reduce fabrication yield in practice, since mechanical contact does not necessarily guarantee a robust conductive path unless sufficient doped-overlap margin is maintained. From a reliability standpoint, the discrete resistance steps can become more sensitive to cycling-induced variations in contact overlap and contact location, reducing long-term repeatability. These limitations are primarily related to the fabrication process rather than the sensing principle itself.

These considerations motivate practical design rules for PiezoMUMPs-based direct-contact sensors: (i) maintain conservative overlap margins between opposing doped regions to tolerate expected misalignment; (ii) favor torsion-stiff, symmetric suspensions to minimize Z-axis skew during engagement; (iii) increase effective contact area and distribute contact pressure to stabilize conduction; and (iv) select contact pitch consistent with the 2 µm minimum-gap rule, which bounds the achievable quantization step size.

Additionally, some observed variability is attributed to the influence of fabrication tolerances. Slight deviations in dimensional precision or doping uniformity can directly impact device electrical behavior to displacement.

Moreover, fabrication-induced variations in mechanical properties, such as stiffness and sidewall roughness can have an impact. These variations may result in increased structural wear, unwanted vibrations, and inefficient mechanical coupling, collectively reducing device reliability. Similarly, doping concentration inconsistencies and deposition non-uniformities may introduce variability.

A distinguishing feature of the proposed transducer is its passive, direct-contact, event-driven detection mechanism, which enables negligible standby power consumption and inherently digital output states. Because the device remains electrically open until contact closure occurs, it does not require continuous electrical biasing or continuous monitoring of an analog or mechanical variable. When direct physical contact is established between microstructures, mechanically induced changes in resistance produce discrete, step-coded resistive states that can be captured directly by low-power digital circuitry. This operating principle simplifies the front-end electronics, reduces sensitivity to analog noise, drift, and calibration, and provides a robust, ultra-low-power alternative to conventional capacitive, piezoresistive, or frequency-based readouts. In this respect, the proposed approach differs from standard MEMS strain transducers, such as piezoelectric sensors that generate analog voltages under deformation and resonant sensors that rely on continuous frequency tracking. The demonstrated measurement range and resolution are currently determined by the contact geometry, but they can be further scaled in future designs by increasing the number of contacts and reducing the contact pitch.

Table 3.1 situates the proposed passive, contact-based sensor within the broader landscape of MEMS force, strain, and displacement transducers. Existing solutions span optical, piezoresistive, capacitive, and resistive principles and generally optimize either large measurable range or sub-nanometer resolution. Optical MEMS implementations, for example, achieve displacements on the order of 1.8 mm with 10 nm resolution, while piezoresistive approaches routinely report sub-nanometer to few-nanometer resolution over tens to hundreds of micrometers (e.g., 25 µm / 0.4 nm, 50 µm / 1 nm, and 140 µm / 10 nm). Capacitive sensors similarly reach 100 µm with 10 nm resolution, and resistive schemes emphasizing large range demonstrate ≥1 mm of displacement with sub-micrometer resolution.

By comparison, the device presented in this work occupies a deliberately different point in the design space, with a relatively short 0-20 µm range and coarse 2 µm spatial quantization. This apparent gap in range and resolution is the consequence of a distinct system-level trade-off. The devices reported in other works generally rely on active transduction and continuous analog or frequency-domain readout: piezoresistive and capacitive sensors require constant biasing, optical schemes demand tightly controlled alignment and higher power sources, and resonant devices need ongoing frequency tracking, all of which contribute to non-negligible static power consumption and increased electronic complexity.

In contrast, the transducer introduced here is fully passive in quiescent conditions. Under nominal operation, the system remains in a deep-sleep state, with current consumption in the nanoampere range. The microcontroller is activated only when mechanical contact occurs within the transducer, at which point a measurement is captured and processed. This event-driven operation yields extremely low average power dissipation while substantially simplifying the front-end electronics.

Although the complete system includes a microcontroller and a pull-down resistor network for readout, the proposed architecture remains fundamentally event-driven: the transducer is electrically open in quiescent conditions, such that the system can remain in deep-sleep with nanoampere-range current consumption and wake only when mechanical contact occurs, at which point a measurement is captured and processed.

Table 3.1 Comparison of MEMS-Based Strain and Displacement Sensors

Reference	Sensing Principle	Range	Resolution	Notes
(Sawada, Higurashi, Sanada, Chino, & Ishikawa, 2006)	Optical MEMS	1800 µm	10 nm	High power; large footprint
(Todorov, Stavrov, & Kreuter, 2011)	Piezoresistive	25 µm	0.4 nm	Continuous bias; power consumption
(Vladimir Stavrov, Todorov, Shulev, & Hardalov, 2013)	Piezoresistive	600 µm	1 nm	Continuous bias; power consumption
(X. Wang et al., 2022)	Resistive	≥1000 µm	0.8 µm	Continuous measurement; power consumption
(V. Stavrov, Tomerov, Stavreva, Hardalov, & Shulev, 2010)	Piezoresistive	140 µm	0.01 µm	Continuous bias; higher power
(V. Stavrov, Stavreva, & Shulev, 2016)	Piezoresistive	50 µm	0.001 µm	Continuous bias; higher power
(Kuijpers, Krijnen, Lammerink, Wiegerink, & Elwenspoek, 2003)	Capacitive	100 µm	0.01 µm	Continuous excitation; power consumption
(Wu et al., 2014)	Piezoresistive	4.6 µm	10 nm	Continuous bias; power consumption
This Work	Resistive	20 µm	2 µm	Passive; near-zero standby power

Even without optimization, the prototype consumes 2.8 µW at a 1 Hz reporting rate (1.8 V supply, 1.6 µA), with nearly 90% of the current attributable to the MCU and only minor contributions from the voltage-divider resistors connected to the transducer. In the implemented readout, each GPIO line is tied to ground through a high-value 100 MΩ pull-down resistor, so that the resistor-network contribution is negligible when the contact is open and only nanoampere-level per asserted contact during an event (i.e., ~1.8 V / 100 MΩ ≈ 18 nA).

As such, the passive, ultra-low-power, contact-based sensing paradigm introduced in this work complements existing high-resolution MEMS transducers by addressing application spaces where intermittent, event-driven readout and stringent energy budgets are more critical than sub-micrometer resolution, such as battery-powered or energy-harvested structural and displacement monitoring nodes.

3.6 Conclusion

This work experimentally evaluated three direct-contact MEMS strain transducer topologies: based on cantilevers (Device A), based on parallel doubly supported beams (Device B), and a concentric-ring variant (Device C). These were fabricated in the PiezoMUMPs process and read out with a 1.8 V microcontroller. The transducers provide step-coded displacement over 0-20 µm with 2 µm increments, validated using a 50 nm-resolution stage and resistance metrology. Because the transduction is passive, no bias is required before first contact. The complete system operates at 2.8 µW at a 1 Hz reporting rate, with ~90% of the current attributable to the MCU, indicating headroom for further power reduction.

Device C achieved the best overall performance. Its doubly supported beams and concentric semicircular contacts improved pressure distribution and alignment tolerance, yielding low and stable contact resistances (100 kΩ down to 18 kΩ after 4 µm engagement) and small hysteresis (typically within ±2 µm across most of the range). Tracking accuracy was notably improved relative to Devices A and B.

The results highlight a key process-driven limitation: the shallow doped region (~2~3 µm) within the 10 µm silicon layer. Vertical misalignment can shift contact to undoped silicon, elevating resistance and producing intermittent continuity. The geometric choices embodied in Device C, larger circular contacts and stiffer, doubly supported beams, mitigate this by increasing effective contact area and reducing torsion, offering practical design guidance for contact-based transducers in shallow-doped stacks.

Combined with a simple digital interface that senses individual contacts through high-value pull-down resistors, the demonstrated microwatt-class operation makes this passive approach well suited to autonomous, energy-constrained deployments (e.g., structural health monitoring nodes, implants). Future work will target improved contact surfaces via deeper doping or local metallization, as well as system-level miniaturization and MCU power reduction.

3.7 Acknowledgement

The authors thank CMC Microsystems for providing the necessary CAD tools and device fabrication services. They also acknowledge financial support from the Natural Sciences and Engineering Research Council of Canada (NSERC), the Microsystems Alliance of Quebec (ReSMiQ) and IPR Inc. for their financial support.

CHAPTER 4

DESIGN AND CHARACTERIZATION OF MULTI-FREQUENCY MEMS TRANSDUCERS FOR PHOTOACOUSTIC IMAGING

Alberto Prud'homme [a] and Frederic Nabki [a]

[a] Department of Electrical Engineering, École de Technologie Supérieure
1100 Notre-Dame West, Montréal, Quebec, Canada H3C 1K3

Paper submitted to MDPI Micromachines special issue *"MEMS and NEMS Sensors: Innovations, Applications, and Future Directions in Micro/Nano Technologies*",
December 2025

Abstract:

This work presents the design, fabrication, and experimental characterization of microelectromechanical system (MEMS) ultrasonic transducers engineered for multi-frequency operation in photoacoustic imaging (PAI). The proposed devices integrate multiple resonant geometries, including circular diaphragms, floated crosses, anchored cross membranes, and cantilever arrays, within compact footprints to overcome the inherently narrow frequency response of conventional MEMS transducers. All devices were fabricated using the PiezoMUMPs commercial microfabrication process, with finite element simulations guiding modal optimization and laser Doppler vibrometry used for experimental validation in air. The circular diaphragm exhibited a narrowband response with a dominant resonance at 1.69 MHz and a quality factor (Q) of 268, confirming the bandwidth limitations of traditional geometries. In contrast, complex designs such as the floated cross and cantilever arrays achieved significantly broader spectral responses, with resonances spanning from 275 kHz to beyond 7.5 MHz. The cantilever array, with systematically varied arm lengths, achieved the highest modal density through asynchronous activation across the spectrum. Results demonstrate that structurally diverse MEMS devices can overcome the bandwidth constraints of traditional piezoelectric transducers. The integration of heterogeneous MEMS geometries offers a viable approach for broadband sensitivity in PAI, enabling improved spatial resolution and depth selectivity without compromising miniaturization or manufacturability.

Keywords: MEMS transducers, Photoacoustic imaging, Multi-frequency Transducer, Piezoelectric devices, Ultrasonic transducer, Biomedical Imaging.

4.1 Introduction

Microelectromechanical systems (MEMS) have emerged as a transformative technology for enhancing the performance of photoacoustic imaging (PAI) systems. PAI, as a hybrid imaging modality that merges the optical contrast provided by photoacoustic effects with the deep tissue penetration capability of ultrasound, holds significant promise for a broad spectrum of biomedical applications. It enables high-resolution visualization of vascular structures, tumors, and molecular distributions within biological tissues, rendering it invaluable for both clinical diagnostics and preclinical research. The quality and adaptability of the resulting images are closely tied to the characteristics of the ultrasonic transducers employed to detect the photoacoustic signals. Historically, PAI platforms have depended on conventional ultrasound transducers; however, MEMS-based devices have recently emerged as an attractive alternative offering new functionalities and extended capabilities (Attia et al., 2019; Suttikittipong et al., 2025).

A fundamental requirement for transducers used in PAI is the ability to deliver both high sensitivity and broad frequency coverage, as the spectral content of photoacoustic signals varies widely with the size, composition, and depth of the absorbing structures. This variability arises from the diverse acoustic responses encountered in biological tissues. To maximize image resolution while maintaining penetration depth, it is necessary to employ transducers capable of efficient operation across multiple frequency bands (Ren et al., 2022).

Conventional PAI transducers are most often fabricated from piezoelectric materials such as lead zirconate titanate (PZT), which convert the mechanical vibrations of ultrasonic waves into electrical signals. Their operating frequency is typically dictated by the thickness of the piezoelectric layer, which sets the device's primary resonance. Depending on the target tissue or imaging application, these devices are designed for specific frequency ranges: higher frequencies (20–100 MHz) are suited for shallow imaging with fine spatial resolution, while lower frequencies (1–10 MHz) allow deeper penetration at the cost of reduced resolution (Manwar et al., 2022).

Despite their long-standing utility, conventional piezoelectric transducers encounter inherent constraints in multi-frequency imaging scenarios. The optimal transducer for PAI should detect a broad range of ultrasonic frequencies to accommodate signals generated from varying tissue depths, sizes, and compositions, as well as from different laser excitation conditions. High-frequency ultrasound is required to resolve microvascular networks and other fine structures, but is prone to rapid attenuation with depth. Conversely, low-frequency ultrasound enables deep imaging of larger anatomical features but lacks the resolution needed for smaller targets.

Although modern piezoelectric transducers can achieve fractional bandwidths exceeding 70%, enabling broader frequency coverage, their peak sensitivity typically remains centered around a single operating frequency. Achieving wideband sensitivity necessitates careful optimization of matching layers, backing materials, and the piezoelectric composition (D. Yang et al., 2007).

While advanced fabrication and piezocomposite materials have enabled more compact and high-density arrays for real-time volumetric imaging, these improvements are less effective when extreme miniaturization or unconventional geometries are required. These are conditions where micromachined ultrasound transducers are increasingly advantageous (Chan et al., 2019; B. Chen et al., 2013).

In practice, conventional systems often employ multiple transducers or array elements tuned to distinct frequency ranges to overcome the trade-off between penetration depth and resolution, increasing both system cost and mechanical complexity. Narrowband devices, in particular, face challenges in capturing the full spectral diversity of photoacoustic signals from complex tissue environments containing multiple coexisting frequency components. This limitation reduces versatility and restricts performance in dynamic, multi-layered, or heterogeneous tissue contexts. Since the ultrasonic signals generated by laser-induced optical absorption span a wide range of frequencies, their spectral content depends strongly on absorber size and composition (Xu & Wang, 2006). High frequencies are ideal for resolving minute structures such as capillaries or cellular features yet attenuate quickly with propagation through tissue. Low frequencies penetrate more deeply to visualize large-scale features such as organs or tumors but compromise spatial resolution, potentially obscuring fine morphological details (Yao & Wang, 2014).

For comprehensive PAI, where both superficial and deep targets must be imaged within a single acquisition, transducers must be capable of detecting across this wide frequency range. Such capability allows simultaneous visualization of superficial vascular details and deeper structural pathologies. Multi-frequency detection further enables advanced modalities such as spectroscopic PAI, in which different tissue components are discriminated based on their unique optical absorption and acoustic signatures at different frequencies. This approach supports tissue composition analysis, molecular marker detection, and differentiation between normal and diseased regions. Without such broadband access, the diagnostic potential of PAI is inherently limited.

MEMS ultrasonic transducers offer a compelling solution by enabling multi-frequency operation through geometrically engineered designs that incorporate multiple mechanical resonances within a miniaturized footprint (Liao et al., 2013). Unlike conventional transducers that operate predominantly at a single thickness mode, MEMS devices can be fabricated with suspended membranes, cantilever beams, or composite architectures that support multiple vibrational modes. This allows detection of ultrasonic signals across a broad frequency spectrum without a substantial loss in sensitivity (Jaber et al., 2016). The inherent broadband nature of such devices facilitates simultaneous acquisition of high-resolution superficial data and deeper structural information, enhancing axial resolution and penetration depth within a single imaging cycle.

The scalability and precision of MEMS microfabrication make it possible to design transducers with tailored higher-order vibrational modes and extended frequency responses. These characteristics are particularly advantageous for spectroscopic PAI, which leverages frequency-dependent acoustic responses to perform functional and molecular imaging beyond purely structural assessment. Additionally, the small form factor of MEMS devices facilitates integration with optical delivery systems and on-chip signal processing electronics, enabling the development of compact, high-performance and potentially lower cost imaging probes.

This work addresses the design, fabrication, and characterization of MEMS piezoelectric ultrasonic transducers specifically engineered for multi-frequency operation in PAI. The research targets the challenge of achieving broad spectral sensitivity to optimize both resolution and penetration depth for imaging biological samples of varying sizes and depths. By exploiting multi-resonant MEMS architectures, the approach aims to overcome the limitations of conventional piezoelectric designs, enhancing sensitivity, adaptability, and image quality for biomedical imaging applications such as vascular mapping, molecular characterization, and pathological assessment.

The remainder of this paper is organized as follows. Section II details the system integration, device stack, and fabrication using the PiezoMUMPs process, along with the four MEMS geometries under study. Section III presents measurement results obtained via finite element modeling and laser Doppler vibrometry. Section IV discusses implications for PAI, including immersion effects, compares performance against prior art, and outlines design trade-offs. Section V concludes with key findings and directions for future work, including optimization for immersed operation and heterogeneous array integration.

4.2 Materials and Methods

Four complementary resonant geometries were co-fabricated on a single MEMSCAP PiezoMUMPs die. The thin-film stack and layout are selected to limit mechanical cross-coupling and broaden the effective bandwidth without increasing area.

A representative cross-section of a device is Figure 4.1. The structure is formed from a 10 µm-thick single-crystal silicon layer, surface-doped to create a conductive region. An aluminum nitride (AlN) piezoelectric layer is deposited between this silicon layer, serving as the bottom electrode, and a patterned top metal electrode. Where electrical isolation is required, a silicon dioxide (SiO_2) layer is introduced to insulate the silicon from the top electrode.

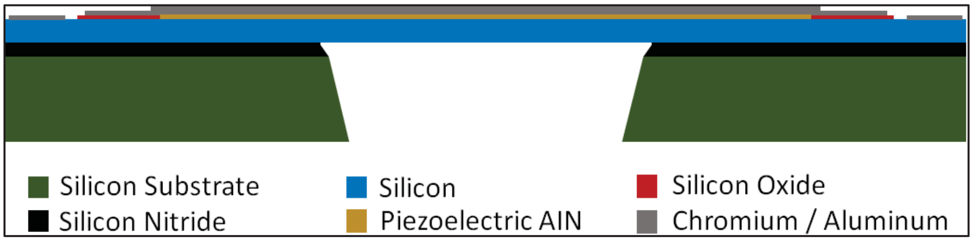

Figure 4.1 Cross-section of the micro-structures

The thin-film stack fabrication proceeds as follows: first, a 200 nm-thick SiO_2 layer is deposited on the silicon substrate and selectively etched to expose regions where the AlN layer must establish electrical contact with the underlying silicon. Next, a 0.5 µm-thick AlN film is deposited and patterned to define the active piezoelectric region. A top metal electrode stack, comprising a 20 nm chromium adhesion layer and a 1 µm aluminum layer, is then deposited and patterned.

All geometries developed in this work were designed in accordance with the dimensional tolerances and design rules of the fabrication process. These constraints affect sensitivity, resonance characteristics and bandwidth. The following subsections present the four evaluated microstructures.

4.2.1 Circular Diaphragm-Based MEMS Transducer

The first structure fabricated was a conventional circular diaphragm with a diameter of 300 μm, shown in Figure 4.2.This configuration represents the most basic and widely adopted geometry in MEMS acoustic sensing due to its fabrication simplicity, structural symmetry, and relatively high mechanical efficiency. While the circular diaphragm offers favorable sensitivity, it inherently exhibits a high quality (Q) factor, producing a sharply defined resonance peak. Such a narrowband response is suboptimal for PAI, where a broad frequency range is essential to achieve both high spatial resolution and depth-resolved imaging performance.

Finite element simulations predicted a first-mode resonance frequency of 1.85 MHz, corresponding to the fundamental vibrational mode of the diaphragm. This value was obtained under vacuum boundary conditions, assuming linear elastic behavior of the structural materials. Although the diaphragm supports multiple resonant modes, higher-order responses are typically of very low amplitude for this geometry. Consequently, most of the transduction occurs at the fundamental frequency, and the pronounced Q-factor effectively confines the operational bandwidth to a narrow spectral region. This limitation significantly reduces its suitability as a receiver for broadband PAI applications.

To address this constraint, complex geometries were designed with the goal of broadening the frequency response and enabling multiple high-amplitude resonance modes. Such designs are expected to enhance sensitivity across a wider spectral range, improving adaptability to the varying frequency content of photoacoustic signals generated at different tissue depths and with different optical absorption contrasts.

As previously mentioned, this multi-frequency behavior increases the potential utility of the transducer in PAI, allowing simultaneous imaging of fine superficial structures and deeper tissue layers.

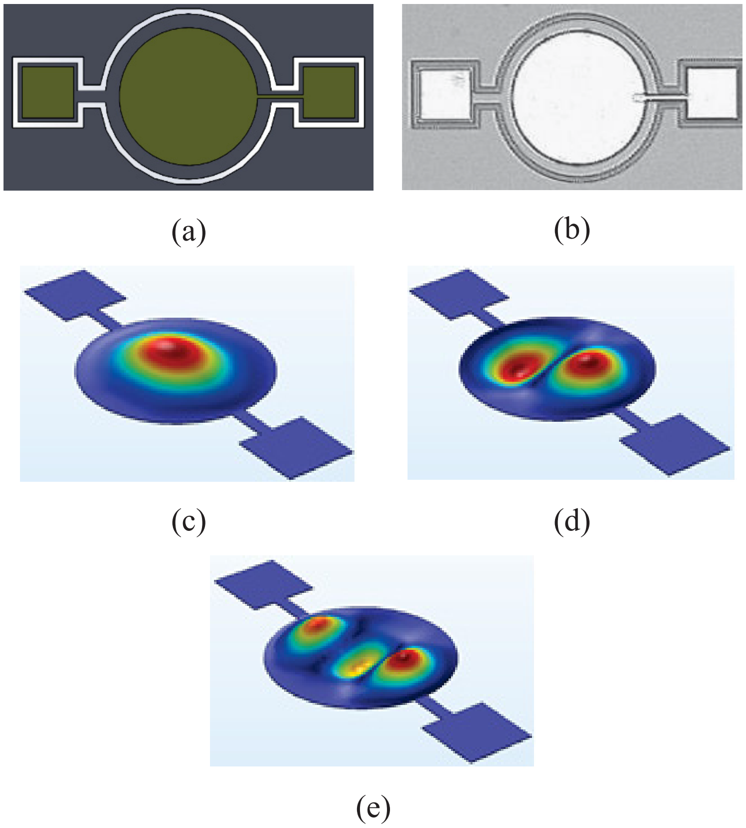

(a) (b)

(c) (d)

(e)

Figure 4.2 Circular diaphragm micro-structure at (a) Device CAD design, (b) Microscope image of the fabricated device, (c) Mode 1, (d) Mode 2 and (e) Mode 3

4.2.2 Floating Cross-Structured MEMS Transducer

The next microstructure design focuses on the integration of multiple cantilevers, suspended membranes, and a central region specifically engineered to exhibit high vibrational amplitude. This configuration, referred to as the floating cross, was developed to promote multimodal resonance behavior by incorporating mechanically distinct substructures, each with different stiffness, mass, and boundary conditions, into a single continuous architecture. As shown in Figure 4.3, the device consists of a central membrane region suspended by four lateral arms, each partially mechanically decoupled from the substrate to enhance dynamic displacement range and allow for independent modal contributions.

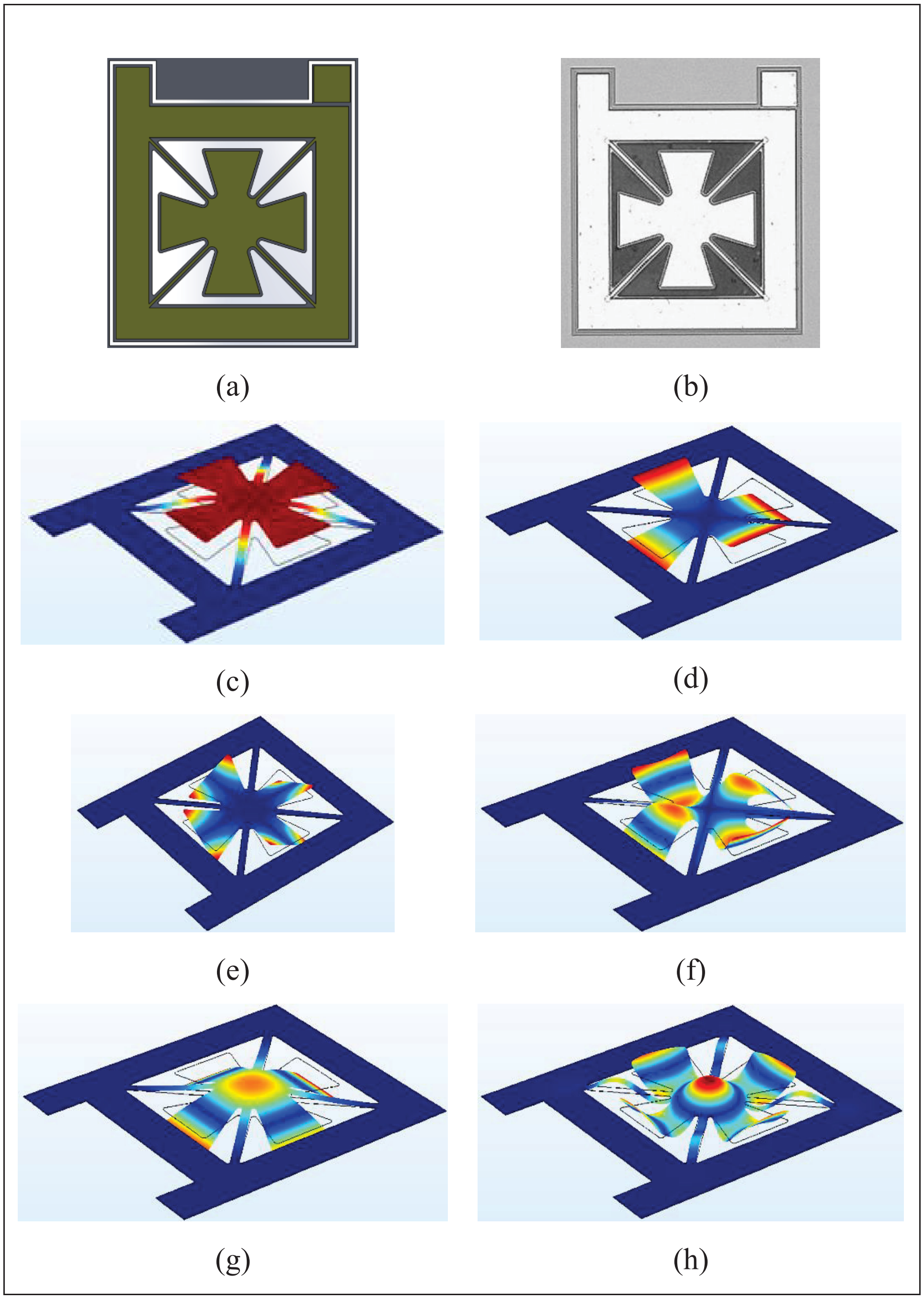
(a)
(b)
(c)
(d)
(e)
(f)
(g)
(h)

Figure 4.3 Floated cross micro-structure at (a) Device CAD design, (b) Microscope image of the fabricated device, (c) Mode 1, (d) Mode 2, (e) Mode 3, (f) Mode 4, (g) Mode 5 and (h) Mode 6

The design strategy aims to achieve frequency diversification by exploiting differences in mechanical impedance and geometric scaling between the central and peripheral elements. In this arrangement, the central membrane primarily dictates the low-frequency response, whereas the cantilever-like extensions generate higher-frequency resonances. Finite element simulations predict the first resonance mode, localized within the central membrane, at approximately 300 kHz. The cantilever arms reach their maximum displacement amplitude at a substantially higher frequency of around 800 kHz.

Owing to its geometrical complexity and the interplay between multiple vibrational domains, the floated cross is expected to produce a rich spectrum of higher-order resonant modes. These may involve hybrid coupling between the central membrane and peripheral cantilevers, resulting in spatially distributed and temporally overlapping displacement fields.

Such modal superposition facilitates broadband spectral coverage, enabling the transducer to respond effectively to a wider range of acoustic frequencies in order to benefit PAI.

4.2.3 Cross-Structured MEMS Transducer

The next microstructure design incorporates a central suspended membrane supported by four symmetrically arranged, inward-pointing anchor arms, forming the configuration referred to as the cross microstructure. This geometry, illustrated Figure 4.4, is engineered to promote a concentrated vibrational response in the central region, while the surrounding support structure minimizes constraints on the membrane and contributes to higher torsional frequency responses. Unlike previous designs employing elongated and mechanically distinct cantilevers, this structure adopts a simplified yet effective approach to achieving broadband vibrational behavior through a centrally suspended membrane connected by four narrow anchor arms. Finite element simulations indicate that the dominant resonance mode is localized within the central membrane, with a peak response at approximately 275 kHz, corresponding to its fundamental flexural oscillation.

Despite its relatively simple geometry, the cross microstructure demonstrates a notable ability to support multiple higher-order modes across a broad spectral range.

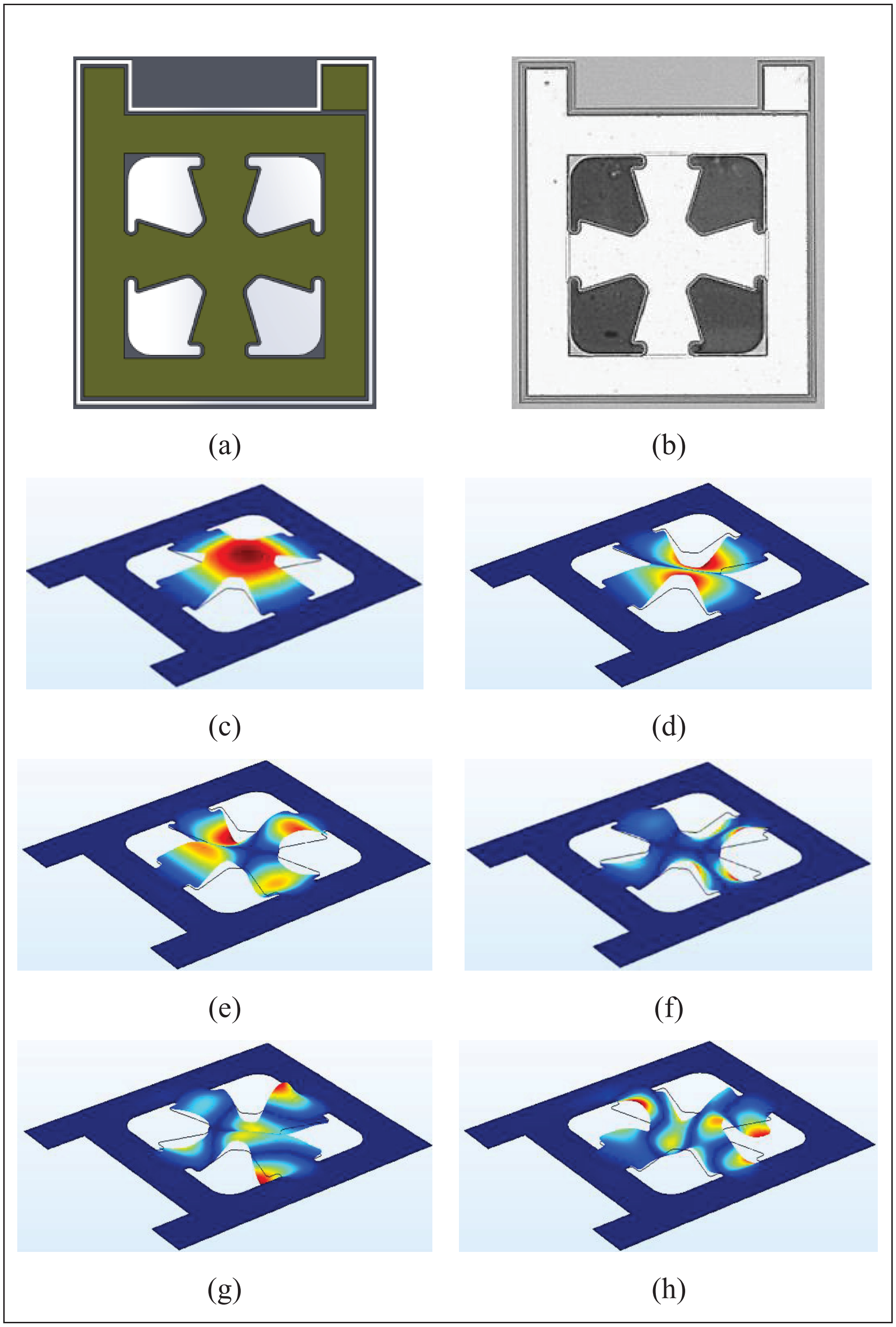

Figure 4.4 Cross micro-structure at (a) Device CAD design, (b) Microscope image of the fabricated device, (c) Mode 1, (d) Mode 2, (e) Mode 3, (f) Mode 4, (g) Mode 5 and (h) Mode 6

This capability is attributed to the dynamic behavior of the anchor arms, which can undergo both bending and torsional deformations under acoustic excitation. Functionally, these arms act as short cantilevers, introducing additional resonances beyond the fundamental mode. Their interaction with the central membrane results in mechanical coupling, producing hybrid vibrational modes that are distributed across the entire structure. This modal diversity is thus well suited to PAI systems.

4.2.4 Cantilevers combination MEMS Transducer

The final design evaluated consists of a closed-frame architecture incorporating a cantilever array with varying lengths and a uniform width. The cantilever lengths range from 115 μm to 25 μm, while the width is consistently maintained at 50 μm for all elements.

This configuration was intentionally developed to exploit the distinct mechanical responses associated with each cantilever geometry, thereby generating a dense and well-distributed set of resonance modes spanning a broad frequency range.

Each cantilever is capable of supporting multiple vibrational modes, both flexural and torsional, arising from differences in length and associated stiffness. Finite element simulations predict that the first resonance mode of the longest cantilever occurs at approximately 145 kHz, corresponding to a low-frequency flexural mode with high displacement amplitude. In contrast, the shortest cantilever exhibits its primary resonance well above 10 MHz, demonstrating the ability to achieve an exceptionally wide spectral span within a compact footprint.

In addition to these extremes, multiple intermediate resonances were identified and confirmed, with prominent modes observed at approximately 2.1 MHz, 2.6 MHz, and 5.5 MHz. Due to the high density of active modes, a detailed graphical representation of the device’s frequency response is provided in the Results section.

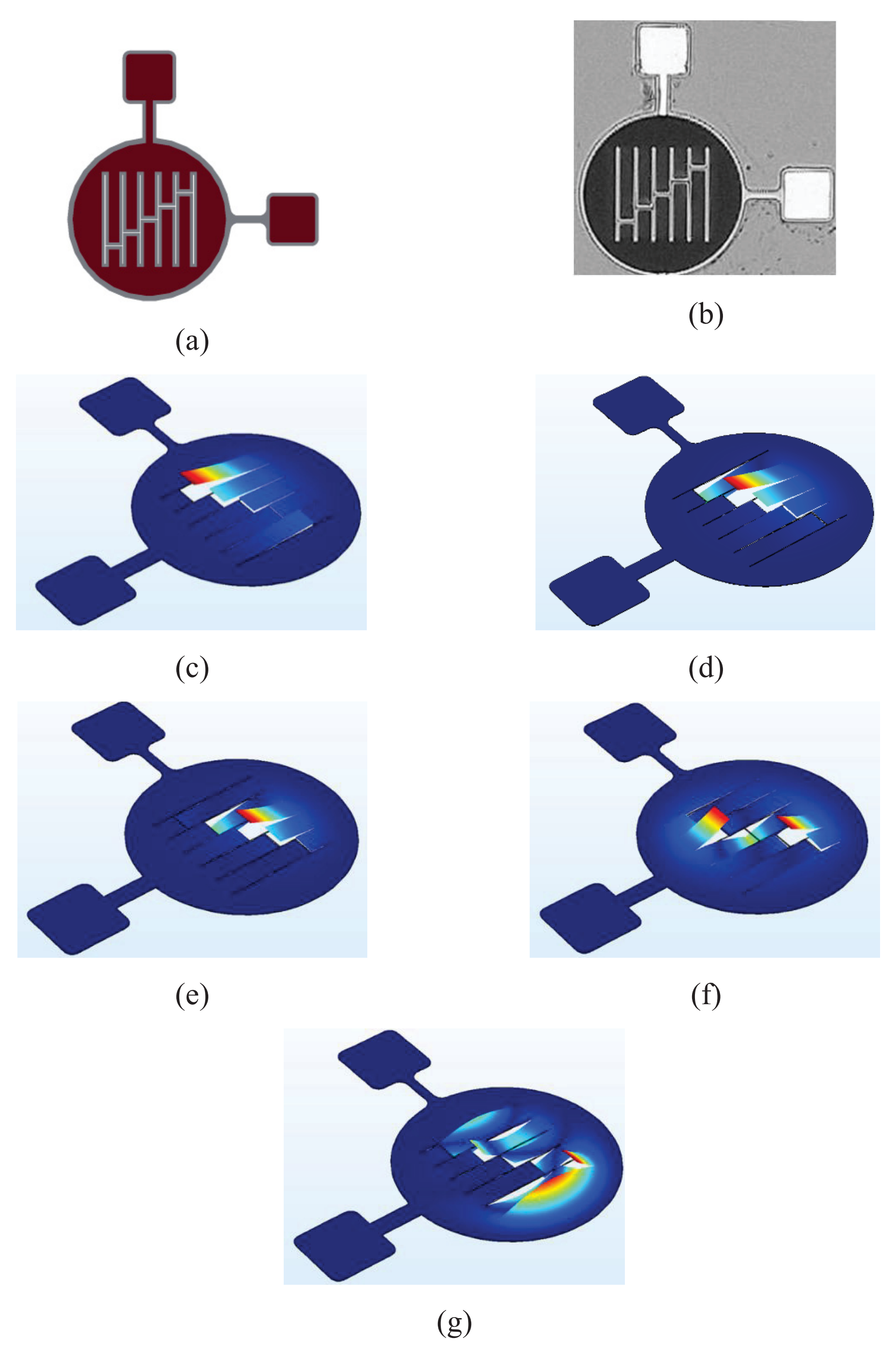

(a) (b) (c) (d) (e) (f) (g)

Figure 4.5 Cantilevers combination micro-structure at (a) Device CAD design, (b) Microscope image of the fabricated device, (c) Arm 1 Mode 1, (d) Arm 2 Mode 1, (e) Arm 3 Mode 1, (f) Arm 4 Mode 1and (g) Arm 5 Mode 1

As shown in Figure 4.5 may vibrate in its fundamental flexural mode while a shorter or stiffer arm resonates in a higher-order flexural or torsional mode. The resulting asynchronous, localized oscillations superpose to form a composite response with multiple concurrent spectral components, enabling effective operation over a broad frequency range.

4.3 Results

The vibrational responses of the fabricated MEMS microstructures were experimentally characterized using a Polytec OFV-534 laser Doppler vibrometer (LDV) in combination with an OFV-2570 controller. All measurements were performed at standard ambient temperature (approximately 22 °C) and atmospheric pressure. While practical PAI applications typically require immersion in a liquid medium, such as water or a higher-density acoustic coupling fluid, to ensure efficient acoustic transmission, the measurement setup available for this study did not permit submerged operation.

It is important to note that operating in air influences both resonance frequency and damping. Air loading is significantly lower than fluid loading, which leads to higher measured Q-factors and slight upward frequency shifts compared to immersed conditions. In a water-immersed scenario, viscous and acoustic loading would be expected to reduce Q-factors, broaden resonance peaks, and shift resonances to slightly lower frequencies. These effects are discussed in detail in the Discussion section, where the practical implications for PAI are considered.

The measured frequency response of the circular diaphragm microstructure is presented in Figure 4.6. As predicted by simulations, the spectrum is dominated by a single strong resonance corresponding to the fundamental flexural mode. The experimental fundamental frequency was measured at 1.69 MHz, closely matching the simulation value, and the Q-factor was extracted as approximately 268.

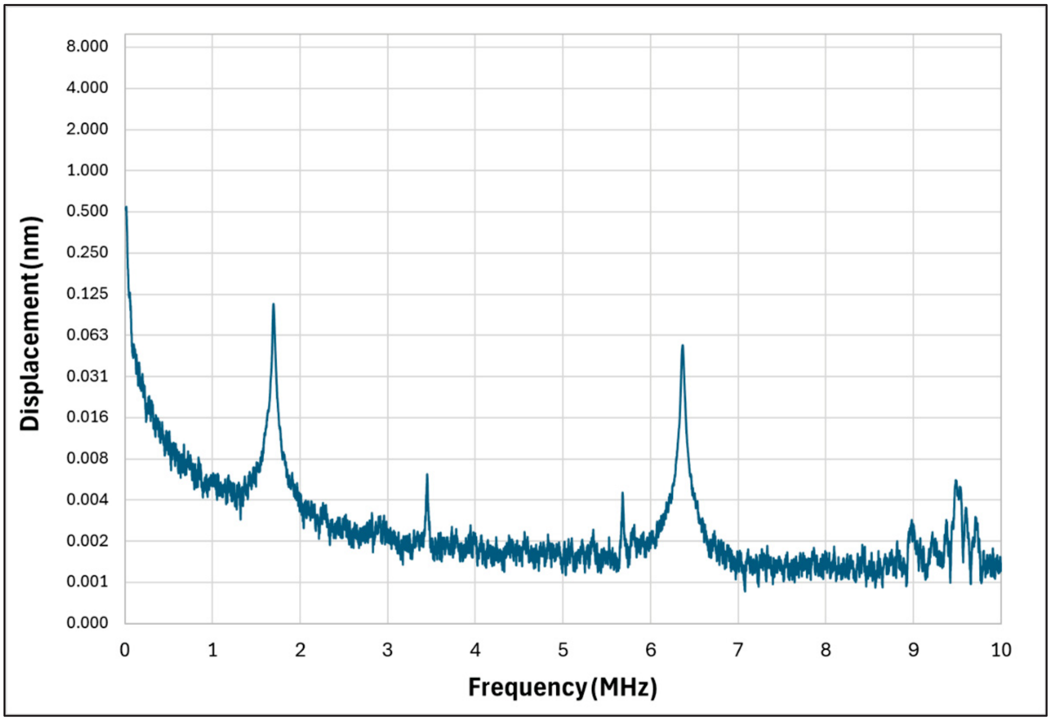

Figure 4.6 Circular diaphragm micro-structure vibrometer response

This high Q-factor confirms that the diaphragm experiences very low mechanical damping in air, concentrating vibrational energy into a narrow spectral window. Such behavior is highly beneficial for applications that require frequency stability or selective detection.

However, in PAI the narrow spectral bandwidth is a disadvantage. Broadband photoacoustic signals generated in tissue can extend from a few hundred kilohertz to beyond tens of megahertz, depending on absorber size and composition.

A sharply peaked response centered at 1.69 MHz means that much of this information is not captured, resulting in reduced axial resolution and incomplete depth profiling. While higher-order modes are present in the spectrum, their displacement amplitudes are significantly weaker, often below detectable thresholds for practical PAI, making the circular diaphragm effectively a single-frequency device. This confirms the need for alternative geometries that can sustain multiple, high-amplitude resonances over a broader range.

The floating cross design measured frequency response is shown in Figure 4.7, and exhibits a large number of observed resonance peaks. The primary low-frequency resonance was measured at 318 kHz with an exceptionally high Q-factor of 698. While this indicates strong mechanical confinement of energy, the resonance lies below the preferred operational range for most PAI applications. Furthermore, the high Q-factor again narrows the operational window for that specific mode.

More promising, however, are the distributed resonance peaks at higher frequencies, specifically in the 1.5–2.5 MHz and 6.5–7.5 MHz bands. These frequency regions correspond to modes involving both central membrane motion and higher order bending or torsional vibrations of the arms. In these ranges, displacement amplitudes were significantly higher than in surrounding spectral regions, suggesting that the floated cross can be tuned to emphasize modes relevant for PAI.

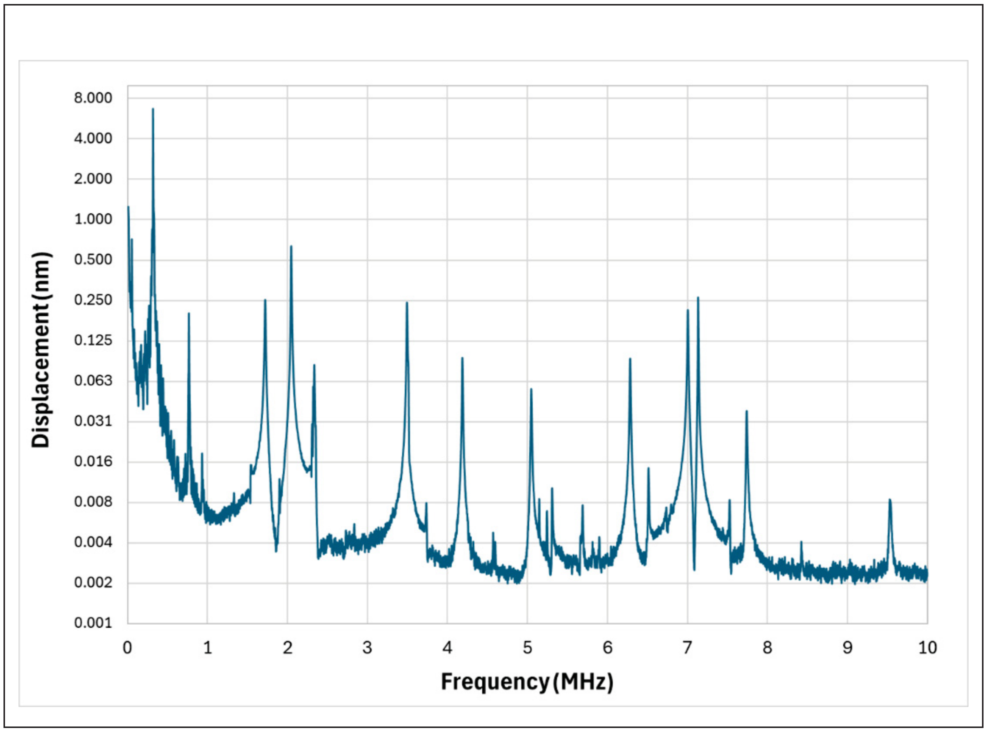

Figure 4.7 Floated cross micro-structure vibrometer response

Nevertheless, the spectrum is not continuous, there are wide frequency intervals with negligible amplitude, which would result in selective rather than uniform broadband sensitivity. This confirms that while the floated cross geometry achieves multi-modal behavior, optimization is still needed to improve mode density and minimize inactive spectral regions. Adjustments to arm stiffness, membrane thickness, or anchoring geometry could promote overlapping modes and enhance continuous spectral coverage.

The cross microstructure's frequency response is shown in Figure 4.8. The fundamental resonance of the central membrane was measured at 247 kHz with a Q-factor of 148. Although outside the optimal PAI band, this low-frequency mode is accompanied by multiple higher-frequency responses with significant amplitudes. Most notably, a broad region of activity was observed between 2.5 MHz and 5.2 MHz, suggesting the presence of overlapping modes from both membrane and arm vibrations. A secondary band of strong response was also measured around 7.5 MHz, likely associated with localized high-frequency modes in stiffer or smaller structural regions.

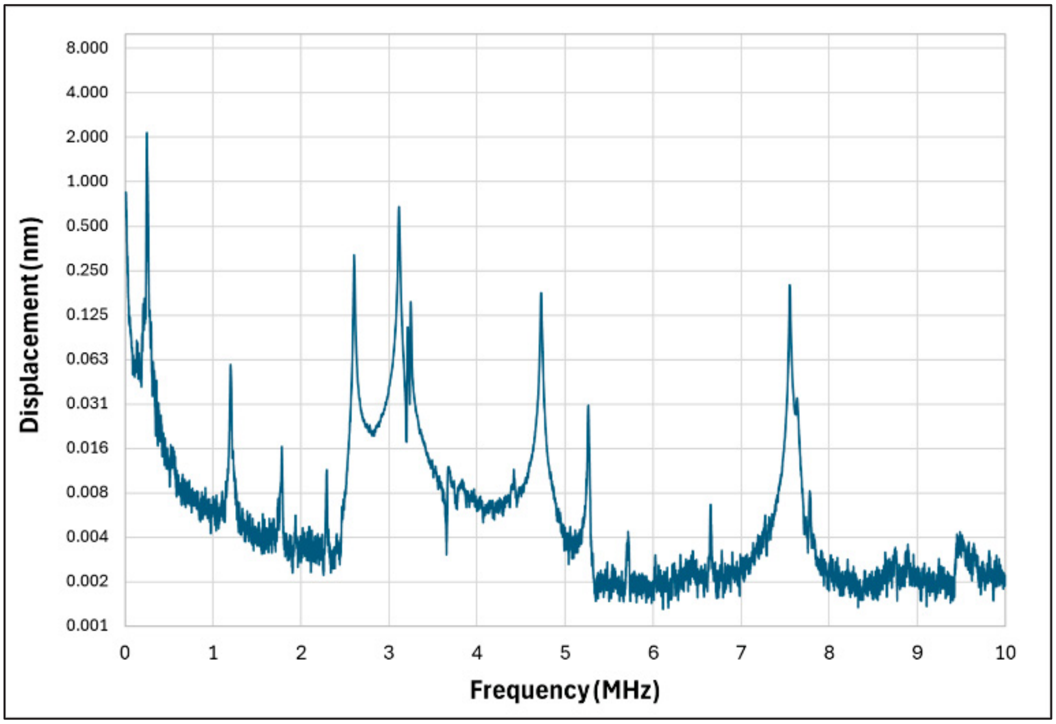

Figure 4.8 Cross micro-structure vibrometer response

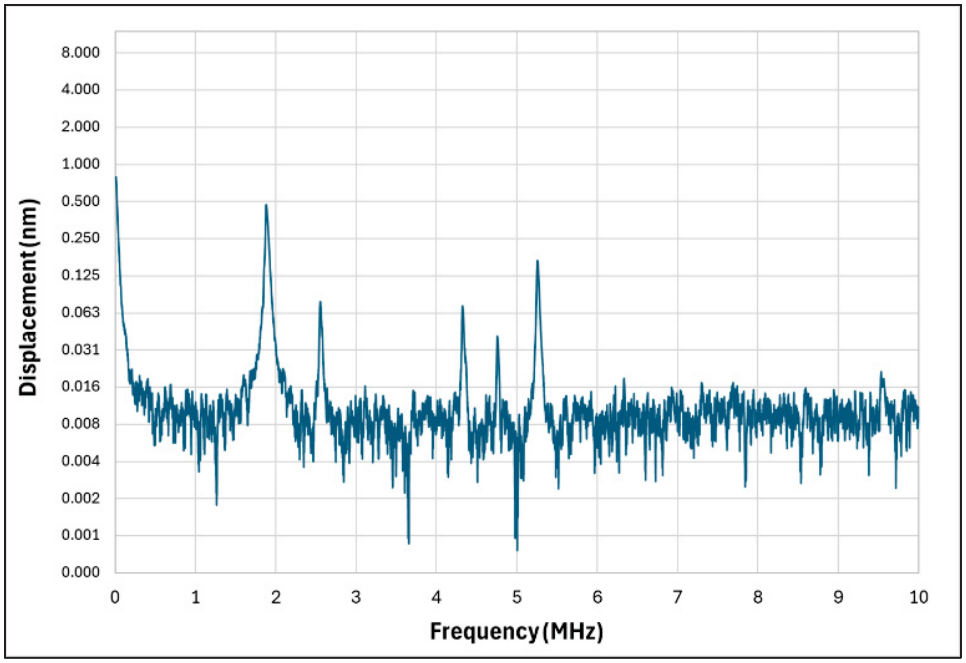

Figure 4.9 Cantilever array microstructure frequency response

Compared to the floating cross, the cross geometry offers a more continuous distribution of high-frequency modes, despite its simpler form. This may be due to stronger coupling between the arms and membrane, which promotes energy transfer across multiple modes. In PAI terms, this translates to improved ability to capture signals from both superficial and moderately deep tissues without large frequency gaps in sensitivity.

The cantilever-array's measured frequency response is presented in Figure 4.9. The longest cantilever exhibited a first-mode resonance at 1.8 MHz with a Q-factor of 204, producing strong displacement amplitude in the lower-megahertz range.

Due to the substantial cantilever length variation the shorter cantilevers are expected to resonate at frequencies exceeding 10 MHz. However, the LDV measurement bandwidth in this study did not extend into this range, so these high-frequency modes are absent from the presented data. Within the measurable range, multiple secondary peaks were observed at intermediate frequencies, but their high Q-factors resulted in relatively narrow, isolated resonances.

While the cantilever array achieves spectral diversity, the lack of modal overlap limits continuous broadband coverage. This limitation could be addressed in future designs by slightly altering cantilever lengths to promote modal convergence, introducing controlled damping to broaden peaks, or varying cantilever widths to encourage hybrid mode formation.

4.4 Discussion

The design and experimental characterization of the proposed MEMS transducers demonstrate the suitability of multi-resonant microstructures for broadband photoacoustic detection. Conventional diaphragms, although simple and mechanically efficient, exhibit high Q and narrow bandwidth; the circular diaphragm measured here shows a sharp resonance at 1.69 MHz ($Q \approx 268$), which limits capture of broadband waveforms from absorbers of varying sizes and depths.

Alternative geometries, the floating cross, the cross configuration, and the cantilever array, provide broader coverage through multimodal vibration. By distributing resonators within a single structure, they generate overlapping modes across the low-megahertz range relevant to tissue imaging. The floating cross shows strong activity in the 1.5–2.5 MHz and 6.5–7.5 MHz bands, but its 318 kHz mode with $Q \approx 698$ highlights a trade-off between reach and uniformity due to gaps in amplitude. The cross configuration offers a more balanced response: although its 247 kHz fundamental lies below the target band, it exhibits sustained activity from 2.5–5.2 MHz and near 7.5 MHz, with compliant arms adding higher-order torsional and flexural modes without excessive structural complexity.

The cantilever array, with lengths from 115 µm to 25 µm, yields a dense set of discrete resonances from sub-megahertz to beyond 10 MHz; measured activity centers near 1.8 MHz with additional peaks up to 5.5 MHz.

Table 4.1 Similar works for MEMS transducers

Ref	**Shape**	**Dimensions (µM)**	**Resonator Type**	**Frequency (Hz)**
(Y. Yang et al., 2013)	Square	1000 µM	pMUT	2 MHz
(Dangi et al., 2018)	Circular	125 µM	pMUT	10 MHZ
(Zheng et al., 2022)	Variable	Various	pMUT	1-8MHz
(Sun et al., 2022)	Circular	170 µM	pMUT	508 KHz
(Lu, Tang, Fung, Wang, et al., 2015)	Circular	100 µM	pMUT	22 MHz
(Lu, Tang, Fung, Boser, et al., 2015)	Circular	50 µM	pMUT	8 MHz
(J. Wang et al., 2020)	Square	250 µM	cMUT	5 MHz
(H. Wang et al., 2021)	Circular	220 µM	pMUT	1.2 MHz
(Sadeghpour et al., 2021)	Circular	160 µM	pMUT	6 MHz
T.W	Complex	Various	pMUT	1-3.5MHz

Asynchronous activation of individual arms produces a spatially distributed, frequency-diverse profile. The comb-like spectrum suggests value in lowering Q or promoting mode coupling, e.g., via slight geometric asymmetries or passive damping (thin polymer layers, fluidic loading), to broaden and flatten bands for broadband reception.

All measurements were conducted in air at atmospheric pressure. Immersion in water or a coupling fluid will introduce viscous and acoustic loading that lowers Q, shifts resonances slightly downward, and broadens peaks, improving functional bandwidth and mode uniformity relative to air operation.

Future work should quantify electromechanical coupling and evaluate photoacoustic reception in tissue-mimicking phantoms. Mode shape distribution and the resulting acoustic aperture and angular response should be analyzed, as these factors affect image fidelity and depth resolution in PAI.

Because of their minimal physical footprint, the fabricated MEMS transducers can be laterally integrated on a single substrate with multiple distinct geometries, forming a heterogeneous array in which each element possesses a unique and complementary vibrational signature. The collective frequency response of this array spans an acoustic bandwidth that exceeds that of any individual element. Consequently, passive spectral decomposition can be performed at the sensor level, enhancing both spatial resolution and penetration depth without requiring active frequency tuning or elaborate post-processing.

Figure 4.10 shows a synthesized composite response obtained by combining the measured spectra of the circular diaphragm, floating cross, cross configuration, and cantilever array. Bands from 1.5–3.5 MHz and 6.25–7.75 MHz exhibit enhanced modal density due to overlap, aligning with expected photoacoustic spectra for absorbers at varying scales and depths.

Relative to prior work listed in Table 4.1 Similar works for MEMS transducers, which largely emphasizes circular piezoelectric micromachined ultrasonic transducers (PMUTs) and a capacitive micromachined ultrasonic transducer (CMUT), the present results underscore the need for alternative geometries and controlled damping when broadband or time-critical

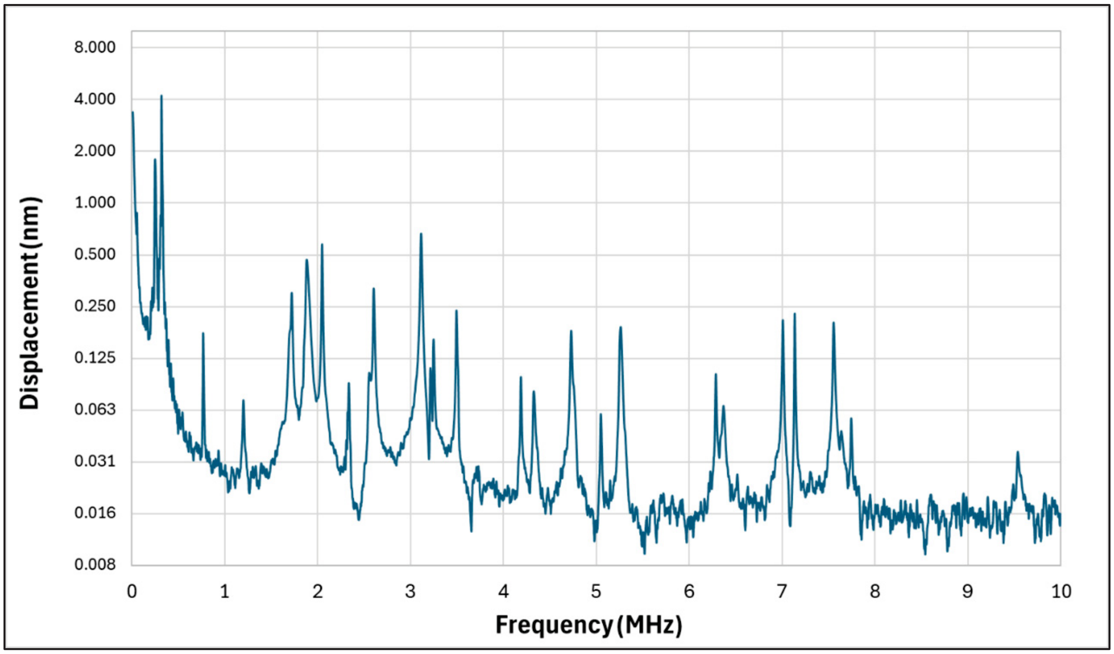

Figure 4.10 Combined devices expected vibrometer response

detection is required. Non-circular membranes, damping layers, and optimization for anchor loss and air/fluid damping provide practical routes to tailor Q and bandwidth to application needs. Overall, although air-based measurements were used, the comparative analysis clarifies strengths and weaknesses of each geometry and supports heterogeneous MEMS designs as a viable path to the broadband characteristics required for advanced PAI.

4.5 Conclusion

This work experimentally demonstrated MEMS ultrasonic transducers with broadband, multi-frequency response suitable for PAI. A comparative evaluation of four geometries, circular diaphragm, floating cross, cross configuration, and a cantilever array, showed that structural complexity and modal diversity extended frequency coverage and improved adaptability to the spectral content of photoacoustic signals. In contrast to the single narrowband resonance of a circular diaphragm, hybrid and distributed microstructures produced overlapping modes that broadened the usable band.

Future work will focus on refining these designs for immersion operation, optimizing fabrication processes to improve mechanical symmetry and electrical integration, and evaluating photoacoustic sensitivity under in situ optical excitation. The integration of such MEMS transducers into compact imaging arrays offers significant potential for high-resolution, real-time biomedical imaging, particularly in scenarios where spatial selectivity and penetration depth must be balanced without compromising device miniaturization or power efficiency.

4.6 Acknowledgement

The authors thank CMC Microsystems for CAD tools and device fabrication, and the Natural Science and Engineering Research Council of Canada (NSERC) and Microsystems alliance of Quebec (ReSMiQ) for their financial support.

CONCLUSION

This thesis advanced photoacoustic imaging and cross-domain diagnostics by studying compact subsystems: (i) avalanche-transistor-driven high-power LED excitation, (ii) multi-frequency MEMS ultrasonic transducers, and (iii) ultra-low-power MEMS strain/displacement sensors. Together, these elements address the two main barriers to portable PAI, bulky, costly laser sources and narrowband piezoelectric receivers, while adding a potential path towards a mechanical feedback channel to quantify motion and coupling.

Beyond the optical excitation subsystem, this thesis introduced multi-frequency MEMS ultrasonic transducers fabricated via the PiezoMUMPs process, capable of covering a broad frequency spectrum (0.3–8 MHz). These devices demonstrated that carefully engineered geometries—circular diaphragms, cantilever arrays, floating and anchored crosses—can overcome the bandwidth limitations of traditional piezoelectric transducers. By enabling simultaneous capture of high-frequency superficial detail and low-frequency deep-tissue information, these MEMS devices establish a new paradigm for compact, broadband acoustic detection in PAI.

In parallel, the development of passive MEMS strain and displacement sensors with sub-micrometer resolution and microwatt-level power consumption provided an additional dimension to this research. Their robustness, digital-ready output, and zero-standby power make them not only suitable for integration into photoacoustic systems as monitoring or calibration nodes, but also highly valuable for applications in biomedical implants, wearable electronics, and structural health monitoring. These sensors can be made part of motion compensation or coupling calibration in future work touching on an integrated PIA system.

The integration of these optical, acoustic, and mechanical components into fully functional experimental platforms has validated the feasibility of a miniaturized, and low-power PAI solution. The results confirm that LED-driven excitation, can generate and capture photoacoustic signals in both air and water with clinically relevant fidelity. Moreover, the modular design philosophy adopted in this work has demonstrated clear adaptability beyond biomedical imaging, extending into fields such as non-destructive industrial testing, environmental sensing, and cross-domain diagnostics.

Overall, this research represents a comprehensive advance toward the democratization of photoacoustic imaging: from benchtop, laser-dependent systems to portable, affordable, and versatile platforms. It contributes to the scientific understanding of fast LED excitation, MEMS-based acoustic sensing, and ultra-low-power mechanical detection, while also offering a blueprint for their co-integration into scalable diagnostic tools.

Looking ahead, the insights gained here point to several promising directions: optimization of signal-to-noise ratios through advanced circuit and packaging design; integration of MEMS arrays with on-chip signal conditioning and wireless telemetry; exploration of new wavelengths and LED array geometries for multispectral PAI; and extension of passive MEMS sensing concepts into energy-autonomous implantable systems. Such developments could catalyze the emergence of next-generation diagnostic technologies that are not only more compact and cost-effective, but also accessible in resource-limited settings, ultimately broadening the impact of photoacoustic imaging in medicine, industry, and beyond.

Novelty Aspect and Importance of the Project

The novelty of this work resides primarily in the translation of avalanche transistor technology—historically confined to radar, pulsed power, and nuclear instrumentation—into the domain of biomedical imaging light sources. This adaptation enabled the generation of sub-100 ns, high-amplitude current pulses in a compact and thermally efficient form factor, directly driving high-power LEDs for photoacoustic excitation. The result is a light source paradigm that departs fundamentally from bulky, costly Q-switched lasers, yet delivers temporally confined optical bursts that are fully compatible with high-resolution PAI.

The significance of this innovation is multifaceted and extends beyond the optical driver itself:

Technical Breakthrough — By leveraging avalanche transistors for ultra-fast current delivery, the system achieves nanosecond-scale optical excitation profiles suitable for stress and thermal confinement in tissues. This marks a critical step in validating LEDs as true competitors to pulsed lasers in PAI.

Cost Reduction and Accessibility — The driver–LED configuration reduces overall system cost by at least an order of magnitude relative to laser-based setups. This economic advantage directly supports the democratization of photoacoustic imaging, enabling adoption in point-of-care, low-resource, and field-deployable diagnostics.

Multi-Frequency MEMS Transducers — A central novelty of this project is the design and fabrication of multi-resonant ultrasonic MEMS devices capable of spanning a wide frequency range (0.3–8 MHz). Through innovative geometrical architectures—including circular diaphragms, floating and anchored cross structures, and cantilever arrays—these transducers demonstrated the ability to combine high-frequency modes for superficial detail with low-frequency modes for deep penetration. This multi-modal resonance strategy effectively resolves the long-standing trade-off in PAI between resolution and penetration depth, offering a single compact device capable of broadband detection. Moreover, the modularity of MEMS fabrication enables integration of diverse structures on the same chip, laying the groundwork for array-based systems and advanced spectral imaging techniques.

Ultra-Low-Power MEMS Strain and Displacement Sensors — In parallel, this work introduced passive MEMS strain sensors employing a direct-contact transduction mechanism. Unlike conventional piezoresistive or capacitive sensors, these devices consume virtually no standby power and operate in the microwatt range (~2.8 µW total, including readout). Experimental validation confirmed sub-2 µm resolution over a 20 µm displacement range, making them exceptionally precise despite their low energy footprint. Their robustness, binary digital-friendly output, and compact form factor render them highly suitable not only for integration within PAI systems (e.g., for calibration, displacement tracking, or mechanical coupling monitoring) but also for structural health monitoring, wearable biomechanical sensing, and implantable biomedical devices. This contribution highlights the cross-domain versatility of MEMS platforms: a single fabrication process can yield both optical-acoustic transducers and mechanical strain sensors, enabling multi-functional diagnostic chips.

The value of this is work lies not only in pioneering the avalanche-driven LED excitation paradigm for photoacoustics, but also in introducing multi-frequency MEMS transducers and ultra-low-power strain sensors as integral components of a unified photoacoustic platform.

Collectively, these advances establish a holistic engineering framework—optical, acoustic, and mechanical—that redefines the design space of portable diagnostic technologies. This project thus positions itself at the intersection of semiconductor optoelectronics, MEMS acoustics, and microscale mechanical sensing, ensuring both scientific impact and translational potential across biomedical, industrial, and environmental domains.

Potential Applications

The technological advancements achieved in this work open the door to a wide range of applications, both within and beyond the biomedical imaging domain. By integrating avalanche-driven LED excitation, multi-frequency MEMS ultrasonic transducers, and ultra-low-power MEMS strain sensors, the developed platform provides a versatile foundation for next-generation diagnostic and monitoring systems.

Point-of-Care Medical Diagnostics: Portable LED-based PAI systems could be deployed in rural or resource-limited settings for rapid and affordable assessment of vascular diseases, tumor detection, and inflammatory conditions. The low cost and compactness of the LED driver–MEMS transducer combination make it feasible to deliver high-quality imaging in primary care or mobile health units where traditional laser-based systems are impractical.

Preclinical and Translational Research: The modularity and reproducibility of MEMS-based devices provide a scalable solution for small-animal imaging laboratories. Broadband, multi-frequency detection allows simultaneous visualization of superficial microvascular structures and deeper tissue perfusion, supporting studies in oncology, cardiovascular biology, and neurovascular coupling. The cost-effectiveness of the system further enables high-throughput preclinical imaging pipelines.

Intraoperative and Image-Guided Surgery: Real-time visualization of tissue oxygenation and perfusion could significantly enhance surgical precision in tumor resections, flap monitoring in reconstructive surgery, and vascular graft validation. The portability of LED-driven excitation combined with MEMS transducers could eventually enable handheld intraoperative probes, reducing reliance on bulky intraoperative MRI or CT systems.

Industrial and Non-Destructive Testing (NDT): Beyond biomedicine, the multi-frequency MEMS transducers are well suited for detecting subsurface defects, delamination, and crack propagation in composite materials or metals. Their broadband acoustic response enables detection across scales, from microcracks to bulk structural anomalies. In addition, the passive MEMS strain sensors can be embedded directly into infrastructure components (bridges, aerospace panels, pipelines) for continuous structural health monitoring, operating at microwatt-level power budgets ideal for IoT-enabled smart infrastructure.

Wearable and Implantable Health Monitoring: The ultra-low-power MEMS strain/displacement sensors developed in this works are particularly attractive for wearable and implantable devices. Their ability to operate with negligible standby power enables long-term monitoring of biomechanical signals such as joint movement, arterial pulse waveforms, or respiratory strain. When combined with LED-based PAI, this creates opportunities for hybrid wearable diagnostics capable of both hemodynamic imaging and mechanical feedback in real time.

Environmental and Cross-Domain Diagnostics: The modular optical and acoustic subsystems could be repurposed for environmental monitoring, such as detecting contaminants in water through photoacoustic spectroscopy, or acoustic emissions in air for smart city sensing. The LED-based avalanche driver can also serve as a compact optical pulse source for low-cost spectroscopy, LiDAR, or short-range optical communications.

Taken together, the combination of performance, miniaturization, and affordability positions this work as a potentially transformative enabler across established and emerging imaging markets, by merging cost-efficient LED excitation with MEMS-based broadband detection and ultra-low-power strain/displacement sensing, the work presented here lays the foundation for next-generation diagnostic systems that are portable, versatile, and accessible beginning to bridge the gap between laboratory innovation and real-world impact.

Future Work

While the outcomes of this research are promising, several avenues remain open for further exploration and refinement to fully unlock the potential of avalanche-driven LED excitation and MEMS-based sensing platforms for PAI and cross-domain diagnostics:

Full System-on-Chip (SoC) Integration: One of the most critical next steps is the integration of all componenta, LED driver, MEMS ultrasonic transducers, and strain sensors, into a unified system-on-chip platform. While microfabrication processes such as PiezoMUMPs are valuable for evaluation, real-world deployment requires more flexible MEMS processes and robust packaging. Future work must address the co-integration of MEMS with CMOS electronics, embedding low-noise amplification, signal conditioning, and wireless telemetry directly on-chip. This approach would drastically reduce parasitic capacitances, improve signal-to-noise ratios, and enable true plug-and-play miniaturized photoacoustic devices.

Refinement of Multi-Frequency MEMS Transducers: While this work demonstrated the feasibility of MEMS devices spanning 0.3–8 MHz, future research should focus on optimizing modal density, Q-factor control, and array integration. Co-fabricated multi-element MEMS arrays could provide synthetic aperture imaging, improved depth resolution, and tailored directional sensitivity. Exploring new piezoelectric materials (e.g., ScAlN, PMN-PT) may further enhance bandwidth and electromechanical coupling.

Optimization of LED Spectral Profiles; Tailoring emission spectra to specific photoacoustic contrast agents or endogenous chromophores (e.g., oxy/deoxy-hemoglobin, melanin, lipids) would significantly enhance both contrast and penetration depth. Strategies may include multi-wavelength LED arrays, bandpass filtering, or even hybrid LED–laser sources for application-specific tuning.

Integration with Advanced Reconstruction Algorithms: The lower optical fluence of LEDs compared to pulsed lasers could be mitigated by coupling the system with machine learning-based image reconstruction and model-based inversion algorithms. Such approaches can improve resolution, enhance spectral unmixing, and increase signal-to-noise ratios, allowing LED-based PAI to approach the fidelity of laser-based systems.

Advances in Passive MEMS Strain and Displacement Sensors: Future work can expand on the proof-of-concept presented here by improving contact reliability, hysteresis reduction, and multi-axis strain detection. Integration into wireless telemetry platforms and battery-free operation via energy harvesting would extend their applicability to implantables, wearables, and large-scale distributed IoT sensing networks.

Pursuing these directions will help realize the disruptive potential of avalanche-transistor-driven LED excitation combined with multi-frequency MEMS sensing. In particular, the shift toward integrated SoC architectures with industrial microfabrication processes represents the decisive step from laboratory prototypes to scalable, clinically and commercially viable products. Together, these advancements could catalyze the emergence of next-generation, affordable, and portable imaging systems, bridging the gap between academic innovation and widespread clinical, industrial, and environmental deployment.

Conclusion

This work has validated that it is both feasible and advantageous to replace traditional, bulky, and costly components of photoacoustic and ultrasonic systems with compact, low-cost, solid-state devices. The avalanche-driven LED excitation source, the passive MEMS strain sensor, and the broadband multi-frequency MEMS ultrasonic transducer each address fundamental barriers in optical excitation, mechanical sensing, and acoustic detection, respectively. Together, they form the foundation of a new technological paradigm: portable, energy-efficient, and multifunctional sensing systems.

The avalanche oscillator provides a disruptive alternative to Q-switched lasers, proving that nanosecond optical excitation with MHz repetition rates can be delivered safely, reliably, and at a fraction of the cost.

The MEMS passive strain/displacement sensor redefines energy efficiency by eliminating the need for continuous bias, enabling event-triggered, near-zero-power sensing.

The multi-frequency MEMS transducers resolve the long-standing trade-off between penetration depth and resolution in ultrasound by offering broadband frequency coverage on a single chip. Each innovation thus not only competes with, but in many respects surpasses, the conventional state of the art.

The broader impact of this work lies in its scalability across domains. These devices, while validated in the context of biomedical photoacoustic imaging, are equally applicable to structural health monitoring, industrial non-destructive testing, environmental sensing, and next-generation IoT systems. Their low cost, robustness, and compatibility with large-scale integration position them as a platform technology that can democratize access to advanced sensing and imaging capabilities.

Looking ahead, the next frontier will be the custom fabrication and heterogeneous integration of these components into unified microsystems. While academic processes such as PiezoMUMPs enabled rapid prototyping, real-world deployment will require MEMS microfabrication flows that are CMOS-compatible, scalable, and optimized for industrial productization. Future efforts must therefore focus on developing system-on-chip architectures in which the avalanche driver, MEMS transducers, and passive strain sensors are monolithically or heterogeneously co-integrated with on-chip amplification and signal conditioning. Such integration will not only minimize electrical noise and parasitics but also enable true plug-and-play photoacoustic microsystems with superior robustness and reproducibility.

These advances will make possible the realization of fully solid-state, handheld photoacoustic imaging systems, wearable health monitors, and distributed sensor networks capable of continuous, autonomous operation at ultra-low cost. In doing so, they will extend the reach of photoacoustic and ultrasonic sensing technologies far beyond research laboratories and tertiary hospitals, into homes, primary care clinics, industrial sites, and smart infrastructures.

BIBLIOGRAPHY

Aboonajmi, M., & Faridi, H. (2016). Nondestructive quality assessment of Agro-food products. *3rd International Iranian NDT Conference*. doi: IRNDT 2016-A13105

Adachi, Y., & Hoshimiya, T. (2013). Photoacoustic Imaging with Multiple-Wavelength Light-Emitting Diodes. *Japanese Journal of Applied Physics, 52*(7S), 07HB06. doi: 10.7567/JJAP.52.07HB06. Repéré à https://dx.doi.org/10.7567/JJAP.52.07HB06

Aebersold, J., Walsh, K., Crain, M., Martin, M., Voor, M., Lin, J. T., . . . Naber, J. (2006). Design and development of a MEMS capacitive bending strain sensor. *Journal of Micromechanics and Microengineering, 16*(5), 935. doi: 10.1088/0960-1317/16/5/009. Repéré à https://dx.doi.org/10.1088/0960-1317/16/5/009

Allen, T. J., & Beard, P. C. (2016). High power visible light emitting diodes as pulsed excitation sources for biomedical photoacoustics. *Biomedical Optics Express, 7*(4), 1260-1270. doi: 10.1364/BOE.7.001260. Repéré à https://opg.optica.org/boe/abstract.cfm?URI=boe-7-4-1260

Ansari, R., Zhang, E. Z., Desjardins, A. E., & Beard, P. C. (2018). All-optical forward-viewing photoacoustic probe for high-resolution 3D endoscopy. *Light: Science & Applications, 7*(1), 75. doi: 10.1038/s41377-018-0070-5. Repéré à https://doi.org/10.1038/s41377-018-0070-5

Attia, A. B. E., Balasundaram, G., Moothanchery, M., Dinish, U. S., Bi, R., Ntziachristos, V., & Olivo, M. (2019). A review of clinical photoacoustic imaging: Current and future trends. *Photoacoustics, 16*, 100144. doi: https://doi.org/10.1016/j.pacs.2019.100144. Repéré à https://www.sciencedirect.com/science/article/pii/S2213597919300679

Beard, P. (2011). Biomedical photoacoustic imaging. *Interface Focus, 1*(4), 602-631. doi: doi:10.1098/rsfs.2011.0028. Repéré à https://royalsocietypublishing.org/doi/abs/10.1098/rsfs.2011.0028

Bulsink, R., Kuniyil Ajith Singh, M., Xavierselvan, M., Mallidi, S., Steenbergen, W., & Francis, K. J. (2021). Oxygen Saturation Imaging Using LED-Based Photoacoustic System. *Sensors, 21*(1), 283. doi: 10.3390/s21010283. Repéré à https://www.mdpi.com/1424-8220/21/1/283

Chan, J., Zheng, Z., Bell, K., Le, M., Reza, P. H., & Yeow, J. T. W. (2019). Photoacoustic Imaging with Capacitive Micromachined Ultrasound Transducers: Principles and Developments. *Sensors, 19*(16), 3617. Repéré à https://www.mdpi.com/1424-8220/19/16/3617

Chen, B., Chu, F., Liu, X., Li, Y., Rong, J., & Jiang, H. (2013). AlN-based piezoelectric micromachined ultrasonic transducer for photoacoustic imaging. *Applied Physics Letters, 103*(3). doi: 10.1063/1.4816085. Repéré à https://doi.org/10.1063/1.4816085

Chen, M., & Blankenship, R. E. (2011). Expanding the solar spectrum used by photosynthesis. *Trends in Plant Science, 16*(8), 427-431. doi: https://doi.org/10.1016/j.tplants.2011.03.011. Repéré à https://www.sciencedirect.com/science/article/pii/S1360138511000598

Chen, S. L., Huang, S. W., Ling, T., Ashkenazi, S., & Guo, L. J. (2009). Polymer microring resonators for high-sensitivity and wideband photoacoustic imaging. *IEEE Transactions on Ultrasonics, Ferroelectrics, and Frequency Control, 56*(11), 2482-2491. doi: 10.1109/TUFFC.2009.1335

Chu, H. K., Mills, J. K., & Cleghorn, W. L. (2008). MEMS Capacitive Force Sensor for Use in Microassembly. Dans *2008 IEEE/ASME International Conference on Advanced Intelligent Mechatronics* (pp. 797-802). doi: 10.1109/AIM.2008.4601762

Culshaw, B., Giblin, R. A., & Blakey, P. A. (1975). Invited paper. Avalanche diode oscillators. II. Capabilities and limitations. *International Journal of Electronics, 39*(2), 121-172. doi: 10.1080/00207217508920473. Repéré à https://doi.org/10.1080/00207217508920473

Dai, X., Yang, H., & Jiang, H. (2017). In vivo photoacoustic imaging of vasculature with a low-cost miniature light emitting diode excitation. *Optics Letters, 42*, 1456. doi: 10.1364/OL.42.001456

Dangi, A., Agrawal, S., Tiwari, S., Jadhav, S., Cheng, C., Trolier-McKinstry, S., . . . Kothapalli, S. R. (2018). Evaluation of High Frequency Piezoelectric Micromachined Ultrasound Transducers for Photoacoustic Imaging. Dans *2018 IEEE SENSORS* (pp. 1-4). doi: 10.1109/ICSENS.2018.8589733

Do, C. D., Erbes, A., Yan, J., Soga, K., & Seshia, A. A. (2016). Vacuum Packaged Low-Power Resonant MEMS Strain Sensor. *Journal of Microelectromechanical Systems, 25*(5), 851-858. doi: 10.1109/JMEMS.2016.2587867

Erlöv, T., Sheikh, R., Dahlstrand, U., Albinsson, J., Malmsjö, M., & Cinthio, M. (2021). Regional motion correction for in vivo photoacoustic imaging in humans using interleaved ultrasound images. *Biomedical Optics Express, 12*(6), 3312-3322. doi: 10.1364/BOE.421644. Repéré à https://opg.optica.org/boe/abstract.cfm?URI=boe-12-6-3312

Hai, P., Yao, J., Li, G., Li, C., & Wang, L. V. (2016). Photoacoustic elastography. *Optics Letters, 41*(4), 725-728. doi: 10.1364/OL.41.000725. Repéré à https://opg.optica.org/ol/abstract.cfm?URI=ol-41-4-725

Hariri, A., Lemaster, J., Wang, J., Jeevarathinam, A. S., Chao, D. L., & Jokerst, J. V. (2018). The characterization of an economic and portable LED-based photoacoustic imaging system to facilitate molecular imaging. *Photoacoustics, 9*, 10-20. doi: https://doi.org/10.1016/j.pacs.2017.11.001. Repéré à https://www.sciencedirect.com/science/article/pii/S2213597917300204

Hui, J., Cao, Y., Zhang, Y., Kole, A., Wang, P., Yu, G., . . . Cheng, J.-X. (2017). Real-time intravascular photoacoustic-ultrasound imaging of lipid-laden plaque in human coronary artery at 16 frames per second. *Scientific Reports, 7*(1), 1417. doi: 10.1038/s41598-017-01649-9. Repéré à https://doi.org/10.1038/s41598-017-01649-9

Inc, M. (2014). PiezoMUMPs™ Design Handbook. *PiezoMUMPs™ Design Handbook, MEMSCAP*.

Jaber, N., Ramini, A., Hennawi, Q., & Younis, M. I. (2016). Wideband MEMS resonator using multifrequency excitation. *Sensors and Actuators A: Physical, 242*, 140-145. doi: https://doi.org/10.1016/j.sna.2016.02.030. Repéré à https://www.sciencedirect.com/science/article/pii/S0924424716300851

Janggun, J., Guan, X., Elena, S., David, L. C., Girish, G., & Xueding, W. (2020). Imaging of enthesitis by an LED-based photoacoustic system. *Journal of Biomedical Optics, 25*(12), 126005. doi: 10.1117/1.JBO.25.12.126005. Repéré à https://doi.org/10.1117/1.JBO.25.12.126005

Javed, Y., Mansoor, M., & Shah, I. A. (2019). A review of principles of MEMS pressure sensing with its aerospace applications. *Sensor Review, 39*(5), 652-664. doi: 10.1108/SR-06-2018-0135. Repéré à https://doi.org/10.1108/SR-06-2018-0135

Jin, L., & Liang, Y. (2021). Fiber laser technologies for photoacoustic microscopy. *Visual Computing for Industry, Biomedicine, and Art, 4*(1), 11. doi: 10.1186/s42492-021-00076-y. Repéré à https://doi.org/10.1186/s42492-021-00076-y

Jinyuan, L., Bing, S., & Zenghu, C. (1998). High voltage fast ramp pulse generation using avalanche transistor. *Review of Scientific Instruments, 69*(8), 3066-3067. doi: 10.1063/1.1149056. Repéré à https://doi.org/10.1063/1.1149056

Joseph Francis, K., Boink, Y. E., Dantuma, M., Ajith Singh, M. K., Manohar, S., & Steenbergen, W. (2020). Tomographic imaging with an ultrasound and LED-based photoacoustic system. *Biomedical Optics Express, 11*(4), 2152-2165. doi: 10.1364/BOE.384548. Repéré à https://opg.optica.org/boe/abstract.cfm?URI=boe-11-4-2152

Karpiouk, A. B., Wang, B., & Emelianov, S. Y. (2010). Development of a catheter for combined intravascular ultrasound and photoacoustic imaging. *Review of Scientific*

Instruments, 81(1). doi: 10.1063/1.3274197. Repéré à https://doi.org/10.1063/1.3274197

Khoshnoud, F., & Silva, C. W. d. (2012). Recent advances in MEMS sensor technology-mechanical applications. *IEEE Instrumentation & Measurement Magazine, 15*(2), 14-24. doi: 10.1109/MIM.2012.6174574

Kim, C., Favazza, C., & Wang, L. V. (2010). In Vivo Photoacoustic Tomography of Chemicals: High-Resolution Functional and Molecular Optical Imaging at New Depths. *Chemical Reviews, 110*(5), 2756-2782. doi: 10.1021/cr900266s. Repéré à https://doi.org/10.1021/cr900266s

Kogut, L., & Komvopoulos, K. (2003). Electrical contact resistance theory for conductive rough surfaces. *Journal of Applied Physics, 94*(5), 3153-3162. doi: 10.1063/1.1592628. Repéré à https://doi.org/10.1063/1.1592628

Kon, S., Oldham, K., & Horowitz, R. (2007). *Piezoresistive and piezoelectric MEMS strain sensors for vibration detection* (Vol. 6529). SPIE. Repéré à https://doi.org/10.1117/12.715814

Kuijpers, T., Krijnen, G., Lammerink, T., Wiegerink, R., & Elwenspoek, M. (2003). Micromachined capacitive long-range displacement sensor. *IEEE/ASME Journal of Microelectromechanical Systems - J MICROELECTROMECHANICAL SYST*.

Kumar, R., Rab, S., Pant, B. D., & Maji, S. (2018). Design, development and characterization of MEMS silicon diaphragm force sensor. *Vacuum, 153*, 211-216. doi: https://doi.org/10.1016/j.vacuum.2018.04.029. Repéré à https://www.sciencedirect.com/science/article/pii/S0042207X17318171

Laufer, J., Zhang, E., Treeby, B., Cox, B., Beard, P., Johnson, P., & Pedley, B. (2012). In vivo preclinical photoacoustic imaging of tumor vasculature development and therapy. *Journal of Biomedical Optics, 17*(5), 056016. doi: 10.1117/1.JBO.17.5.056016. Repéré à https://doi.org/10.1117/1.JBO.17.5.056016

Lei, Y., Duan, J., Qi, Q., Fang, J., Liu, Q., Zhou, S., & Wu, Y. (2025). The Design and Application of Wearable Ultrasound Devices for Detection and Imaging. *Biosensors (Basel), 15*(9). doi: 10.3390/bios15090561

Liao, W., Liu, W., Rogers, J. E., Usmani, F., Tang, Y., Wang, B., . . . Xie, H. (2013). Piezoelectric micromachined ultrasound tranducer array for photoacoustic imaging. Dans *2013 Transducers & Eurosensors XXVII: The 17th International Conference on Solid-State Sensors, Actuators and Microsystems (TRANSDUCERS & EUROSENSORS XXVII)* (pp. 1831-1834). doi: 10.1109/Transducers.2013.6627146

Liu, C., Teng, J., & Wu, N. (2015). A Wireless Strain Sensor Network for Structural Health Monitoring. *Shock and Vibration, 2015*(1), 740471. doi: https://doi.org/10.1155/2015/740471. Repéré à https://onlinelibrary.wiley.com/doi/abs/10.1155/2015/740471

Lu, Y., Tang, H.-Y., Fung, S., Boser, B., & Horsley, D. (2015). *Short-range and high-resolution ultrasound imaging using an 8 MHz Aluminum Nitride PMUT array* (Vol. 2015). doi: 10.1109/MEMSYS.2015.7050905

Lu, Y., Tang, H.-Y., Fung, S., Wang, Q., Tsai, J., Daneman, M., . . . Horsley, D. (2015). Ultrasonic fingerprint sensor using a piezoelectric micromachined ultrasonic transducer array integrated with complementary metal oxide semiconductor electronics. *Applied Physics Letters, 106*, 3503. doi: 10.1063/1.4922915

Manwar, R., Islam, M. T., Ranjbaran, S. M., & Avanaki, K. (2022). Transfontanelle photoacoustic imaging: ultrasound transducer selection analysis. *Biomedical Optics Express, 13*(2), 676-693. doi: 10.1364/BOE.446087. Repéré à https://opg.optica.org/boe/abstract.cfm?URI=boe-13-2-676

Manwar, R., Li, X., Kratkiewicz, K., Zhu, D., & Avanaki, K. (2023). Adaptive coherent weighted averaging algorithm for enhancement of photoacoustic tomography images of brain. *Journal of Biophotonics, 16*(11), e202300103. doi: https://doi.org/10.1002/jbio.202300103. Repéré à https://onlinelibrary.wiley.com/doi/abs/10.1002/jbio.202300103

Meng, L., Deschaume, O., Larbanoix, L., Fron, E., Bartic, C., Laurent, S., . . . Glorieux, C. (2019). Photoacoustic temperature imaging based on multi-wavelength excitation. *Photoacoustics, 13*, 33-45. doi: https://doi.org/10.1016/j.pacs.2018.11.004. Repéré à https://www.sciencedirect.com/science/article/pii/S2213597918300314

Mohammed, A. A. S., Moussa, W. A., & Lou, E. (2008). High Sensitivity MEMS Strain Sensor: Design and Simulation. *Sensors, 8*(4), 2642-2661. Repéré à https://www.mdpi.com/1424-8220/8/4/2642

Mohammed, A. A. S., Moussa, W. A., & Lou, E. (2011). High-Performance Piezoresistive MEMS Strain Sensor with Low Thermal Sensitivity. *Sensors, 11*(2), 1819-1846. Repéré à https://www.mdpi.com/1424-8220/11/2/1819

Moore, S. I., & Moheimani, S. O. R. (2014). Displacement Measurement With a Self-Sensing MEMS Electrostatic Drive. *Journal of Microelectromechanical Systems, 23*(3), 511-513. doi: 10.1109/JMEMS.2014.2314296

Morita, M., Ohmi, T., Hasegawa, E., Kawakami, M., & Suma, K. (1989). Control factor of native oxide growth on silicon in air or in ultrapure water. *Applied Physics Letters, 55*(6), 562-564. doi: 10.1063/1.102435. Repéré à https://doi.org/10.1063/1.102435

Nguyen, T.-V., Tanii, R., Takahata, T., & Shimoyama, I. (2019). Development of a single-chip elasticity sensor using MEMS-based piezoresistive cantilevers with different tactile properties. *Sensors and Actuators A: Physical, 285*, 362-368. doi: https://doi.org/10.1016/j.sna.2018.11.020. Repéré à https://www.sciencedirect.com/science/article/pii/S0924424718310264

Nyayapathi, N., Zheng, E., Zhou, Q., Doyley, M., & Xia, J. (2024). Dual-modal photoacoustic and ultrasound imaging: from preclinical to clinical applications. *Frontiers in Photonics, Volume 5 - 2024*. doi: 10.3389/fphot.2024.1359784. Repéré à https://www.frontiersin.org/journals/photonics/articles/10.3389/fphot.2024.1359784

Okulov, P. D. (2017). *Brevet nº US10663357*.

Panas, R. M., Cullinan, M. A., & Culpepper, M. L. (2012). Design of piezoresistive-based MEMS sensor systems for precision microsystems. *Precision Engineering, 36*(1), 44-54. doi: https://doi.org/10.1016/j.precisioneng.2011.07.004. Repéré à https://www.sciencedirect.com/science/article/pii/S0141635911001176

Pandya, H. J., Kim, H. T., Roy, R., & Desai, J. P. (2014). MEMS based low cost piezoresistive microcantilever force sensor and sensor module. *Materials Science in Semiconductor Processing, 19*, 163-173. doi: https://doi.org/10.1016/j.mssp.2013.12.016. Repéré à https://www.sciencedirect.com/science/article/pii/S1369800113003909

Pandya, H. J., Sheng, J., & Desai, J. P. (2017). MEMS-Based Flexible Force Sensor for Tri-Axial Catheter Contact Force Measurement. *J Microelectromech Syst, 26*(1), 264-272. doi: 10.1109/jmems.2016.2636018

Park, B., Oh, D., Kim, J., & Kim, C. (2023). Functional photoacoustic imaging: from nano- and micro- to macro-scale. *Nano Convergence, 10*(1), 29. doi: 10.1186/s40580-023-00377-3. Repéré à https://doi.org/10.1186/s40580-023-00377-3

Park, S., Mallidi, S., Karpiouk, A., Aglyamov, S., & Emelianov, S. (2007). Photoacoustic imaging using array transducer. *SPIE BiOS, 6437*. doi: https://doi.org/10.1117/12.704240

Preethichandra, D. M. G., Suntharavadivel, T. G., Kalutara, P., Piyathilaka, L., & Izhar, U. (2023). Influence of Smart Sensors on Structural Health Monitoring Systems and Future Asset Management Practices. *Sensors (Basel), 23*(19). doi: 10.3390/s23198279

Razansky, D., Buehler, A., & Ntziachristos, V. (2011). Volumetric real-time multispectral optoacoustic tomography of biomarkers. *Nature Protocols, 6*(8), 1121-1129. doi: 10.1038/nprot.2011.351. Repéré à https://doi.org/10.1038/nprot.2011.351

Ren, D., Li, C., Shi, J., & Chen, R. (2022). A Review of High-Frequency Ultrasonic Transducers for Photoacoustic Imaging Applications. *IEEE Transactions on Ultrasonics, Ferroelectrics, and Frequency Control, 69*(6), 1848-1858. doi: 10.1109/TUFFC.2021.3138158

Sadeghpour, S., Zilonova, E., Hooge, J. D., & Kraft, M. (2021). A Novel 6 MHz Phased Array Piezoelectric Micromachined Ultrasound Transducer (pMUT) with 128 Elements for Medical Imaging. Dans *2021 IEEE International Ultrasonics Symposium (IUS)* (pp. 1-4). doi: 10.1109/IUS52206.2021.9593633

Sawada, R., Higurashi, E., Sanada, S., Chino, D., & Ishikawa, I. (2006). Integrated Micro-Displacement Sensor that can Measure Tilting or Linear Motion for an External Mirror. Dans *IEEE/LEOS International Conference on Optical MEMS and Their Applications Conference, 2006.* (pp. 52-53). doi: 10.1109/OMEMS.2006.1708260

Song, P., Ma, Z., Ma, J., Yang, L., Wei, J., Zhao, Y., . . . Wang, X. (2020). Recent Progress of Miniature MEMS Pressure Sensors. *Micromachines, 11*(1), 56.

Stavrov, V., Stavreva, G., & Shulev, A. (2016). Piezoresistive Position Microsensors with PPM Accuracy. *Procedia Engineering, 168*, 717-720. doi: https://doi.org/10.1016/j.proeng.2016.11.258. Repéré à https://www.sciencedirect.com/science/article/pii/S1877705816335718

Stavrov, V., Todorov, V., Shulev, A., & Hardalov, C. (2013). *MEMS sensors for mm-range displacement measurements with sub-nm resolution* (Vol. 8763). SPIE. Repéré à https://doi.org/10.1117/12.2017381

Stavrov, V., Tomerov, E., Stavreva, G., Hardalov, C., & Shulev, A. (2010). Lateral displacement MEMS sensor. *Procedia Engineering, 5*, 649-652. doi: https://doi.org/10.1016/j.proeng.2010.09.193. Repéré à https://www.sciencedirect.com/science/article/pii/S187770581000740X

Su, R., Ermilov, S., Liopo, A., & Oraevsky, A. (2013). Laser optoacoustic tomography: Towards new technology for biomedical diagnostics. *Nuclear Instruments and Methods in Physics Research Section A: Accelerators, Spectrometers, Detectors and Associated Equipment, 720*, 58-61. doi: https://doi.org/10.1016/j.nima.2012.12.035. Repéré à https://www.sciencedirect.com/science/article/pii/S0168900212015689

Sun, S., Wang, J., Ning, Y., & Zhang, M. (2022). Air-coupled piezoelectric micromachined ultrasonic transducers for surface stain detection and imaging. *Nanotechnology and Precision Engineering, 5*, 013004. doi: 10.1063/10.0009632

Suster, M., Guo, J., Chaimanonart, N., Ko, W. H., & Young, D. J. (2006). A High-Performance MEMS Capacitive Strain Sensing System. *Journal of Microelectromechanical Systems, 15*(5), 1069-1077. doi: 10.1109/JMEMS.2006.881489

Suttikittipong, P., Parawee, T., Nicholas, P., & and Piyawattanametha, W. (2025). Comparison of MEMS-based photoacoustic microscopy in biomedical imaging. *International Journal of Optomechatronics, 19*(1), 2447236. doi: 10.1080/15599612.2024.2447236. Repéré à https://doi.org/10.1080/15599612.2024.2447236

Taruttis, A., Timmermans, A. C., Wouters, P. C., Kacprowicz, M., van Dam, G. M., & Ntziachristos, V. (2016). Optoacoustic Imaging of Human Vasculature: Feasibility by Using a Handheld Probe. *Radiology, 281*(1), 256-263. doi: 10.1148/radiol.2016152160. Repéré à https://pubs.rsna.org/doi/abs/10.1148/radiol.2016152160

Todorov, V., Stavrov, V., & Kreuter, J. (2011). Sub nm-Resolution Static Measurement with MEMS Displacement Sensors. *Procedia Engineering, 25*, 591-594. doi: https://doi.org/10.1016/j.proeng.2011.12.147. Repéré à https://www.sciencedirect.com/science/article/pii/S1877705811058164

Uttamchandani, D. D. (1995). Measurement of mechanical properties of boron doped silicon microresonators using a resonant frequency technique. Dans *IEE Colloquium on Methods of Materials Measurement in Microengineering* (pp. 4/1-4/3). doi: 10.1049/ic:19951466

Van Heumen, S., Riksen, J. J. M., Singh, M. K. A., Van Soest, G., & Vasilic, D. (2023). LED-based photoacoustic imaging for preoperative visualization of lymphatic vessels in patients with secondary limb lymphedema. *Photoacoustics, 29*, 100446. doi: https://doi.org/10.1016/j.pacs.2022.100446. Repéré à https://www.sciencedirect.com/science/article/pii/S2213597922001112

Wang, H., Yang, H., Chen, Z., Zheng, Q., Jiang, H., Feng, P. X. L., & Xie, H. (2021). Development of Dual-Frequency PMUT Arrays Based on Thin Ceramic PZT for Endoscopic Photoacoustic Imaging. *Journal of Microelectromechanical Systems, 30*(5), 770-782. doi: 10.1109/JMEMS.2021.3096733

Wang, J., Zheng, Z., Chan, J., & Yeow, J. T. W. (2020). Capacitive micromachined ultrasound transducers for intravascular ultrasound imaging. *Microsystems & Nanoengineering, 6*(1), 73. doi: 10.1038/s41378-020-0181-z. Repéré à https://doi.org/10.1038/s41378-020-0181-z

Wang, L. V. (2009). Multiscale photoacoustic microscopy and computed tomography. *Nat Photonics, 3*(9), 503-509. doi: 10.1038/nphoton.2009.157

Wang, L. V., & Hu, S. (2012). Photoacoustic tomography: in vivo imaging from organelles to organs. *Science, 335*(6075), 1458-1462. doi: 10.1126/science.1216210

Wang, L. V., & Yao, J. (2016). A practical guide to photoacoustic tomography in the life sciences. *Nat Methods, 13*(8), 627-638. doi: 10.1038/nmeth.3925

Wang, X., Li, W., Jin, L., Gong, M., Wang, J., Zhong, Y., . . . Li, M. (2022). High-precision micro-displacement sensor based on tunnel magneto-resistance effect. *Scientific Reports, 12*(1), 3021. doi: 10.1038/s41598-022-06965-3. Repéré à https://doi.org/10.1038/s41598-022-06965-3

Westerveld, W. J., Leinders, S. M., Muilwijk, P. M., Pozo, J., Dool, T. C. v. d., Verweij, M. D., . . . Urbach, H. P. (2014). Characterization of Integrated Optical Strain Sensors Based on Silicon Waveguides. *IEEE Journal of Selected Topics in Quantum Electronics, 20*(4), 101-110. doi: 10.1109/JSTQE.2013.2289992

Wojciechowski, K. E., Boser, B. E., & Pisano, A. P. (2004). A MEMS resonant strain sensor operated in air. Dans *17th IEEE International Conference on Micro Electro Mechanical Systems. Maastricht MEMS 2004 Technical Digest* (pp. 841-845). doi: 10.1109/MEMS.2004.1290718

Wu, J., Lei, L., Chen, X., Cai, X., Li, Y., & Han, T. (2014). A Three-Dimensional Microdisplacement Sensing System Based on MEMS Bulk-Silicon Technology. *Sensors, 14*(11), 20533-20542. Repéré à https://www.mdpi.com/1424-8220/14/11/20533

Xia, J., Chen, W., Maslov, K., Anastasio, M. A., & Wang, L. V. (2014). Retrospective respiration-gated whole-body photoacoustic computed tomography of mice. *J Biomed Opt, 19*(1), 16003. doi: 10.1117/1.Jbo.19.1.016003

Xu, M., & Wang, L. V. (2006). Photoacoustic imaging in biomedicine. *Review of Scientific Instruments, 77*(4).

Yang, D., Xing, D., Yang, S., & Xiang, L. (2007). Fast full-view photoacoustic imaging by combined scanning with a linear transducer array. *Optics Express, 15*(23), 15566-15575. doi: 10.1364/OE.15.015566. Repéré à https://opg.optica.org/oe/abstract.cfm?URI=oe-15-23-15566

Yang, Y., Tian, H., Yan, B., Sun, H., Wu, C., Shu, Y., . . . Ren, T.-L. (2013). A flexible piezoelectric micromachined ultrasound transducer. *RSC Advances, 3*(47), 24900-24905. doi: 10.1039/C3RA44619K. Repéré à http://dx.doi.org/10.1039/C3RA44619K

Yao, J., & Wang, L. V. (2014). Sensitivity of photoacoustic microscopy. *Photoacoustics, 2*(2), 87-101. doi: https://doi.org/10.1016/j.pacs.2014.04.002. Repéré à https://www.sciencedirect.com/science/article/pii/S2213597914000111

Yao, J., & Wang, L. V. (2021). Chapter 13 - Photoacoustic Molecular Imaging: Principles and Practice. Dans B. D. Ross & S. S. Gambhir (Éds.), *Molecular Imaging (Second Edition)* (pp. 233-244). Academic Press. doi: https://doi.org/10.1016/B978-0-12-816386-3.00016-8. Repéré à https://www.sciencedirect.com/science/article/pii/B9780128163863000168

Yoo, Y., & Choi, B. D. (2021). Readout Circuits for Capacitive Sensors. *Micromachines (Basel), 12*(8). doi: 10.3390/mi12080960

Zeng, L., Liu, G., Di-Wu, Y., & Ji, X. (2014). Cost-efficient laser-diode-induced optical-resolution photoacoustic microscopy for two-dimensional/three-dimensional biomedical imaging. *Journal of Biomedical Optics, 19*, 76017. doi: 10.1117/1.JBO.19.7.076017

Zhang, C., Maslov, K., & Wang, L. V. (2010). Subwavelength-resolution label-free photoacoustic microscopy of optical absorption in vivo. *Opt Lett, 35*(19), 3195-3197. doi: 10.1364/ol.35.003195

Zhang, Y., Howver, R., Gogoi, B., & Yazdi, N. (2011). A high-sensitive ultra-thin MEMS capacitive pressure sensor. Dans *2011 16th International Solid-State Sensors, Actuators and Microsystems Conference* (pp. 112-115). doi: 10.1109/TRANSDUCERS.2011.5969151

Zheng, Q., Wang, H., Yang, H., Jiang, H., Chen, Z., Lu, Y., . . . Xie, H. (2022). Thin ceramic PZT dual- and multi-frequency pMUT arrays for photoacoustic imaging. *Microsystems & Nanoengineering, 8*(1), 122. doi: 10.1038/s41378-022-00449-0. Repéré à https://doi.org/10.1038/s41378-022-00449-0

Zhu, Y., Xu, G., Yuan, J., Jo, J., Gandikota, G., Demirci, H., . . . Wang, X. (2018). Light Emitting Diodes based Photoacoustic Imaging and Potential Clinical Applications. *Sci Rep, 8*(1), 9885. doi: 10.1038/s41598-018-28131-4